UNIVERSITY OF ALBERTA

Diffractive Optics in Optoelectronic Switching

by

Rajkumar Nagarajan (C)

A thesis submitted to the Faculty of Graduate Studies and Research in partial fulfillment of the requirements for the degree of **Doctor of Philosophy**

Department of Electrical and Computer Engineering

Edmonton, Alberta
Spring 1997

National Library of Canada
Acquisitions and Bibliographic Services
395 Wellington Street
Ottawa ON K1A 0N4
Canada

Bibliothèque nationale du Canada
Acquisitions et services bibliographiques
395, rue Wellington
Ottawa ON K1A 0N4
Canada

Your file Votre référence
Our file Notre référence

The author has granted a non-exclusive licence allowing the National Library of Canada to reproduce, loan, distribute or sell copies of his/her thesis by any means and in any form or format, making this thesis available to interested persons.

The author retains ownership of the copyright in his/her thesis. Neither the thesis nor substantial extracts from it may be printed or otherwise reproduced with the author's permission.

L'auteur a accordé une licence non exclusive permettant à la Bibliothèque nationale du Canada de reproduire, prêter, distribuer ou vendre des copies de sa thèse de quelque manière et sous quelque forme que ce soit pour mettre des exemplaires de cette thèse à la disposition des personnes intéressées.

L'auteur conserve la propriété du droit d'auteur qui protège sa thèse. Ni la thèse ni des extraits substantiels de celle-ci ne doivent être imprimés ou autrement reproduits sans son autorisation.

0-612-21608-X

Canada

UNIVERSITY OF ALBERTA

LIBRARY RELEASE FORM

Name of Author: RAJKUMAR NAGARAJAN

Title of Thesis: DIFFRACTIVE OPTICS IN OPTOELECTRONIC SWITCHING

Degree: DOCTOR OF PHILOSOPHY

Year this Degree Granted: 1997

Permission is hereby granted to the University of Alberta Library to reproduce single copies of this thesis and to lend or sell such copies for private, scholarly, or scientific research purposes only.

The author reserves all other publication rights in association with the copyright in the thesis, and except as hereinbefore provided, neither the thesis nor any substantial portion thereof may be printed or otherwise reproduced in any material form whatever without the author's prior written permission.

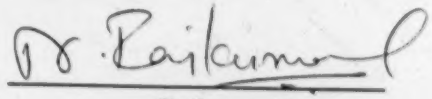

Rajkumar Nagarajan
H-121/5, 33rd Cross Street
Besant Nagar
Madras-600090
India

Date: 3 March 1997

UNIVERSITY OF ALBERTA

FACULTY OF GRADUATE STUDIES AND RESEARCH

The undersigned certify that they have read, and recommend to the Faculty of Graduate Studies and Research for acceptance, a thesis entitled

"Diffractive Optics in Optoelectronic Switching"

submitted by RAJKUMAR NAGARAJAN in partial fulfillment for the degree of DOCTOR OF PHILOSOPHY.

Dr. J. N. McMullin
Supervisor

Dr. K. McGreer
U. of Manitoba

Dr. M. Wilson
Biology

Dr. R. I. MacDonald
Elec. and Comp. Eng.

Dr. J. Conradi
Elec. and Comp. Eng.

DATE: Feb. 28, 1997.

dedicated

to my

grandparents

Abstract

Optoelectronic switches offer a technologically viable approach to perform signal transparent switching functions in present and future fibre optic networks.The feasibility of realising a broadband optoelectronic switch employing free space optical signal distribution is considered. By the design and fabrication of novel diffractive and refractive micro-optical devices, optical distribution schemes for a 3x3 and 4x4 switch have been implemented. The diffractive optical devices are fabricated using semiconductor processing techniques, and the refractive micro-lenses are realised by computer-controlled pressure dispensing of a UV curable polymer. The cross-talk due to the optical distribution was experimentally measured for both cases. Bandwidth limits of an optoelectronic switch are set by the terminal devices that perform the electro-optical and opto-electrical conversions, i.e., the lasers and detectors. In order to evaluate the bandwidth limits of the proposed switch, the high frequency design aspects of the transmitters and receivers are investigated. A four channel wideband optical transmitter package using vertical cavity surface emitting laser arrays with low adjacent channel cross-talk was designed for frequencies up to 2.64 GHz. The low cross-talk performance is achieved by the use of novel coplanar access lines. The suitability of Corning 7059 glass as a transparent high frequency substrate is demonstrated for frequencies up to 18 GHz. The detector package is fabricated by flip-chip bonding an MSM array onto the glass substrate. The high frequency performance of the detector assembly is tested and is shown to be device limited at 2 GHz. A noise analysis of the free space optoelectronic switch was done from the measured experimental data to study the various system impairments.

In addition to the work on broadband optoelectronic free space switch, investigations have also been carried out into the theory and fabrication of novel diffraction gratings, obtained by anisotropically etched V-grooves in silicon. Using scalar diffraction theory to find the amplitudes of the different diffracted orders, a numerical search is used to find the optimum designs for 1:3, 1:5 and 1:7 splitters. To prove the concept, V-bump gratings on a thin silicon nitride diaphragm were fabricated using elaborate micro-machining techniques.

Acknowledgement

My journey towards the PhD has been influenced greatly by my educators and fellow companions in the travel. I would like to take this opportunity to thank each and every one of them for their contribution towards my goal.

I would like to thank my supervisor, Dr. J. N. McMullin, for placing trust in my judgement and allowing me to pursue my areas of interest. The academic freedom enjoyed under his supervision enabled me to develop skills in many different areas. His help, support and encouragement at every stage has made this journey very enjoyable.

Dr. R. I. MacDonald has been a great source of inspiration and I am fortunate to have worked in his midst. I have profited immensely from all the discussions and advice rendered by him during the course of my work. I would also like to thank Dr. B. P. Keyworth for his help and suggestions in the different design aspects of my work. The help rendered by Dino Corazza in the lab, and the interest taken by him towards my work is very much appreciated.

I would like to thank Graham McKinnon of AMC for his help at every stage during the fabrication of the various components. His valuable advice and friendly disposition greatly simplified my task at AMC and made my work very productive. The help rendered by all the staff at AMC is also acknowledged, especially, Yan Loke, Tran Tran, Jim Broughton and Glen Fitzpatrick.

Many thanks are also due for my colleagues at TRLabs with whom I have spent many hours of fruitful discussions. I would like to thank Madhu Krishnaswamy, Craig Unick, Dave Boertjes, Sheldon Walklin, Huy Nguyen, Ray DeCorby, Sing Cheng, Mike Sieben, Reza Paiam and Alan Hnatiw for their inputs at various times.

Finally, I would like to thank my parents who always encouraged and supported me and never once shackled my discretion.

Table of Contents

1. Introduction 1

1.1 Optoelectronic Switch: Basic Operation 1
1.2 Diffractive Optics 3
1.3 Thesis Objectives 4
1.4 Thesis Organisation 4

2. Binary Gratings 6
2.1 Dammann Grating 7
2.1.1 Theory 7
2.2 Fabrication of Dammann Gratings 13
2.2.1 Basic Clean Room Process 13
2.2.2 Reactive ion Etching - Process Details 15
2.3 Test and Measurement Results of the 1:3 Grating 18
2.4 Design of Binary Gratings with Arbitrary Phase 21
2.4.1 Theory 21
2.4.2 Experimental Results 22
2.4.3 Discussion 24

3. Design and Fabrication of V-Groove Gratings 27
3.1 Overview 27
3.2 Grating Design and Scalar Diffraction Theory 28
3.3 Gratings Replicated From a Silicon Master 33
3.4 Fabrication of V-groove Gratings 33
3.4.1 Substrate Preparation 37
3.4.2 Substrate Patterning 39
3.4.3 Sub-micron Micromachining of Silicon 41
3.5 Experimental results and Discussion 45

4. Free Space Optical Distribution for Optoelectronic Switching 48
4.1 3x3 Optoelectronic Cross-bar Switch 48
4.1.1 Free Space Optical Distribution: Theory and Design 50
4.1.2 Beam Optics Theory for Single Lens Imaging 53
4.1.3 Experimental Results 58
4.2 4x4 Optoelectronic Switch Prototype 62
4.2.1 Optical Design of the 4x4 OES 63
4.2.2 Experimental Results 66

5. High Frequency Design of the Optoelectronic Switch 69
5.1 Transmitter Design 69
5.1.1 Multichannel High Frequency Modulation: Design Issues 70
5.1.2 Coplanar Waveguide Access Lines 74
5.1.3 Fabrication of Coplanar Access Lines 76

5.1.4 Experimental Setup and Results 77
5.1.5 Design of the 4-Channel High Frequency VCSEL Driver 81
5.1.6 Experimental Results of the 4-Channel VCSEL Driver 83
5.1.7 Fabrication Errors 88
5.2 Detector Cross-Point Design 89
5.2.1 MSM Biasing 90
5.2.2 Fabrication of the High Frequency Detector Submount 93
5.2.3 Experimental Results 98
5.3 System Issues 100

6. Conclusions 103
6.1 Synopsis of Work done in Novel V-groove Gratings 103
6.2 Synopsis of Work Done in Free Space OES 104
6.2.1 Optical Distribution 104
6.2.2 Transmitter Design 105
6.2.3 Detector Cross-point Design 105
6.2.4 System Issues 106
6.3 Future Directions 106

References 108

Appendix A 115

Appendix B 117

Appendix C 124

List of Tables

Table 2.1 Design values of the transition points for 1:N Dammann gratings

List of Figures

Fig. 1.1 Conceptual diagram of an optoelectronic switch

Fig. 2.1 (a) A continuous phase blazed grating and, (b) it's four level approximation

Fig. 2.2 (a) A cross-section view of a Dammann grating (b) The transmittance function for a period

Fig. 2.3 Fabrication of Dammann gratings

Fig. 2.4 (a) Desired etch profile (b) profile obtained by using a photoresist mask

Fig. 2.5 SEM photograph of a grating etched in quartz with a chrome mask

Fig. 2.6 Photoresist accumulation at the corners

Fig. 2.7 Quartz etched with photoresist as mask and only CHF3 plasma

Fig. 2.8 Measurement set-up for testing the Dammann gratings

Fig. 2.9 Intensity distribution of a 1:3 Dammann grating fabricated with photoresist mask

Fig. 2.10 Plot showing the uniformity of the intensity distribution of the 1:3 grating for three different samples

Fig. 2.11 Camera image of the far-field diffraction pattern of a 1:3 Dammann grating

Fig. 2.12 Transmittance function of a generalized binary grating

Fig. 2.13 Intensity distribution in the diffracted orders of a 1:2 grating

Fig. 2.14 Far field diffraction pattern of the 1:2 binary grating

Fig. 2.15 Effect of an error in the pattern on the diffraction grating

Fig. 2.16 Effect of etch depth errors on the performance of the 1:2 grating

Fig. 2.17 Comparison of different schemes of binary gratings

Fig. 3.1 Structure of a grating with grooves etched in silicon, index n0, and covered with a material of index n1

Fig. 3.2 Standard deviation with respect to the mean of the p = -1, 0, 1 diffraction orders as a function of the grating half-width for five values of the grating period. Length units are micrometers (μm)

Fig. 3.3 Diffraction efficiencies for the same cases as Fig. 3.2

Fig. 3.4 Optimized grating efficiencies as function of overlayer thickness for several values of overlayer index of refraction

Fig. 3.5 Grating profile for generation of (a) 1:3, (b) 1:5, (c) 1:7 beam splitters

Fig. 3.6 Effect of fabrication errors on the efficiency and the uniformity of replicated gratings

Fig. 3.7 Processing steps in the fabrication of V-bump silicon nitride gratings

Fig. 3.8 PMMA on silicon dioxide patterned by e-beam direct write

Fig. 3.9 Silicon dioxide pattern on (100) silicon, transferred from PMMA by RIE

Fig. 3.10 V-grooves formed after the anisotropic etching in 30% KOH at 80oC

Fig. 3.11 Formation of plate like structures due to misalignment of the pattern with (110) flats

Fig. 3.12 Silicon nitride V-bump gratings formed on a 2 μm thick diaphragm

Fig. 3.13 Intensity distribution of the -1, 0, 1 diffracted orders for the Si3N4 V-bump grating at different wavelengths as predicted by scalar theory

Fig. 3.14 Intensity distribution of the diffracted orders, measured at 675 nm

Fig. 3.15 Intensity distribution of the diffracted orders, measured at 1300 nm

Fig. 4.1 Basic design of the 3x3 optoelectronic switch

Fig. 4.2 (a) Optical-in and electrical-out configuration (b) Electrical-in and electrical-out configuration

Fig. 4.3 Fabrication of the focusing and beam splitting elemen

Fig. 4.4 SEM photographs of the polymer microlenses, top view and side view

Fig. 4.5 Simplified ray diagram of the optical distribution

Fig. 4.6 Gaussian beam imaged by a thin lens

Fig. 4.7 The spot size 2W(v') of the beam at the detector plane vs the source distance u away from the lens

Fig. 4.8 Image of the optical distribution at the detector plane

Fig. 4.9 3x3 MSM detector layout

Fig. 4.10 Simulation of the coupling between channels 2 and 3 of the layout in Fig. 4.9 for frequencies between 1 Mhz to 10 GHz

Fig. 4.11 Simulation of the coupling between channels 2 and 3 for coplanar lines

Fig. 4.12 Design prototype of the 4x4 free-space optoelectronic switch

Fig. 4.13 Trace of a single input beam illustrating the 1:4 split achieved by the grating and the beam-splitter

Fig. 4.14 Spot size 2W'(v') at the detector plane vs object distance, u, from the lens

Fig. 4.15 Minimum achievable spot size {2W'(v')}min at the detector plane vs F# of the micro-lens

Fig. 4.16 Image of the optical distribution at a distance of 17 mm from the grating

Fig. 4.17 The +1 diffracted orders imaged at the detector plane

Fig. 5.1 (a) A VCSEL die containing 12 lasers at 250 μm pitch, (b) VCSELs emitting light under current injection

Fig. 5.2 A typical access line scheme for simultaneous high frequency modulation of an optoelectronic array

Fig. 5.3 Geometry of a microstrip transmission line

Fig. 5.4 A microstrip access line layout for a VCSEL array

Fig. 5.5 Simulation of microstrip access lines. Trace-B shows the response of a single channel, and Trace-A is the cross-talk in the adjacent channel due to coupling

Fig. 5.6 Geometry of a coplanar transmission line

Fig. 5.7 Coplanar access line layout for a VCSEL array

Fig. 5.8 Simulation of coplanar access lines. Trace-A is the response of a single channel, and Trace-B is the cross-talk in the adjacent channe

Fig. 5.9 Fabrication of CPW access lines using semiconductor processes

Fig. 5.10 Camera image of the substrate showing the dual pick-up microwave probes

Fig. 5.11 Experimental set-up to measure single channel performance

Fig. 5.12 (a) S21 and S11 of a single channel (b) the phase response

Fig. 5.13 Experimental set-up for adjacent channel cross-talk measurement

Fig. 5.14 Plot showing the S21 of channel-1 and cross-talk signal picked up in channel-2

Fig. 5.15 A typical bias-T driver configuration for modulating a laser

Fig. 5.16 Four-channel high frequency VCSEL package fabricated on AlN

Fig. 5.17 Picture showing the details of the bias-T

Fig. 5.18 (a)Experimental set-up for measuring the laser frequency response (b) picture of the measurement setup showing the pick-up fibre

Fig. 5.19 (a) Response of the laser for different bias currents (b) Phase response (c) S11 of the laser package

Fig. 5.20 Set-up to measure the adjacent channel cross-talk in the VCSEL

Fig. 5.21 (a)The response of the VCSEL, to a modulation applied at its input is shown in Trace-a, and to a modulation applied in the adjacent channel is shown in Trace-b

Fig. 5.22 Plot showing the change in Zo as a function of the metal undercut

Fig. 5.23 Structure of a planar MSM

Fig. 5.24 (a) An MSM detector showing the metal fingers (b) an array of MSMs

Fig. 5.25 Biasing circuit for the MSM array. C1=82 pF, C2=1 nF, C3=10 nF, L1=10 nH, R1=500 ohm

Fig. 5.26 Response of the MSM array package when C1 is 9 mm away from the detector (b) response when C1 is 3 mm away

Fig. 5.27 Layout of the MSM detector cross-point

Fig. 5.28 (a) The S21 and S11 of the coplanar transmission line fabricated on Corning 7059 glass substrate (b) phase response of the coplanar line on glass (c) the group delay (d) Smith chart of the S21 of the coplanar line on glass

Fig. 5.29 Picture showing the MSMs flip-chip bonded with silver epoxy

Fig. 5.30 The detector substrate with flip-chip bonded MSMs and associated biasing circuitry

Fig. 5.31 Experimental set-up used to test the performance of the detector submount

Fig. 5.32 (a) The frequency response of the MSM array at different bias voltages. The traces a, b, c, d, e are at 2V, 4V, 6V, 8V, 10V bias respectively. (b) the phase response

List of Abbreviations

AC	Alternating Current
AlN	Aluminium Nitride
AMC	Alberta Microelectronic Centre
BOE	Buffered Oxide Etch
CCD	Charge Coupled Device
CHF_3	Tri-fluoro-methane
CF_4	Carbon Tetra-Fluoride
CPW	Coplanar Waveguide
CRC	Communications Research Centre
DC	Direct Current
DOE	Diffractive Optical Element
ECN	Electrical Cross-talk Noise
EDP	Ethylenediamine Pyrocatechol
EIEO	Electrical-In and Electrical-Out
GaAs	Gallium Arsenide
HF	Hydrofluoric Acid
HP	Hewelett Packard
IPA	Iso-Propyl-Alcohol
KOH	Potassium Hydroxide
L-C	Inductor-Capacitor
MDS	Microwave Design System
MMIC	Monolithic Microwave Integrated Circuit
MSM	Metal Semiconductor Metal
MZ	Mach Zehnder
NaOH	Sodium Hydroxide
NiCr	Nichrome
OCN	Optical Cross-talk Noise
OES	Optoelectronic Switch

OIEO	Optical-In and Electrical-Out
PCB	Printed Circuit Board
PECVD	Plasma Enhanced Chemical Vapour Deposition
PMMA	Polymethylmethacralate
R-C	Resistor-Capacitor
RIE	Reactive Ion Etching
RIN	Relative Intensity Noise
RF	Radio Frequency
SEM	Scanning Electron Microscope
Si_3N_4	Silicon Nitride
SiO_2	Silicon Dioxide
SMF	Single Mode Fibre
S/N	Signal to Noise Ratio
SOA	Semiconductor Optical Amplifiers
TRLabs	Telecommunication Research Labs
UV	Ultra-Violet
VCSEL	Vertical Cavity Surface Emitting Laser
WDM	Wavelength Division Multiplexing

List of Symbols

A_p	Fourier Coefficient
F	F number of a lens
F_n	Noise figure
$\overline{I_p}$	Generated photocurrent
$\overline{i^2_{RIN}}$	Noise power at the receiver due to the laser RIN
$\overline{i^2_{ECN}}$	Noise power at the receiver due to electrical cross-talk in the laser
$\overline{i^2_{OCN}}$	Noise power at the receiver due to cross-talk in the optical distribution
$\overline{i^2_{SN}}$	Shot noise power of the receiver
$\overline{i^2_{TN}}$	Thermal noise power of the receiver
k_o	Propagation constant of a wave in free space
K	Boltzman constant
$\overline{P_e}$	Power output from the laser
$\overline{P_o}$	The available power at the detector
R(z)	Radius of curvature of a Gaussian beam
R_L	Load resistor at the receiver
T(x)	Transmittance function
T	Temperature in ^oKelvin
u_{opt}	Optimum object distance from the lens
v'	Distance of the detector plane from the lens
W(z)	$1/e^2$ radius of a Gaussian beam

W_o	Waist of a Gaussian beam
z_o	Rayleigh length of a Gaussian beam
Z_o	Characteristic impedance of a transmission line
Λ	Period of a grating
λ_o	Free space wavelength
η	Diffraction Efficiency of a grating
$\zeta(z)$	Excess phase factor of a Gaussian beam
ε_r	Relative permittivity
δ_{skin}	Skin depth
$\bar{}$	Time average
$\lvert\ \rvert$	Absolute value

Chapter 1

Introduction

The continued rapid progress in the deployment of fibre-optic communications, and the anticipated total dominance of optical fibre in the wired network, has led to widespread interest in employing photonics to implement switching functions, otherwise not possible by electronics due to technology limitations [1]. In addition to micro-second switching times, future optical networks would demand from cross-connect switches functionalities such as bit-rate and code rate transparency for implementing network survivability [2]. These functions can be obtained by using all-optical switches such as Mach-Zehnder (MZ) switches [3], or those that use semiconductor optical amplifiers (SOA) [4]. It is also recognised that future optical networks which employ wavelength division multiplexing (WDM), would require switches that allow payload and spatial reconfigurability of a wavelength channel. The latter is possible with switches of the MZ and SOA type, but payload reconfigurability of wavelength channels by an all-optical approach has yet to be demonstrated.

A simple and technologically viable approach to perform all the required functionalities is to employ optoelectronic switches [5]-[7]. A 10x10 optoelectronic switch has been recently built as a prototype [8] and has demonstrated bit-rate and code transparency at all rates below the inherent bandwidth (1.3 GHz) of the lasers used in the switch. The work described in this thesis focuses around this switching technology, and explores alternate optical and electrical designs for future optoelectronic switching modules.

1.1 Optoelectronic Switch: Basic Operation

The system performance of any electronic space division switch matrix degrades at high frequencies because of the crosstalk between adjacent conductor lines carrying high frequency current. An optoelectronic switch (OES) offers significantly improved performance by distributing the input signals optically to the photodetectors which act as the

cross-points [5]. The conceptual diagram of an optoelectronic switch is shown in Fig. 1.1. The signals generated by each of the rows of photodetectors is summed electrically to form the outputs. Switching is controlled electrically by turning the detectors ON and OFF with a bias voltage. As the incoming paths are optical, a great degree of immunity to crosstalk can be gained, and the crosstalk that may arise in the outgoing electrical lines can be reduced by proper shielding as the adjacent conductor lines are no longer electrically connected.

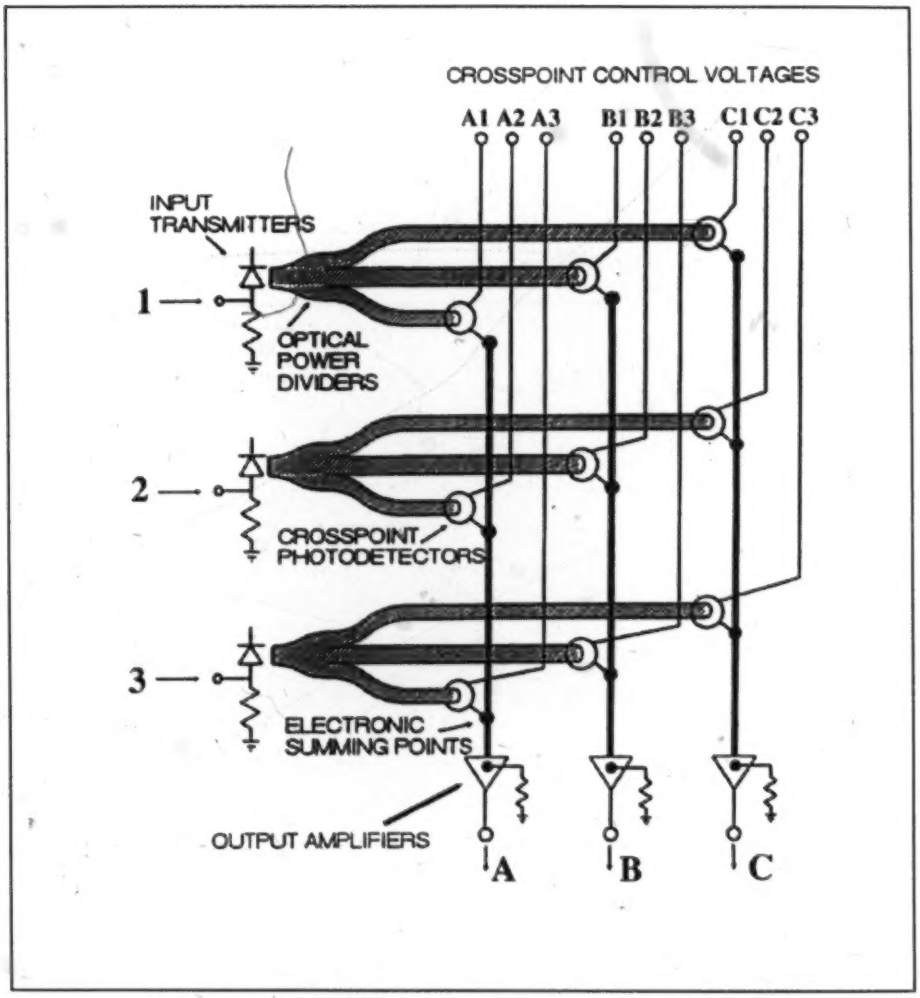

Fig. 1.1 Conceptual diagram of an optoelectronic switch

The inputs to the switch could be optical or electrical. If the signal in Channel-1 is to be switched to the output Channel-A then detector A1 is biased to the ON state; likewise, if Channel-3 is to be switched to Channel-B the detector cross-point B3 is biased to the ON state. Such switching matrices have enormous potential in broadband applications such as cross-connection in telecommunication network restoration, in asynchronous transfer mode (ATM) cross-connect switches and also in other high speed analog and digital signal processing applications [9]-[11].

One of the critical issues to be dealt with in the design of such a switching matrix is the optical distribution of the input signals to the various cross-points or detectors. This has been achieved in the past using 1:N multimode fibre splitters prealigned in silicon V-grooves and butt-coupled to a linear Metal-Semiconductor-Metal (MSM) detector array [8]. The main advantage of an optical fibre distribution scheme is the high degree of cross-talk isolation (>50 dB) between the adjacent channels, thus making it suitable for analog and digital switching applications. The drawbacks are that it is very bulky and handling of large numbers of fibres is difficult and time consuming thus having a direct bearing on the cost of manufacture. Alternative approaches to overcoming this problem would be to use integrated waveguides or to employ free-space optical power distribution. Free-space distribution, which has been investigated in the past for optical interconnect applications in high speed digital computing [12] offers the advantage of low cost and high density of interconnections, but has not been studied for optical distribution in optoelectronic matrix switching. The work described in this thesis fills this gap, and explores novel free-space optical distribution schemes for OES using diffractive optical techniques.

1.2 Diffractive Optics

Diffractive optics, a relatively new term for a branch of knowledge more than 100 years old, describes an area in which the diffraction of light is used as the means to achieve an end. A diffractive optical element (DOE) generally refers to an optical element that operates principally on the mechanism of diffraction as opposed to refraction or reflection and replaces a conventional refractive optical element such as lens or prism. In other words, DOE is a two dimensional periodic structure designed to modulate the phase

of an incoming wave to focus it to a single point and thus act as a lens or to generate a pattern of spots for imaging. The diffraction grating has now come a long way from its original spectroscopic application to perform a whole new range of functions including light focusing, diffusing and imaging.

Diffractive optics have attracted a sudden surge of research interest over the last few years and have moved from obscurity to an important technology thanks to a fascinating coincidence of the emergence of new system requirements with the development of a whole collection of new enabling technologies. These include computational methods, optical materials and finally micromachining techniques using semiconductor process technologies [13]. The new system requirements pulling the development of DOEs include optical interconnect applications for chip-to-chip and board-to-board interconnects for future high speed digital computing, advanced imaging applications, commercial and entertainment electronics which utilize optical disk storage, and many more [12], [14].

1.3 Thesis Objectives

In this project, the author has looked into the feasibility of realising a broadband optoelectronic switch with free-space optical distribution. Two different schemes of optical distribution employing novel diffractive and micro-optical devices were considered for implementation. In order to establish the bandwidth limits of the proposed OES, work was also done on the high frequency electrical aspects of the terminal devices in the switch, namely the lasers and detectors. In addition to the work on broadband OES, investigations into the theory and fabrication of novel V-groove gratings in silicon, by micro-machining techniques, were undertaken.

1.4 Thesis Organisation

This thesis is organised along the following lines:

Chapter 2: This chapter discusses the theory and fabrication of binary gratings that could be used for optical beam splitting applications. The work done in design simula-

tions, fabrication and testing of high efficiency arbitrary phase Binary gratings for 1:N splitters is also discussed.

Chapter 3: A novel type of diffraction grating based on anisotropic etching of silicon has been conceived. This chapter explains the theoretical and experimental work done in this area. The gratings fabricated using this technique provide an alternative to the more popular binary gratings used in beam-splitting applications.

Chapter 4: Two prototypes of free-space optical distribution for optoelectronic switching were conceived and designed using novel diffractive-refractive elements. Their performance is compared with regard to cross-talk, bandwidth and ease of manufacturability.

Chapter 5: The high frequency design layout for the optical sources and detector cross-points in an optoelectronic matrix switch is closely tied to the architecture used for optical distribution. In this chapter, a very low electrical cross-talk design for driving a VCSEL array is reported. The cross-talk performance obtained is the lowest reported by any group so far. In addition, the design of the MSM cross-point array on Corning 7059F glass is detailed and the performance of 7059F glass as an excellent microwave substrate is demonstrated.

Chapter 6: This chapter concludes the thesis summarising the important results obtained in this work. Future directions for free-space optoelectronic switching that would enhance the existing capabilities are proposed.

Chapter 2

Binary Gratings

Binary gratings are a class of phase grating that offers discrete phase modulation to an incoming wave. This class of gratings has also spawned new terms, "Binary Optics and Digital Optics", and rests on the proposition that there is a little difference between a continuous phase structure and its approximation by a series of steps (4 to 16 usually). Fig. 2.1(a) is a drawing of the well known blazed grating and on the right is its 4-level binary approximation. This technique of fabricating a continuous phase relief grating by discrete approximations was made possible only by the great advances in micro-lithography and semiconductor processes.

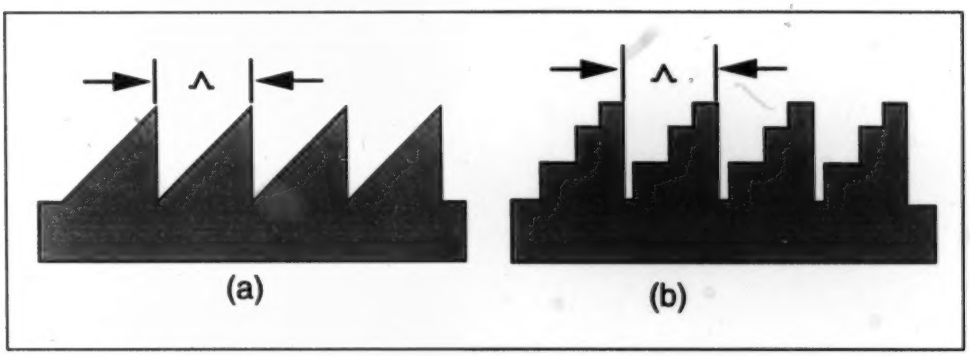

Fig. 2.1 (a) A continuous phase blazed grating and, (b) it's four level approximation

The grating in Fig. 2.1(a) may be fabricated using precision diamond turning/ruling machines and the grating in Fig. 2.1(b) by photolithography using a set of accurate masks and proper aligning. The etching is usually done by reactive ion etching (RIE). The greater the number of discrete levels in the binary grating, the closer its performance would match to its continuous phase counterpart. Even though binary gratings may be slightly less efficient than continuous phase gratings, their advantages and flexibility offer no parallel. Binary gratings are fabricated using semiconductor process technology and hence could be inexpensively mass produced. However, their greatest advantage lies in being

able to produce off-axis Fresnel lenses and other non-symmetrical patterns which cannot be made on lathes [15]-[16]. One of the important types of binary DOE is the Dammann grating [17] and the work done in designing and fabricating this class of grating is the subject of this chapter.

2.1 Dammann Grating

Dammann gratings are binary phase gratings that can be used to generate a 1-D or 2-D array of equal intensity spots. These gratings offer only two levels of phase modulation to an incoming wave, i.e. an input beam passing through these gratings can be phase shifted by 0^o or 180^o. The idea of using a special type of diffraction grating for this purpose originated with Dammann and Gortler in 1971 [18]. Their goal was to obtain multiple images from one input object, and their application was in optical lithography. Another paper, by Dammann and Koltz [19], explains in more detail the theory of the approach. Related articles on the subject of beam splitter gratings for multiple imaging were written by Boivin[20] and Lee[21]. Other uses for Dammann gratings were proposed by Killat et al. [22] for making star couplers, and Veldkamp et al. [23] for coherent summation of beams from different laser sources. Recently, there has been a renewed interest in Dammann gratings caused by new developments in optical digital computing in which arrays of spots must be generated to provide optical power to arrays of electro-optic logic devices. A brief theory of Dammann gratings is given in the next section followed by the fabrication techniques.

2.1.1 Theory

The general shape of a Dammann grating is shown in Fig. 2.2 (a) and its phase representation in Fig. 2.2 (b). When a light wave passes through the unetched portion of the grating it undergoes a phase shift

$$\Phi_1 = nk_oD \qquad 2.1$$

where k_o is the propagation constant and is given by

$$k_o = \frac{2\pi}{\lambda_o} \qquad 2.2$$

n is the refractive index of the material and λ_o the free space wavelength of the light beam.

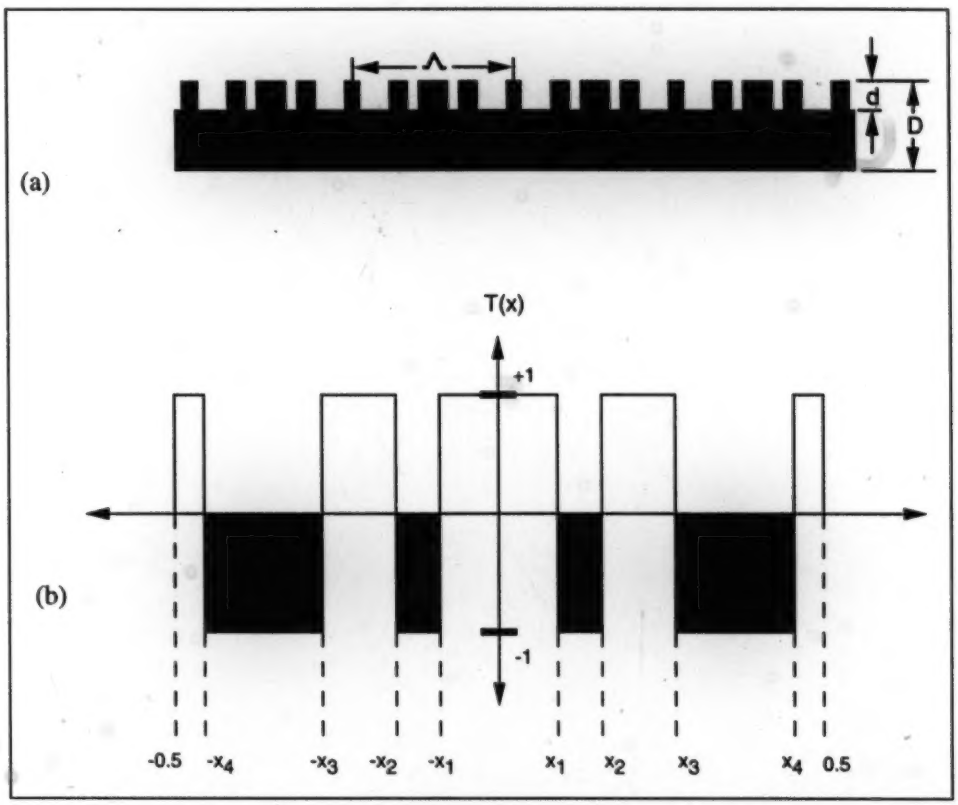

Fig. 2.2 (a) A cross-section view of a Dammann grating (b) The transmittance function for a period

Similarly when the wave passes through the etched portion of the grating it undergoes a phase shift

$$\Phi_2 = k_o d + k_o n (D - d) \qquad 2.3$$

in a Dammann grating

$$\Delta\Phi = \Phi_1 - \Phi_2 = \pi \qquad 2.4$$

From Equations 2.1 to 2.4 we obtain for the etch depth d

$$d = \frac{\lambda_o}{2(n-1)} \qquad 2.5$$

The following can be noted from Fig. 2.2 (b) about the properties of the transmittance function T(x). For this kind of grating T(x) can have only two values i.e.

$$T(x) = \pm 1 \qquad 2.6$$

and is a periodic function i.e.

$$T(x) = T(x+\Lambda) \qquad 2.7$$

and also a symmetric function, which means

$$T(x) = T(-x) \qquad 2.8$$

If we set the basic period of the grating $\Lambda = 1$ then a period could be represented in the interval $-0.5 \le x \le 0.5$. In the interval from x = 0 to x = 0.5 there are N transition points at which T(x) changes its value between +1 and -1. The representation in Fig. 2.2 shows four transition points. The goal is to compute the coordinates $x_1, x_2, \ldots\ldots x_N$ so that the zeroth and the $\pm 1, \ldots\ldots \pm m^{th}$ diffraction order become equal in intensity. It follows naturally that in order to obtain a 1:2m+1 split ratio there should be N = m transition points in the interval $0 \le x \le 0.5$. In the following we denote the set of coordinates by a vector $\bar{x} = (x_1, x_2 \ldots\ldots x_N)$. We also use the convention that $x_0 = 0$ and $x_{N+1} = 0.5$. Within the interval from 0 to +0.5 the amplitude function of T(x) can be written as

$$T(x) = \sum_{l=0}^{N} (-1)^N rect\left[\frac{x - (x_{l+1} + x_l)/2}{x_{l+1} - x_l}\right], \quad 0 \le x \le 0.5 \qquad 2.9$$

where

$$rect(x) \equiv 1 \quad \text{for } |x| < 1/2 \text{ and}$$

$$rect(x) \equiv 0 \quad \text{for } |x| \ge 1/2.$$

Assuming an infinite extension of the grating in the x-direction, we can represent T(x) by

a Fourier series

$$T(x) = \sum_{-\infty}^{\infty} A_p e^{(2\pi jpx)} \qquad 2.10$$

The coefficients A_p give the amplitudes of the diffraction orders in the Fourier plane. From Eq. 2.8 we see that T(x) is a symmetric function and hence

$$A_p = 2 \int_0^{0.5} T(x) \cos(2\pi px)\, dx \qquad 2.11$$

Using Eqs. 2.6, 2.7 and 2.8, a straightforward computation yields the following expressions for the amplitudes of the diffraction orders

$$A_o = 4 \sum_{n=1}^{N} (-1)^{n+1} x_n + (-1)^{N+1} \qquad 2.12$$

$$A_p = \frac{2}{p\pi} \sum_{n=1}^{N} (-1)^{n+1} \sin(2\pi p x_n) \qquad p \neq 0 \qquad 2.13$$

According to Parseval's theorem, the sum of the intensities of all diffraction orders is 1, therefore

$$\sum_{p=-\infty}^{\infty} I_p = 1 \qquad \text{where } I_p = A_p^{\,2} \qquad 2.14$$

We are looking for solutions for the coordinates $\bar{x} = (x_1, x_2 \ldots\ldots x_N)$ so that the intensities of the lowest (2m + 1) diffraction orders become equal, i.e.

$$I_o(\bar{x}) = I_{\pm 1}(\bar{x}) = \ldots\ldots = I_{\pm m}(\bar{x}) \qquad 2.15$$

Since $I = A^2$, there is more than one solution to the problem. Keeping the sign of A_o positive and since $A_m = A_{-m}$, we find that there are 2^N possible solutions, a result given by Dammann and Koltz [19]. If we change the sign of A_o, more solutions to the problem are not added since this is achieved by simply inverting the grating pattern. This does not change the position of the coordinates. There is no direct way to solve Eqs. 2.12 and 2.13, and therefore optimization techniques have to be used to find the solutions for $x_1, x_2, \ldots\ldots x_N$. Different techniques are available in the literature [24] to perform this task. For the optimization, we have to define an objective (or cost) function that can be optimized. The objective function Ψ is a function of the transition coordinates i.e.

$$\Psi = \Psi(x_1, x_2 \ldots\ldots x_N) \qquad 2.16$$

For the Dammann grating problem it would be appropriate to define Ψ as the standard deviation with respect to the mean, of the intensities $I_o, I_{\pm 1}, \ldots\ldots, I_{\pm N}$.

$$\Psi(\bar{x}) = \frac{1}{\langle I \rangle}\left[\frac{1}{2N}\sum_{m=-N}^{N}\left|(I_m(\bar{x}) - \langle I \rangle)\right|^2\right]^{1/2} \qquad 2.17$$

where $\langle I \rangle$ denotes the mean value of all intensities

$$\langle I \rangle = \frac{1}{2N+1}\sum_{m=-N}^{N} I_m \qquad 2.18$$

Another criterion included in the optimization is to maximize the efficiency, i.e. the amount of light power in the desired diffracted orders. The efficiency is defined as

$$\eta = \sum_{m=-N}^{N} I_m \qquad 2.19$$

This restricts the search to one of the 2^N maxima. The design values for x from N=1 to N=10 are shown in Table 2.1 [25]. One of the important points to be noted from Table 2.1 is that as the value of N increases the minimum feature size δ decreases at the approximate rate of $N^{-3/2}$.

Table 2.1 Design values of the transition points for 1:N Dammann gratings

N	x_n				η	δ
1	0.367629				66.42%	2.6×10^{-1}
2	0.019304	0.367657			77.39%	3.8×10^{-2}
3	0.104582	0.155223	0.377125		65.52%	5.1×10^{-2}
4	0.099750	0.159152	0.369009	0.491743	66.32%	1.66×10^{-2}
5	0.006497	0.167640	0.215973	0.287050	59.42%	6.5×10^{-3}
	0.424112					
6	0.012690	0.178617	0.189778	0.235271	70.01%	1.1×10^{-2}
	0.371513	0.468108				
7	0.001317	0.161904	0.219859	0.234420	65.40%	1.3×10^{-3}
	0.297862	0.396294	0.471380			
8	0.033914	0.085013	0.208060	0.225219	67.77%	4.7×10^{-3}
	0.326301	0.381807	0.386448	0.462768		
9	0.091626	0.095805	0.145224	0.202884	68.71%	4.1×10^{-3}
	0.249280	0.330181	0.424735	0.446794		
	0.462340					
10	0.040571	0.058850	0.164916	0.217545	69.18%	6.9×10^{-3}
	0.285866	0.329488	0.336420	0.418581		
	0.472982	0.490914				

For example, if the grating period Λ was chosen to be 100 μm, then for a 1:21 splitter (N=10) the minimum feature size required would be 0.69 μm. This would mean that the masks would have to be generated using electron beam writers and the fabrication tolerances would have to be very tightly controlled.

2.2 Fabrication of Dammann Gratings

2.2.1 Basic Clean Room Process

Designs of a 1:3 grating are laid on a mask generated by photomasking.The minimum feature size that can be defined in a photomask is 3 μm. In this work the minimum feature size of the gratings was fixed at 5 μm and from Table 2.1 this gave a period of approximately 20 μm for the 1:3 grating. The 1:3 grating will be used for free space optical distribution applications, covered in chapter 4. The substrate chosen to fabricate the gratings is fused silica quartz or pure SiO_2. Quartz is preferred over ordinary glass for etching gratings because the chemical properties of quartz are very predictable and do not vary from sample to sample. Glass, on the other hand, is SiO_2 with some dopants such as Sodium (Na), Potassium (K) etc., and this makes the chemical properties very unpredictable and the properties tend to vary from sample to sample. For gratings where precise control of etch depths are required, quartz has come to be the universal choice for all DOEs.

The fabrication steps involved are shown in Fig. 2.3. As a first step, a 0.1 μm layer of chrome is sputtered onto the quartz substrate. Then, HPR 504 positive photoresist is spun on to the substrate at about 4500 rpm to obtain a 1 μm layer of photoresist. The substrate is then soft-baked in vacuum at 110°C for 1 minute. The grating pattern is then transferred to the substrate by contact UV lithography in the high pressure contact mode. The exposure dose has to be properly calibrated to avoid over or under exposure of the photoresist. The resist is then developed in 352 photoresist developer (NaOH) for about 40 seconds to rinse of the exposed areas. Next, the substrate is dipped in a chrome etch solution to etch the chrome in the areas not covered by the photoresist. This transfers the

photoresist pattern to the chrome layer. The substrate is then placed in the RIE chamber to plasma etch the exposed quartz areas.

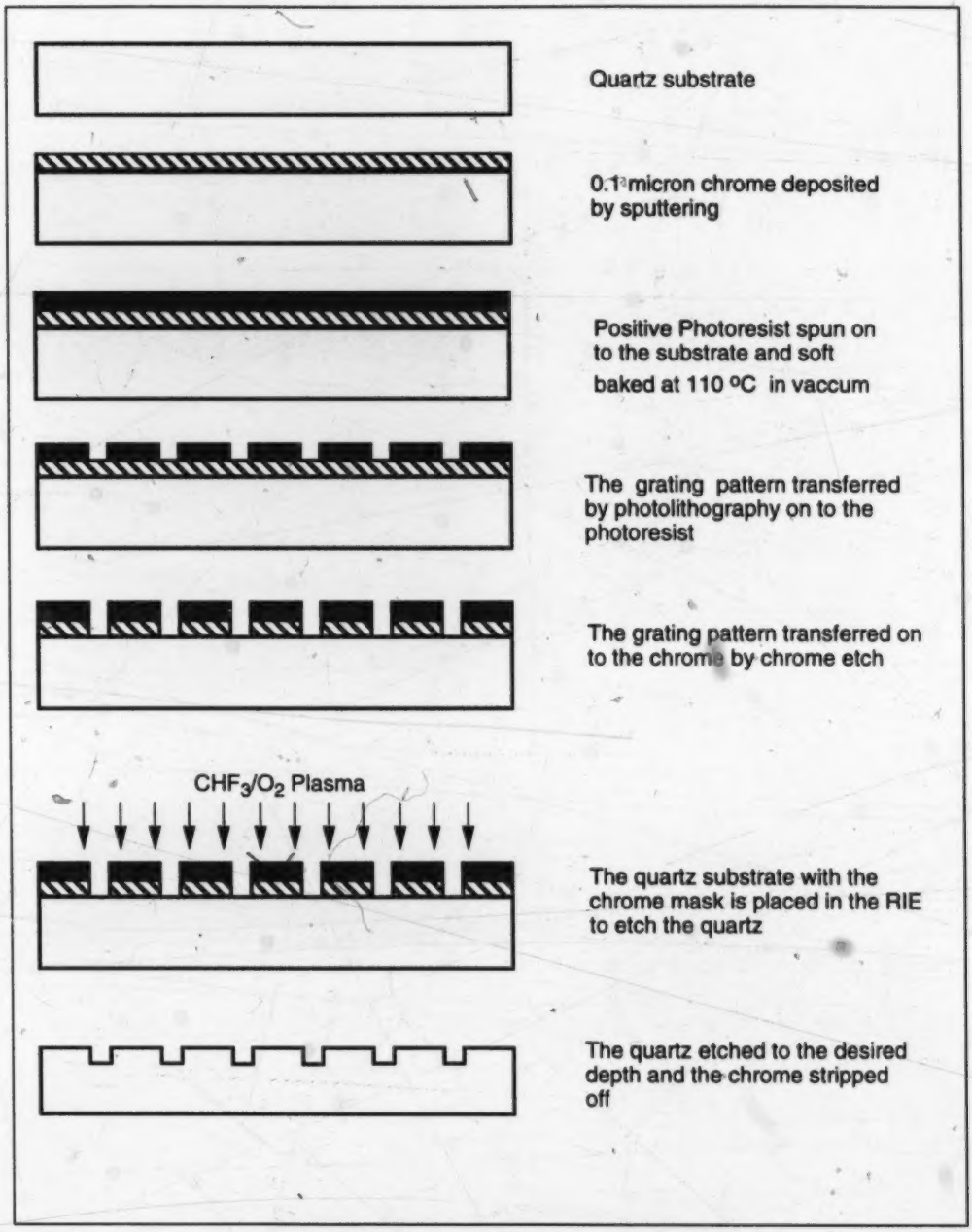
Quartz substrate
0.1 micron chrome deposited by sputtering
Positive Photoresist spun on to the substrate and soft baked at 110 °C in vaccum
The grating pattern transferred by photolithography on to the photoresist
The grating pattern transferred on to the chrome by chrome etch
CHF_3/O_2 Plasma
The quartz substrate with the chrome mask is placed in the RIE to etch the quartz
The quartz etched to the desired depth and the chrome stripped off

Fig. 2.3 Fabrication of Dammann gratings

The RIE is operated at 40 mTorr pressure with 80% CHF_3 and 5% O_2 flow rates in the chamber and an RF power of 140 Watts. This recipe etches the quartz at a rate of 400 A°/ min. Typical etch times for a grating designed to operate at 675 nm wavelength would be 18-19 minutes. The chrome layer holds up as a good mask to the plasma and prevents any etching of the underlying quartz substrate.

2.2.2. Reactive Ion Etching - Process Details

During the initial trials of fabrication plain photoresist was used as the masking layer in the RIE. But the presence of oxygen in the RIE gas plasma caused photoresist to etch as well. The etch rate of photoresist for the receipe used was around 200 A°/min.

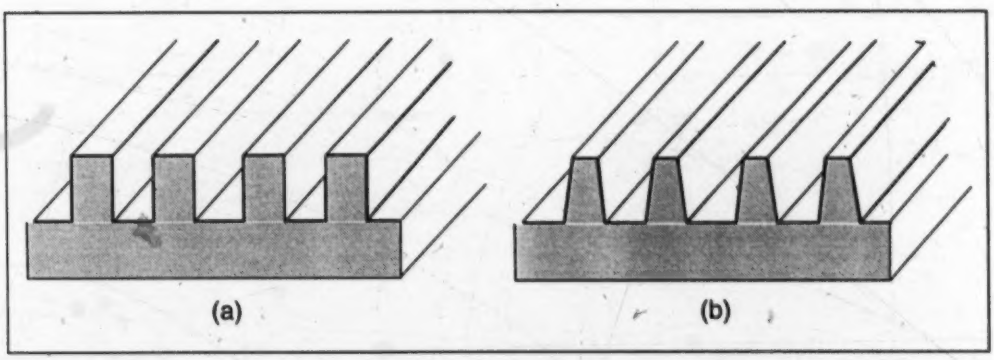

Fig. 2.4 (a) Desired etch profile (b) profile obtained by using a photoresist mask

So theoretically a 1 μm thick layer of photoresist could hold as a mask for 50 minutes or so and hence would be more than adequate for our purposes. However, when the quartz was etched with photoresist as the mask, the etched features had a trapezoidal profile rather than a rectangular one (see Fig. 2.4). This probably was due to the undercutting of the photoresist during the etch, caused by the ion bombardment and reflections of the quartz surface. To eliminate this problem chrome was used as the masking layer and the undercut was greatly reduced giving rise to a near rectangular profile as shown in Fig. 2.5.

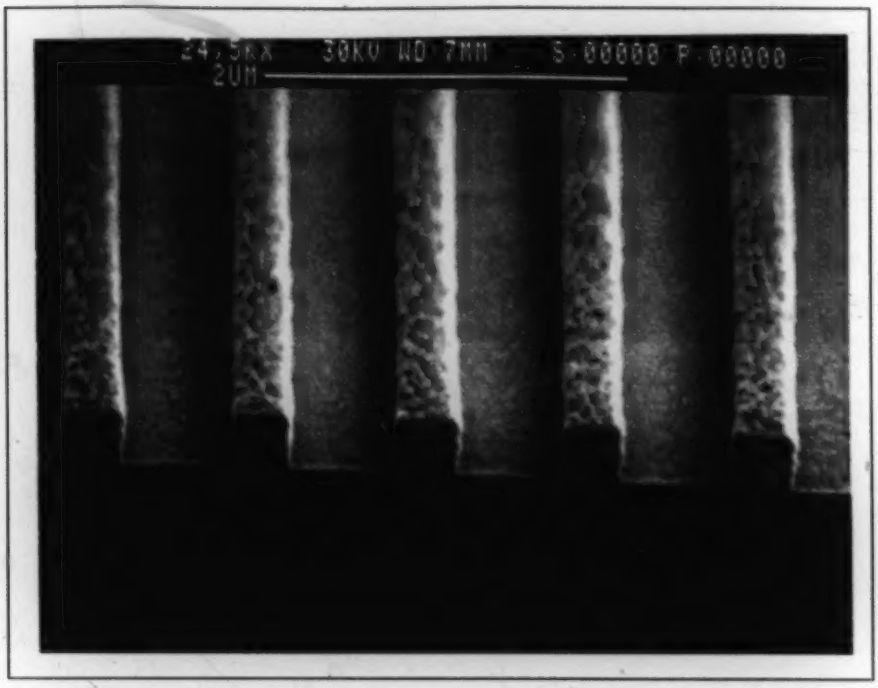

Fig. 2.5 SEM photograph of a grating etched in quartz with a chrome mask

As mentioned before, the reason the photoresist was etched was the presence of O_2 in the plasma. It therefore follows that absence of O_2 in the RIE chamber would prevent the photoresist from etching. This is true no doubt, but the absence of O_2 causes greater problems, as there might be residual microscopic particles of photoresist still left in the exposed and developed areas of the pattern and also sludge accumulation at the corners as shown in Fig. 2.6. Now when the RIE is done with only CHF3 the photoresist will polymerize and this would cause micro-mesas and other unwanted artifacts in the final device. Also, removing the polymerized photoresist poses another big problem as acetone would no longer be effective as a rinsing agent. In Fig. 2.7 is a SEM photo of a quartz substrate in which photoresist was employed as the mask and the RIE conducted with only CHF_3 plasma at 140 watts RF power and 40 mTorr pressure.

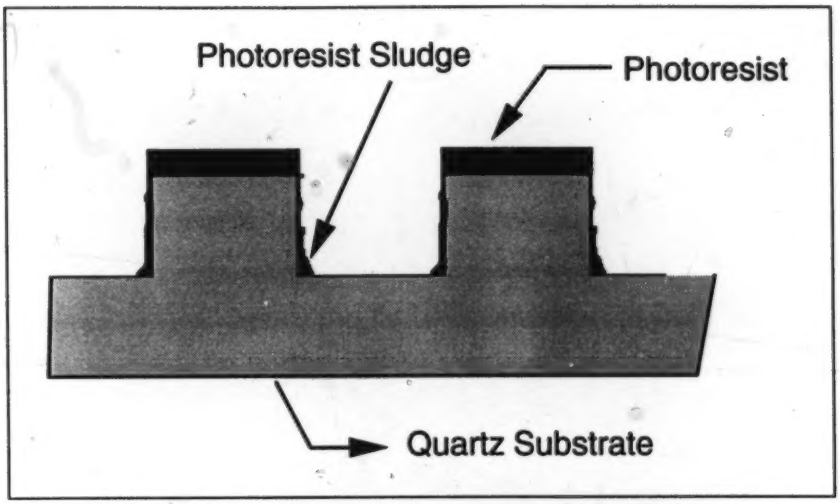

Fig. 2.6 Photoresist accumulation at the corners

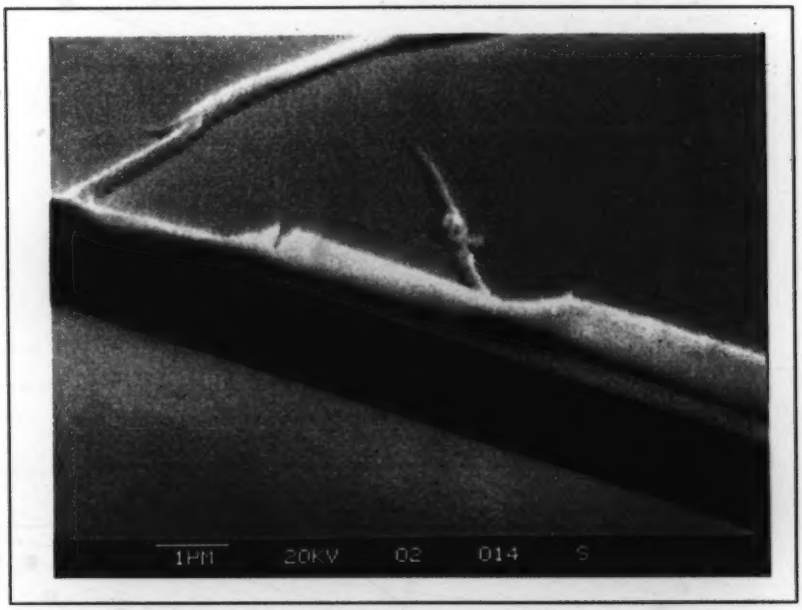

Fig. 2.7 Quartz etched with photoresist as mask and only CHF_3 plasma

The photoresist layers can still be seen in many parts of the device even though it has been thoroughly cleaned in acetone.

Another factor that influences the etching process is the chamber condition. Usually the walls of the RIE chamber would have adsorbed gases from previous runs and would be contaminated with many different kinds of gas molecules. In order to get repeatable results it is of paramount importance to clean the RIE chamber with an oxygen plasma. The recipe normally used to clean the chamber is 100% O_2 flow rate, 400 mTorr gas pressure and 300 Watts of RF power. A typical oxygen clean would be for 1/2 hour. Another important step is a chamber precondition or allowing the chamber walls to adsorb the gas molecules of the desired run. Before the sample is put into the chamber, the RIE is allowed to run for about 5 minutes with the same gas chemistry, pressure and power conditions as the actual run. Adherence to proper cleaning and preconditioning procedures helps in realising the desired repeatable results.

2.3 Test and Measurement Results of the 1:3 Gratings

The experimental setup used to test these gratings is shown in Fig. 2.8.

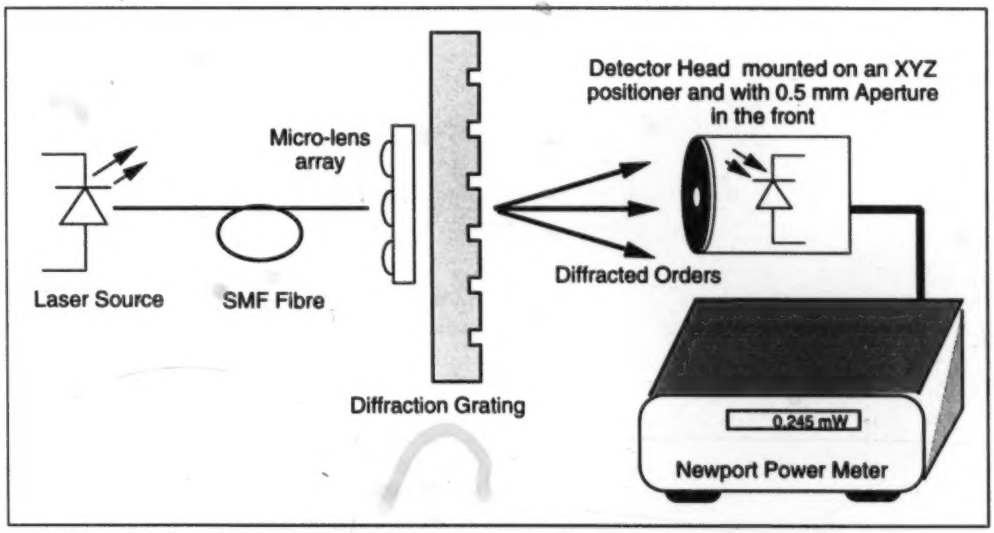

Fig. 2.8 Measurement set-up for testing the Dammann gratings

Light from the 675 nm laser was collimated by a F-2.6 microlens and passed through the grating. The light power in the diffracted orders was measured with the help of a Newport

power meter mounted on an XYZ positioner. A pin hole aperture is also placed in front of the detector head to avoid picking up the power from other diffraction orders. The intensity distribution for the 1:3 gratings fabricated with a photoresist mask and a chrome mask is shown in Fig. 2.9 and Fig. 2.10 respectively.

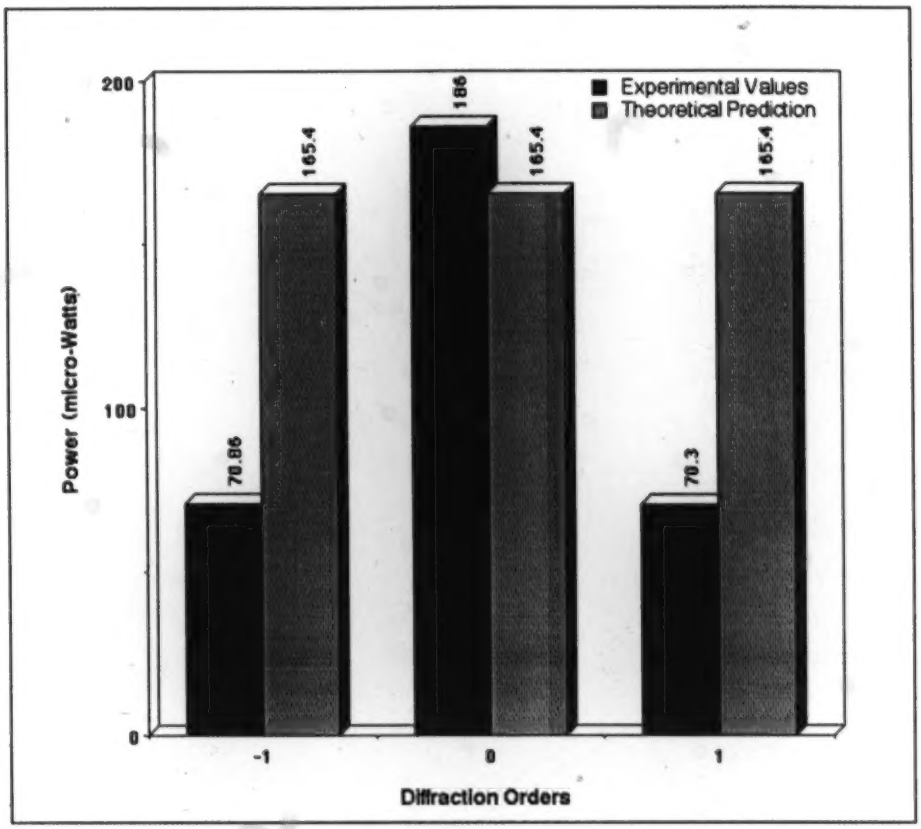

Fig. 2.9 Intensity distribution of a 1:3 Dammann grating fabricated with photoresist mask

With chrome masks the dramatic improvement in the uniformity of the intensities of the diffracted spots can easily be seen. The standard deviation with respect to the mean, between the intensities of the diffracted orders for the grating shown in Fig. 2.9 is 49.5% and that for the one shown in Fig. 2.10 is 2.1%. Theoretical efficiency of the 1:3 Dammann grating from Table 2.1 is 66.42%, and the measured value of efficiency for the grating of Fig. 2.10 is 66.2%. There is a close agreement between the predicted and measured values and this confirms the accuracy of the fabrication technique employed.

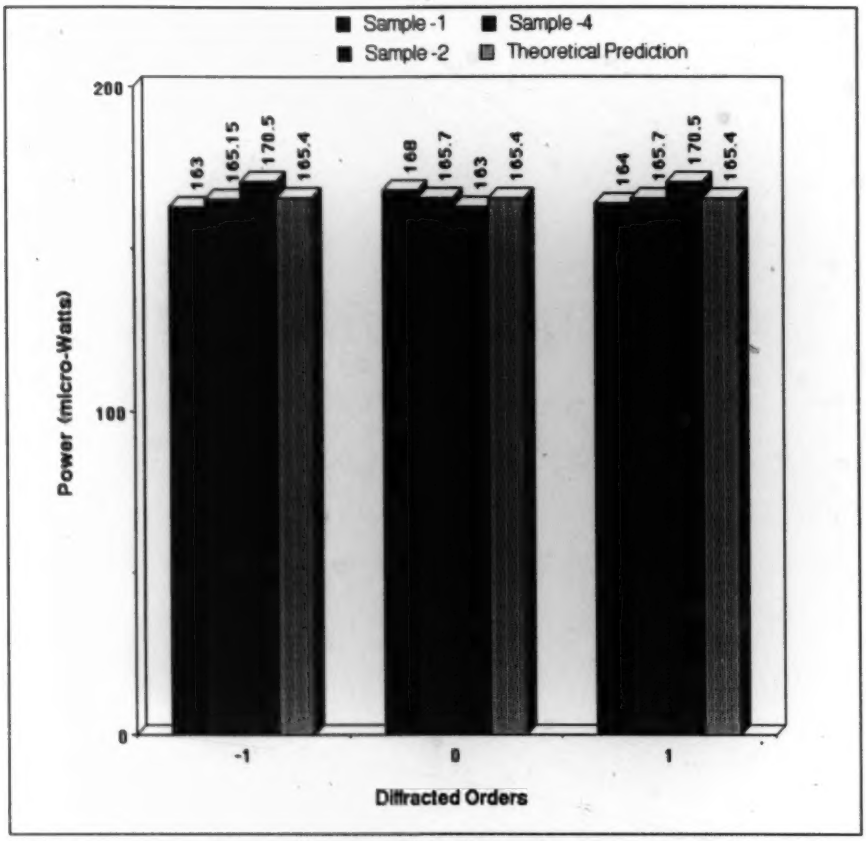

Fig. 2.10 Plot showing the uniformity of the intensity distribution of the 1:3 grating for three different samples

A CCD camera image of the diffraction orders for a 1:3 grating is shown in Fig. 2.11. The higher diffraction orders cannot be seen as they fall outside the field of view of the imaging system.

Fig. 2.11 Camera image of the far-field diffraction pattern of a 1:3 Dammann grating

In section 2.2 the importance of proper RIE techniques for repeatable performance was emphasized. The repeatability of the process can also be gauged from looking at Fig. 2.10 where the intensity distribution for a 1:3 diffraction grating has been compared for three samples fabricated at different times. There is little variation from sample to sample and they more or less conform to the theoretical prediction.

2.4 Design of Binary Gratings with Arbitrary Phase

2.4.1 Theory

The conventional Dammann gratings are capable of only 1:(2N+1) split ratios. Some applications require an even number of splits of the kind 1:2N, and this is possible employing non-symmetrical periods, i.e., structures where the transmittance function

$$T(x) \neq T(-x) \qquad 2.20$$

Designs of these types and those where the binary phase is allowed to have values (0, non-π), have been investigated by Killet et al [22]. Here, a general purpose 'C' program for designing binary gratings of arbitrary phase was written in order to obtain the exact design values and also to enable the study of fabrication errors on the diffraction pattern.

For an arbitrary phase non-symmetric binary grating, the transmittance function of Eq. 2.9 is modified to a more general form

$$T(x) = \sum_{l=0}^{N} e^{-jk_o(n-1)\,dMod[l]}\, rect\left[\frac{x-(x_{l+1}+x_l)/2}{x_{l+1}-x_l}\right]$$

$$0 \le x \le 1 \qquad 2.21$$

where

$Mod(l) \equiv 1$ if l is odd numbered and

$Mod(l) \equiv 0$ if l is of even numbered

Also for mathematical convenience the period is represented from 0 to 1 and the transition points x1, x2....xl are all positive valued (see Fig. 2.12).

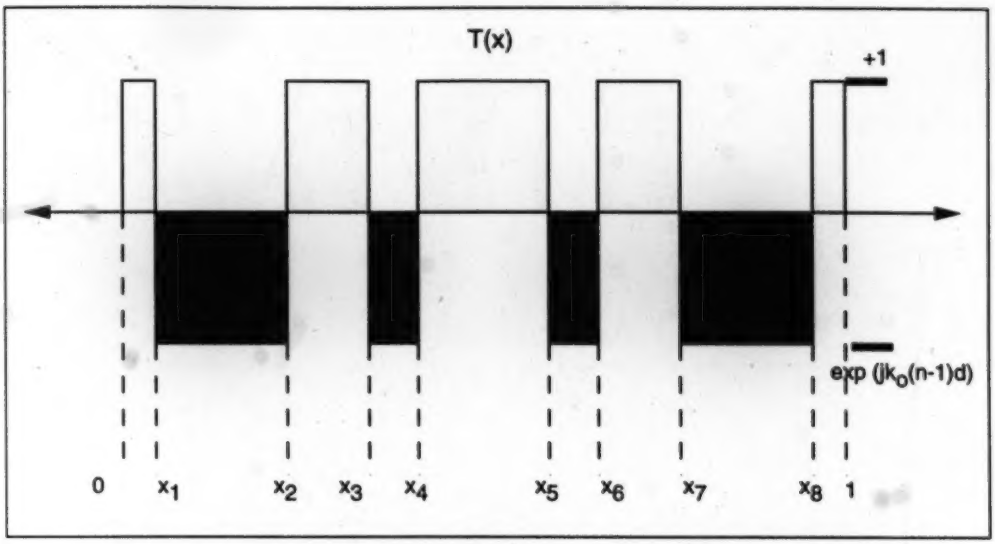

Fig. 2.12 Transmittance function of a generalized binary grating

The symmetric form of Eq. 2.9 is hidden in the general transmittance equation of Eq. 2.21. In the above form of representation for 2m+1 splits the number of cross-over points would be N = 2m in the interval $0 \leq x \leq 1$.

In this work it was required to design a 1:2 grating. The design had one transition point at x_1 =0.5 and the phase (0, $\Delta\Phi$) was found to be (0, π).

2.4.2 Experimental Results

The gratings designed had a period of 20 μm and were required to operate as a 1:2 grating at 850 nm, for applications described in chapter 4. From Eq. 2.5 the etch depth was calculated to be 923.9 nm. The fabrication technique used is similar to the process described in Fig. 2.3. The intensity distribution of the diffraction pattern is shown in Fig. 2.13.

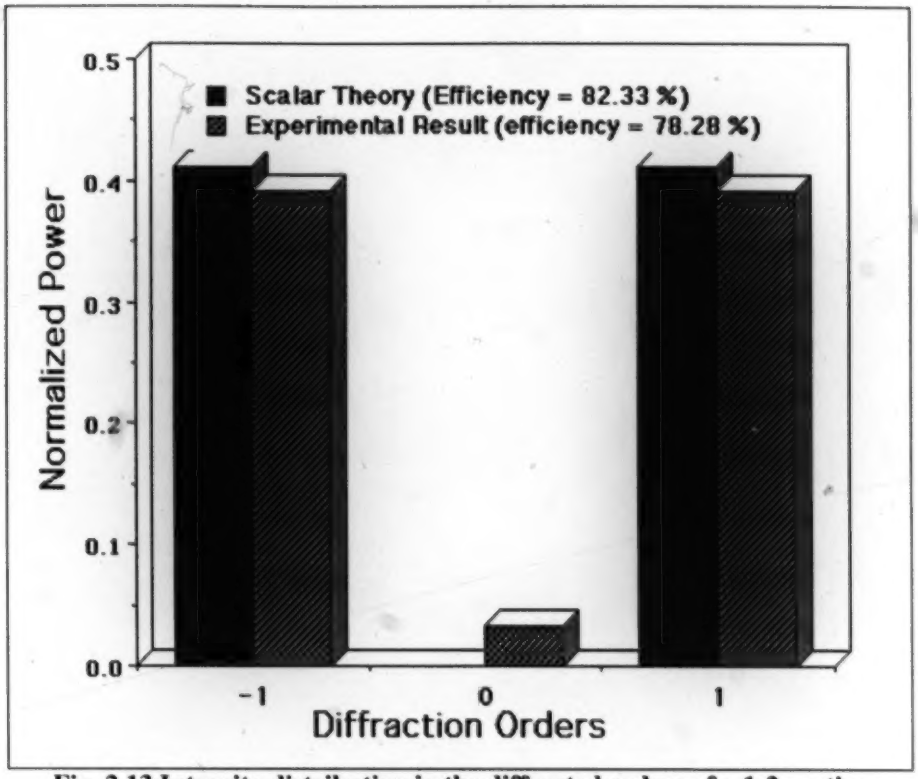

Fig. 2.13 Intensity distribution in the diffracted orders of a 1:2 grating

The power in the zeroth order is 13 dB below the power in the ± 1 diffraction orders and the efficiency is close to 78%. This is in quite close agreement to the theoretical value of 82%. A camera image of the far-field diffraction pattern is shown in Fig. 2.14. The small amount of power scattered into the unwanted zeroth diffraction order can also be seen in the image.

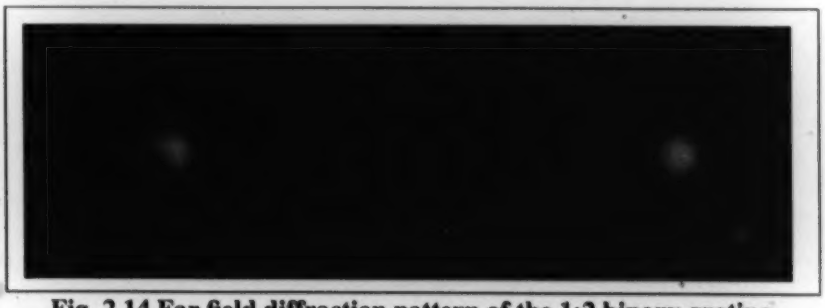

Fig. 2.14 Far field diffraction pattern of the 1:2 binary grating

2.4.3 Discussion

There is no doubt that even in the best controlled fabrication processes, there would still be certain errors because of the inherent tolerances associated with many of the fabrication steps. In the fabrication of the binary gratings there are two principal sources of error:(a) error in the patterning caused due to incorrect lithography or undercut during etching etc. (b) error due to the incorrect etch depth in the RIE. A simulation was done to study the effects of these errors on the diffraction pattern of a 1:2 grating. As mentioned in the previous section the 1:2 grating has been designed to have a period of 10 μm, so for x_1=0.5 the grating pattern would have 5 μm etched and 5 μm unetched portions in one period. The grating pattern was varied ± 2 μm and the etch depth was kept constant at 923.9 nm (phase shift π). The effects of this variation on the powers in the 0, ± 1 diffraction orders and the efficiency is shown in Fig. 2.15. It can be see that any error in the patterning results in a decrease in the efficiency and an increase in the power scattered into the unwanted 0 th diffraction order. However, for practical purposes the error in the patterning should be limited to < 5%.

The effect of an incorrect etch depth on the performance of the grating was also studied and is shown in Fig. 2.16. In this simulation the grating pattern was kept constant at the design value and the etch depth was varied ± 200 nm from the designed value of 923.9nm. This corresponds to approximately $\pm 40^{o}$ phase variation from the desired phase depth of 180°. It can be seen that the etch depth variation should be tightly controlled to less than 2% from the designed value.

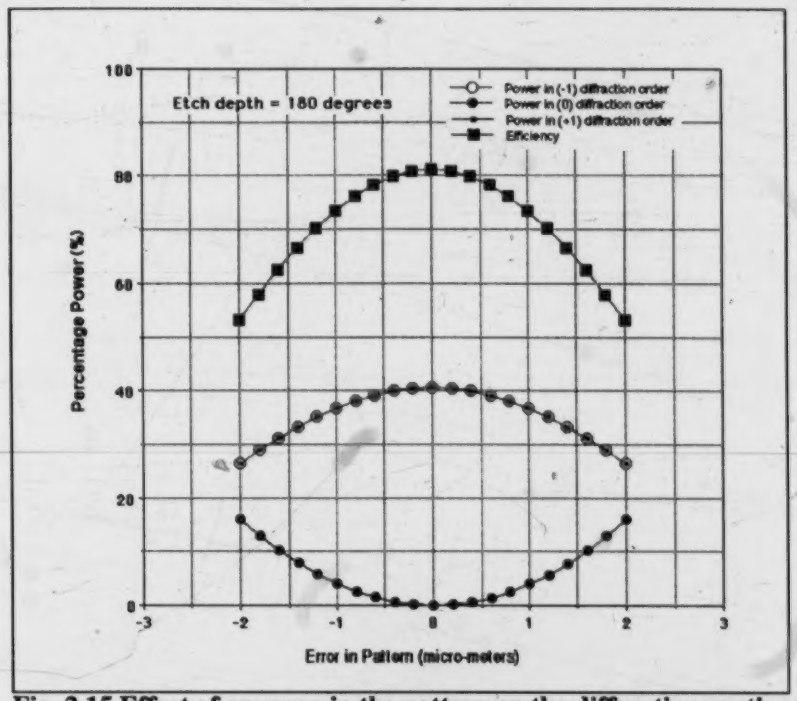

Fig. 2.15 Effect of an error in the pattern on the diffraction grating

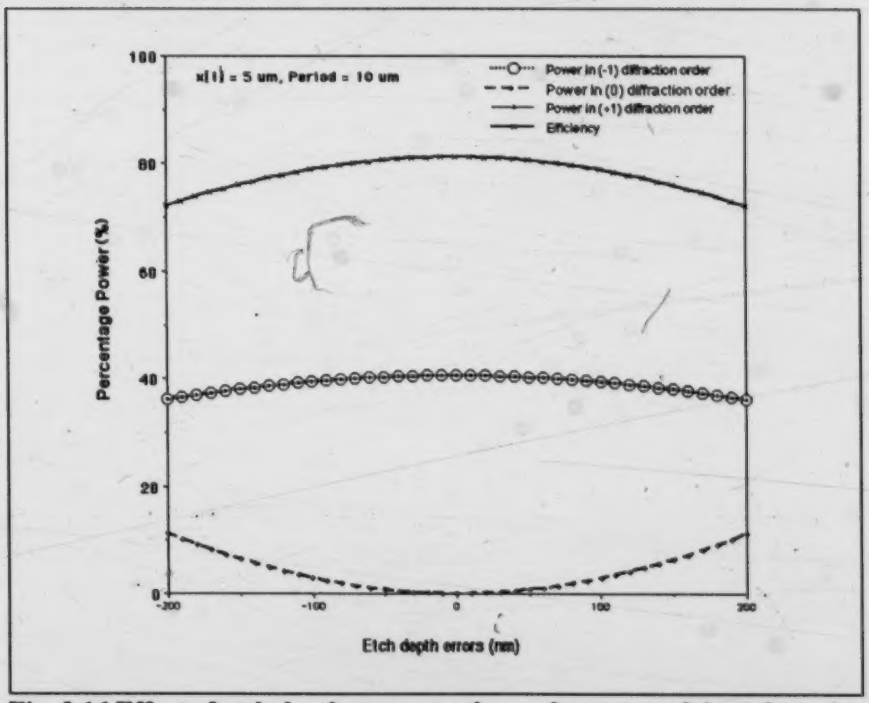

Fig. 2.16 Effect of etch depth errors on the performance of the 1:2 grating

It is an established fact that arbitrary phase binary gratings are either equal to, or more efficient than the $(0, \pi)$ class of binary gratings [26]. The reason $(0, \pi)$ gratings are still widely used for pattern generation is because of the moderate computational complexity involved in designing these gratings. A comparison of the different kinds of gratings with regards to their efficiency for different fan-outs is shown in Fig. 2.17 and is taken from Ref. [26]. The $(0, non-\pi)$ type of gratings are more efficient than the $(0, \pi)$ type and the continuous phase relief gratings are the most efficient. Therefore, if higher efficiency is desired, multilevel binary gratings that closely approximate the continuous phase gratings could be used at the expense of increased cost and complexity. The number of discrete phase levels in the multilevel system depends upon the number of masks used to pattern. If M masks are used, we can get 2^M quantized phase levels. The choice of the number of levels employed in designing a binary grating depends on the performance requirements, fabrication costs and yield.

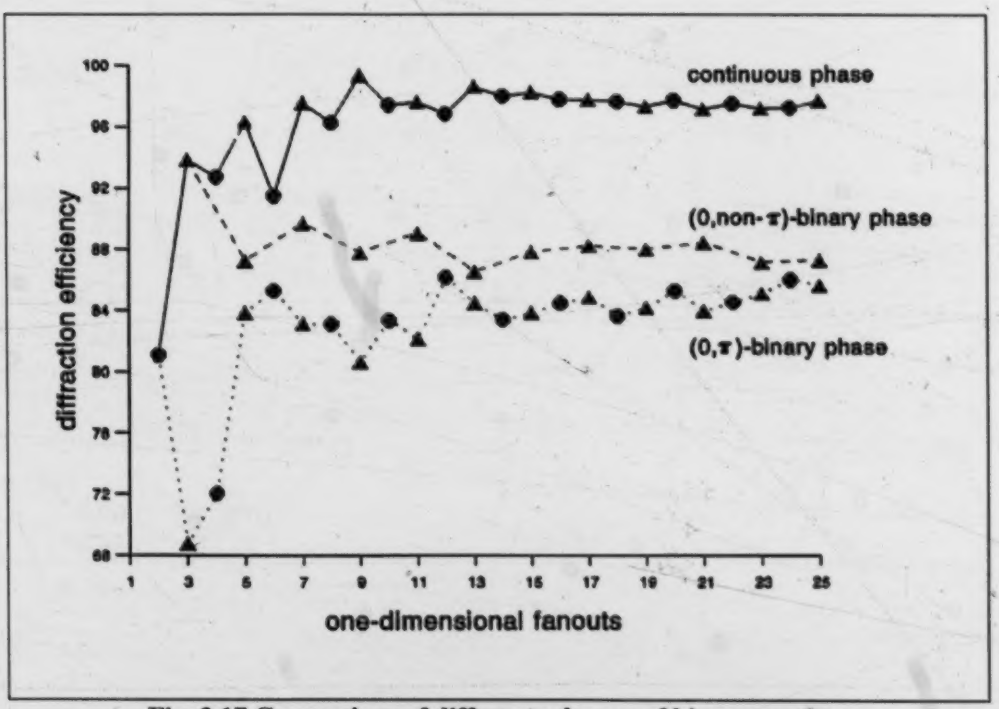

Fig. 2.17 Comparison of different schemes of binary gratings

Chapter 3

Design and Fabrication of V-Groove Gratings

3.1 Overview

For applications that demand beamsplitting where the phase of the beams is not important, Dammann gratings have received special attention because of their simple binary phase design and their fabrication using conventional VLSI processing technology[18]-[23]. Gratings fabricated using these techniques rarely achieve their theoretical efficiencies because of limitations in the fabrication processes. The two main limiting factors have been the uncertainty inherent in photolithography and etch depth errors when using RIE. The latter is still very empirical, requires a high degree of fabrication skill, and varies from installation to installation. At longer infrared wavelengths, photolithography errors are not as critical, especially with recent advances in submicron patterning techniques [27]. However, greater etch depths are required making the RIE process more difficult and time-consuming.

An etching technique that is self-limiting would reduce depth errors and lead to a simpler, more repeatable process. One such method is anisotropic etching of (100) crystalline silicon by ethylene diamine pyrocatechol (EDP) or potassium hydroxide (KOH) [28], which has been employed in the past for fabricating diffraction gratings [29], waveguides [30], and other integrated optical devices [32]-[33]. The basic principles of anisotropic etching of silicon is given are Appendix-A.

If gratings were fabricated using wet anisotropic etching techniques, control of the etch depth would no longer be a problem since the depth is proportional to the V-groove width which in turn is controlled by the surface photolithography and not the etch time. This means that designs involving multiple V-grooves per grating period with different depths can be fabricated with one lithography step and one etch step, or that completely different grating designs can be fabricated on the same wafer in the same etch step. Multiphase gratings fabricated this way should have the advantage of repeatability, and

reduced scattering because of the smooth sidewalls of the v-grooves.

In this chapter, a new technique for making Dammann-like transmission gratings for infrared light from periodically spaced V-grooves in silicon is described. In the next section, the theory of transmission gratings utilizing silicon v-grooves is developed and applied to the design of 1:N equal intensity beamsplitters[39].

3.2 Grating Design and Scalar Diffraction Theory

Let us consider gratings composed of periodically etched V-grooves. The theory is demonstrated by a simple grating structure with one V-groove of half-width x_1 per period L on a silicon substrate of thickness D (Fig. 3.1). The extension of the analysis to structures with more than one groove is straight forward. The anisotropic etching of (100) silicon produces grooves with sidewalls of slope $s = \sqrt{2}$. The shaded region of Fig. 3.1 is an overlayer of index n_2, which is intermediate to the indices of silicon and air.

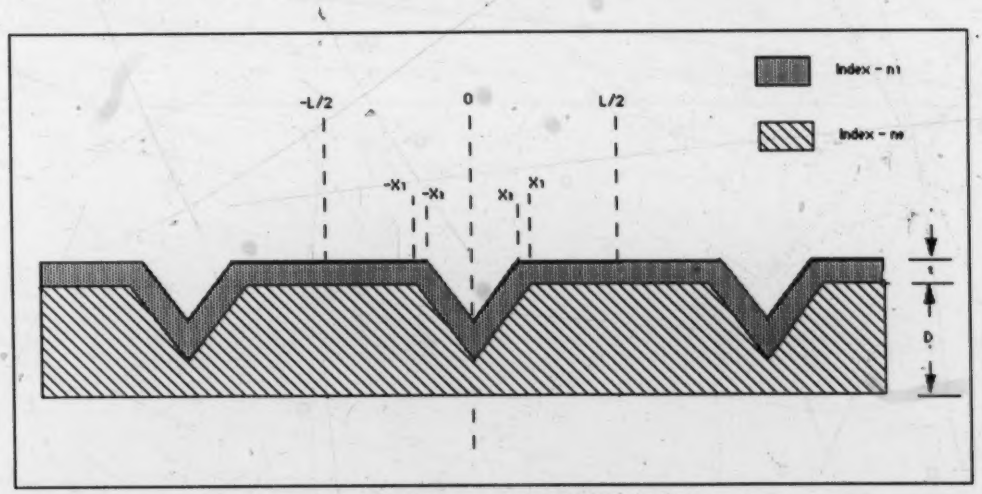

Fig. 3.1 Structure of a grating with grooves etched in silicon, index n_0, and covered with a material of index n_1

The purpose of this layer, which would be deposited after the v-grooves have been etched, is to reduce Fresnel reflections and improve the diffraction efficiency by suppressing higher diffraction orders. Its thickness, t, is assumed to be constant in the direction normal

to the silicon surface. The validity of this assumption will depend on the method of deposition but is approximately true with chemical vapor deposition of SiO_2 on silicon [30]. The half-width of the grooves in the overlayer, x_2, is then

$$x_2 = x_1 - \left(\sqrt{3}-1\right)(t/s) \quad \text{when } t \le x_1 s/\left(\sqrt{3}-1\right), \tag{3.1}$$

$$= 0 \qquad \text{when } t > x_1 s/\left(\sqrt{3}-1\right). \tag{3.2}$$

Using simple scalar diffraction theory, the transmittance function T(x) is a product of the transmittances of the substrate(thickness $d_0(x)$ and index $n_0 = 3.5$), of the overlayer (thickness $d_1(x)$ and index n_1) and of the air (thickness $d_2(x)$ and index $n_2 = 1$) in the groove. The thicknesses for the three different materials are

$$d_0(x) = \begin{bmatrix} D + s(|x| - x) & 0 \le |x| \le x_1 \\ D & x_1 < |x| < \frac{L}{2} \end{bmatrix} \tag{3.3}$$

$$d_1(x) = \begin{bmatrix} t & x_1 \le |x| \le T/2 \\ t + s\left(x_1 - |x|\right) & x_2 \le |x| < x_1 \\ t\sqrt{3} & 0 \le |x| < x_2 \end{bmatrix} \tag{3.4}$$

$$d_2(x) = \begin{bmatrix} s(x_2 - |x|) & |x| < x_2 \\ 0 & x_2 \le |x| < \frac{L}{2} \end{bmatrix} \tag{3.5}$$

and the transmittance is then found to be

$$T(x) = exp\left[-j\frac{2\pi}{\lambda_o}\left[n_0 d_0(x) + n_1 d_1(x) + n_2 d_2(x)\right]\right] \tag{3.6}$$

and repeated every L. Expressing T(x) as a Fourier series, the amplitude of the p^{th} diffraction order is just the series coefficient, A_p, given by

$$A_p = \frac{1}{L}\int_{-\frac{L}{2}}^{\frac{L}{2}} T(x)\, exp\left[-2\pi jp\frac{x}{L}\right] dx \qquad 3.7$$

Since the phase is piecewise linear with x, analytic expressions can be obtained for the Fourier coefficients. However, the expressions are very complicated and even more so for the structures with more V-grooves per period such as those considered in this work. An alternative approach followed in this work is to evaluate A_p numerically by a 'C' program for the few coefficients that are required.

Let us now consider the design of gratings which generate (2N+1) beams of equal intensity. Ideally, the coefficients of the diffraction orders would satisfy

$$|A_p|^2 = \frac{1}{(2N+1)} \qquad 3.8$$

for $|p| \le M$ with all other coefficients zero, but this is impossible to obtain in practice. Instead, a brute force search is performed for the grating parameters (groove widths, positions, overlayer thickness if any) that minimize the standard deviation normalized with respect to the mean of the desired diffraction orders

$$\sigma = \frac{1}{\langle A^2\rangle}\left[\frac{1}{2N}\sum_{p=-N}^{N}\left(|A_p|^2 - \langle A^2\rangle\right)^2\right]^{1/2}, \qquad 3.9$$

where $<A^2>$ is the arithmetic mean of the intensities of the desired diffraction components.Typically there are several local minima in the standard deviation and then the diffraction efficiency, η, which is defined by

$$\eta = \sum_{P=-N}^{N} |A_p|^2, \qquad 3.10$$

should be as large as possible. There are limits over which the parameters can vary. For example, the period cannot be less than the wavelength if non-zero diffraction orders are to propagate into air, and the groove widths and positions must be such that no grooves overlap. The overlayer thickness t is bounded above by $x_1 s/\left(\sqrt{3}-1\right)$ since adding more

material after the grooves are filled will result only in a constant phase shift across the wave front. Finally, the coefficients for positive and negative are automatically equal if multiple grooves are placed symmetrically in the grating period. The optimization procedure is now applied to the design of a 1:3 beamsplitter (N = 1) for 1.55 μm light. First, it is assumed that the overlayer completely fills the grooves and L is held constant while x_1 is varied in incremental steps of 0.01 μm. The standard deviation and efficiencies as a function of x_1 for several values of L are shown in Fig. 3.2 and Fig. 3.3 respectively.

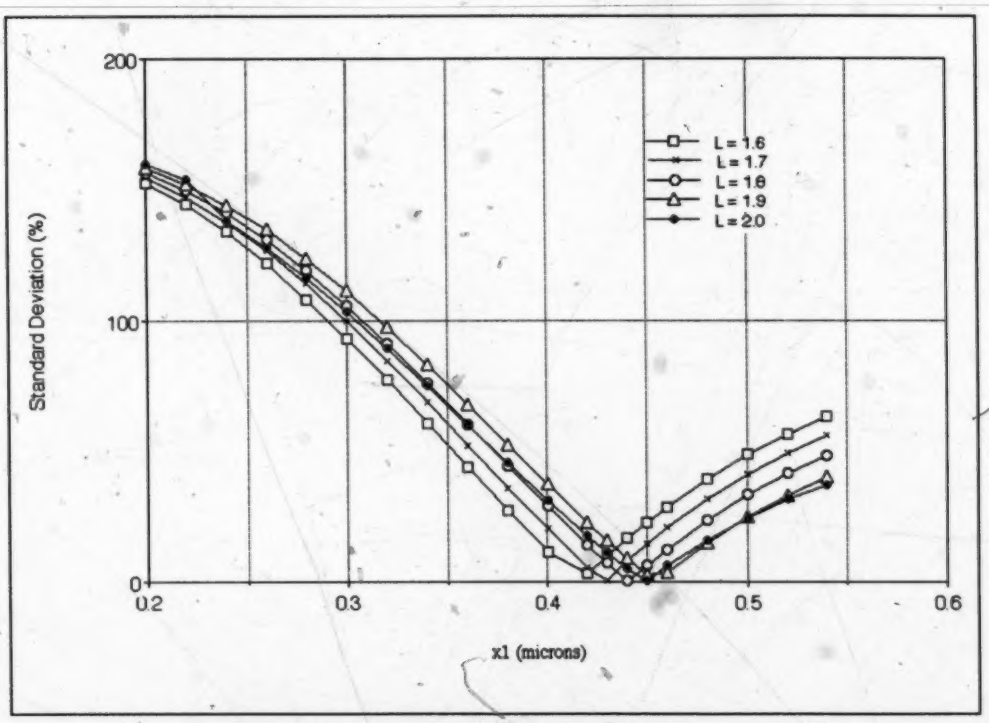

Fig. 3.2 Standard deviation with respect to the mean of the p = -1, 0, 1 diffraction orders as a function of the grating half-width for five values of the grating period. Length units are micrometers (μm)

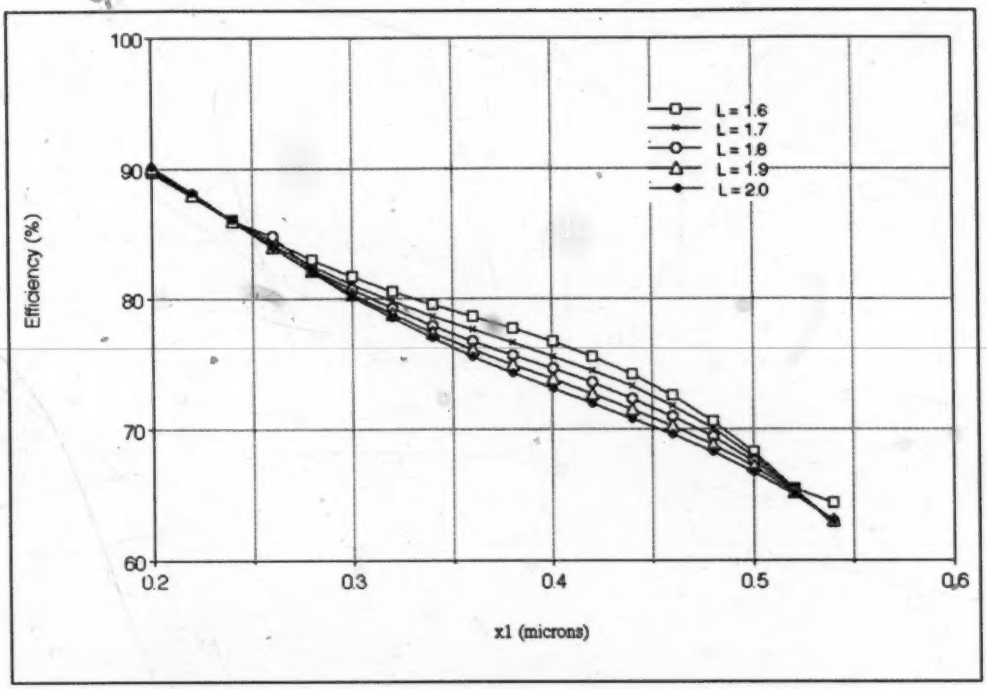

Fig. 3.3 Diffraction efficiencies for the same cases as Fig. 3.2

In all cases, there is an x_1 at which the standard deviation vanishes indicating that the intensities of the three lowest orders are equal. Efficiencies in the range 70% to 75% are found and it can be seen that the efficiency decreases as the period increases and that efficiency can be gained at the expense of uniformity.

The effect of varying the overlayer thickness, t, and refractive index, n_1, was studied and the results are presented in Fig. 3.4. For fixed values of t and n_1, x_1 was searched until the standard deviation fell below 5%. For each n_1, the maximum efficiency (the far right of each curve) occurs when the grooves are completely filled up, that is when $x_2 = 0$.

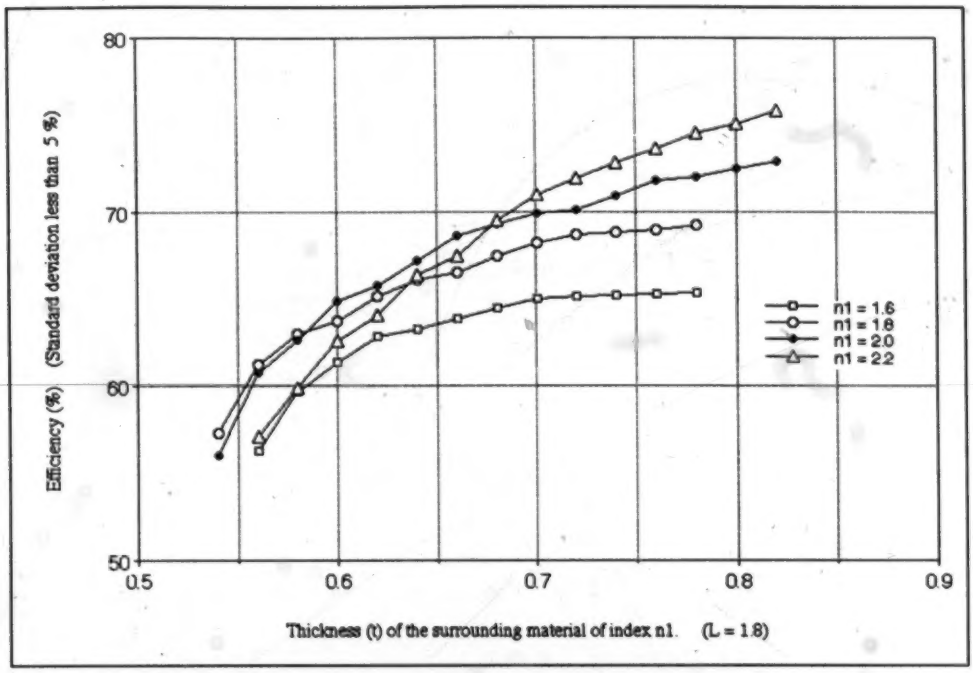

Fig. 3.4 Optimized grating efficiencies as function of overlayer thickness for several values of overlayer index of refraction

The results clearly show that the efficiency improves as the index increases. For an index of 2.9, the optimized value is reached at the maximum allowable x_1, L/2, and for higher indices there is no optimum solution. The apparent reason for this is that the phase change through the grooves is too small and most of the power is concentrated in the zeroth diffraction order.

3.3 Gratings Replicated From a Silicon Master

An alternative approach is to implement V-groove gratings in lower index materials. The fabrication involves etching a silicon master and replicating the gratings by the use of special photocurable polymers or plastics that would be removed after hardening [40]. The need for a lower index overlayer is removed, and the gratings can now be designed for wavelengths that are below the infrared region. The question of the optimum choice of materials is not addressed here. The analysis must be modified slightly since the

grooves become bumps in the finished grating. In searching for optimum designs, it was found that solutions with small standard deviation could be found for 1:(2N+1) beam splitters only if there were N grooves per period. As shown in Fig. 3.5, the grooves are symmetrically placed so that the positive and the negative orders automatically have the same amplitude. When searches were made without the assumptions of symmetry, the optimum solutions were symmetrical.

Results of the optimization of the 1:2, 1:5, and 1:7 beam splitters of index 1.5 for a wavelength of 780 nm are given in Table 3.1 as the coordinates of the groove edges. In each case, a grating period was assumed, and longer periods were assumed for the larger splitting ratios to accommodate the higher diffraction orders. One result that emerged is that, as N increases, the required minimum feature size for a desired standard deviation decreases. In searching for the optimum 1:5 splitter, solutions with slightly higher efficiency were found when a shorter period was assumed, but these also required a much smaller feature size. The standard deviation obtained for a 1:5 solution was 5%. For a 1:7 splitter, the lowest standard deviation found was 7% and this required a minimum feature size of 0.1 μm.

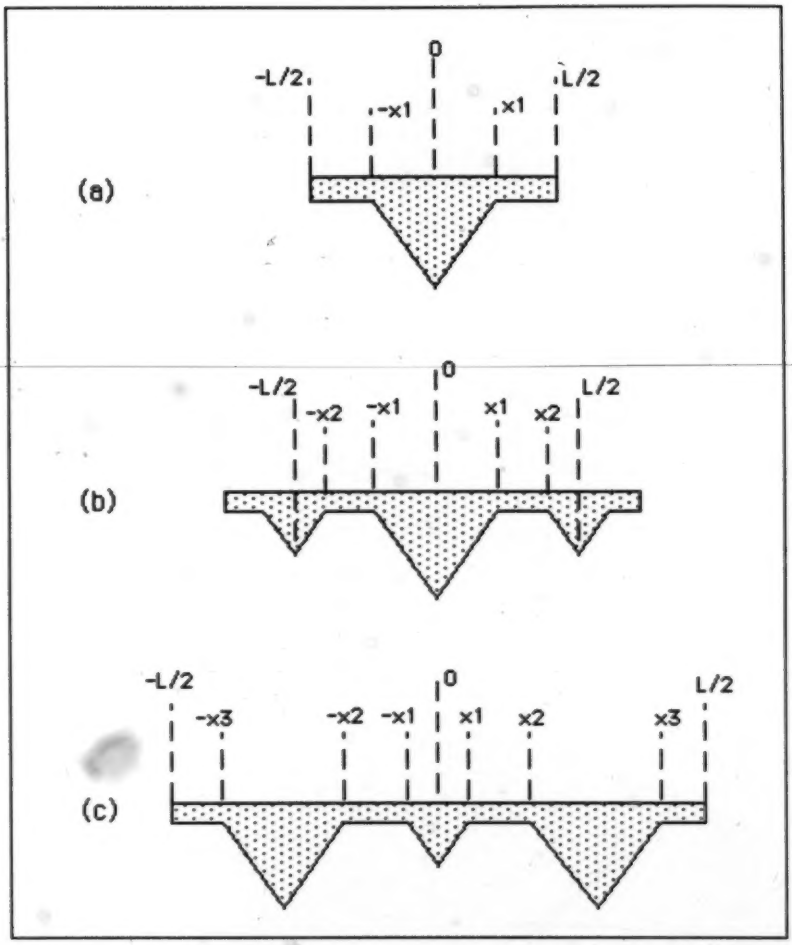

Fig. 3.5 Grating profile for generation of (a) 1:3, (b) 1:5, (c) 1:7 beam splitters

Table 3.1

N	Period (microns)	x1, x2, x3 (microns)	Efficiency (%),	Minimum feature size (microns)
1	1.6	0.55	87	0.5
2	3.2	0.4, 0.8	65	0.4
3	4.2	0.1, 0.65, 2.05	82	0.1

The tolerance of the optimized designs to variations in groove widths was studied, and the results for 1:5 beam splitters are shown in Fig. 3.6 as variations of the efficiency and standard deviation as one groove width is varied away from is optimum value while the other is held constant. It can be seen that a 0.1 μm error in width results in a decrease in uniformity to approximately 20%. The efficiency is rather insensitive to changes in the smaller groove width and can actually be increased at the expense of uniformity by a decrease in the larger groove width.

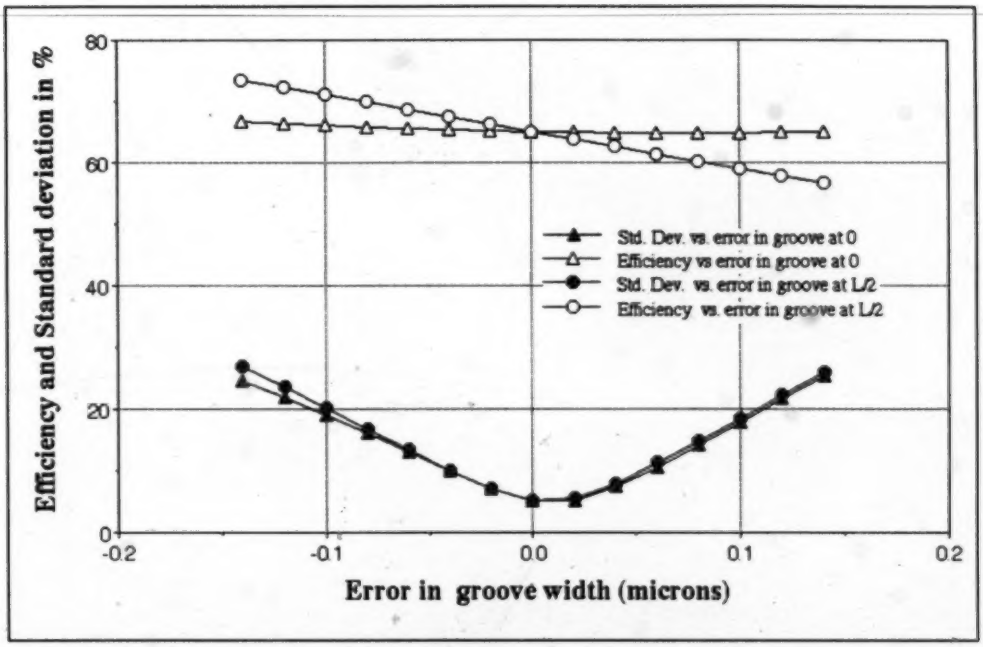

Fig. 3.6 Effect of fabrication errors on the efficiency and the uniformity of replicated gratings

3.4 Fabrication of V-groove Gratings

It was mentioned in the previous section that if the V-groove gratings were to be replicated in a low index material to form V-bumps, then, beamsplitters can be made for the wavelengths below the infrared as well. But the technology involved in replication is quite involved as it is similar to injection moulding and many of the existing techniques are

well protected under patent laws.

In order to test the principle a round-about technique of fabricating a 1:3 V-bump grating in a silicon nitride (Si_3N_4) was conceived and implemented. For the 1:3 grating, the period was chosen to be 1.8 μm and the groove width was calculated to be 0.8 μm for an operating wavelength of 780 nm. The major steps involved in the fabrication are shown in Fig. 3.7 and is a rigorous exercise in micro-machining [41].

3.4.1 Substrate Preparation

As the grating has sub-micron features it is imperative that electron-beam (e-beam) lithography techniques be used in order to pattern the gratings. At AMC, a SEM has been reconfigured to act as an electron beam writer under computer control. But unlike a commercial e-beam writer which can write masks over an area of 5 inch^2, the present set-up is limited to an area of 1 mm^2. Also the samples to be patterned should be about 1 cm^2, i.e., about the size that can be mounted on a SEM mounting stub. In the first step wet-thermal oxide of about 0.7 μm thickness is grown on a batch of (100) silicon wafers. This layer would serve later as the masking layer during the anisotropic etching of silicon. The substrate is then dipped into a buffered oxide etch (BOE) solution to etch back the SiO_2 layer from 0.7 μm to 0.1 μm. The reason for this etch is explained later. The BOE, which essentially is hydroflouric acid (HF), etches the SiO_2 at a rate 500 A^o/min. But this rate may vary with age and from sample to sample. The resist used for e-beam patterning is polymethyl methacrelate or PMMA for short. A 5% solution of PMMA is spun onto the wafer at 5000 rpm to give a coat of 0.5-0.6 μm. The substrate is then hard-baked in the oven at 150 ^{o}C for one hour and then soft-baked in vacuum for 40 seconds. The wafer has to be cleaved carefully along the (110) flats into 1 cm^2 squares. If cleaved properly, the sides of the squares then represent the (110) plane and could be used for alignment in the e-beam writer.

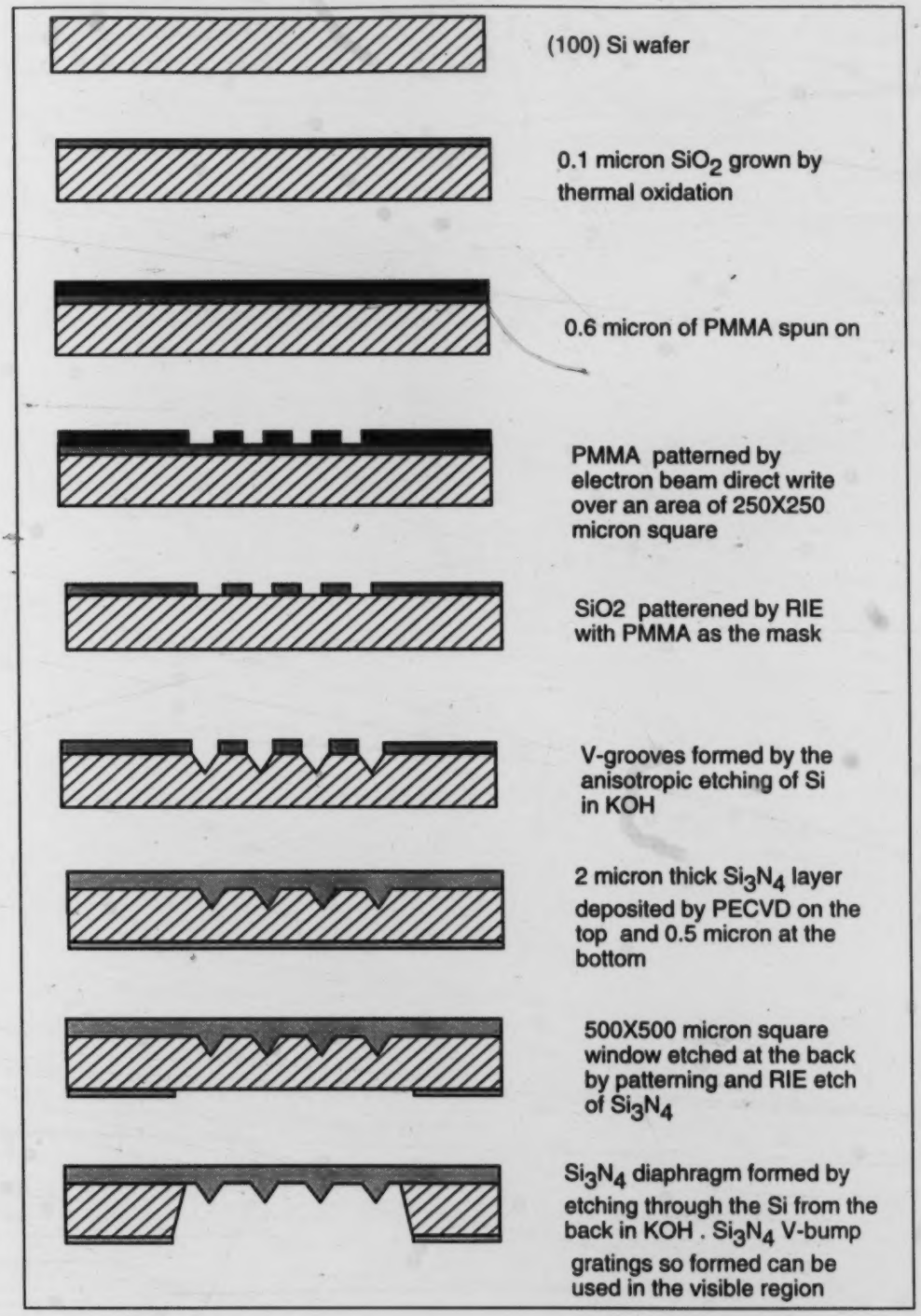
(100) Si wafer
0.1 micron SiO_2 grown by thermal oxidation
0.6 micron of PMMA spun on
PMMA patterned by electron beam direct write over an area of 250X250 micron square
SiO2 patterened by RIE with PMMA as the mask
V-grooves formed by the anisotropic etching of Si in KOH
2 micron thick Si_3N_4 layer deposited by PECVD on the top and 0.5 micron at the bottom
500X500 micron square window etched at the back by patterning and RIE etch of Si_3N_4
Si_3N_4 diaphragm formed by etching through the Si from the back in KOH . Si_3N_4 V-bump gratings so formed can be used in the visible region

Fig. 3.7 Processing steps in the fabrication of V-bump silicon nitride gratings

3.4.2 Substrate Patterning

The silicon pieces are mounted on the mounting stubs using carbon graphite paste. The substrate is properly aligned inside the SEM such that the e-beam will write the patterns parallel to the (110) sides. The beam dosage used is 150 $\mu C/cm^2$ and the acceleration voltage used is 40 KV. The desired pattern is first generated using the software L-EDIT and then converted to an e-beam writer run file, which is then used to generate the pattern. The total area exposed is 250 μm^2 and the total amount of time required is approximately 7 minutes. In order to cut down the writing time larger patterns are avoided. The sample is then developed in a MIBK/IPA solution for one minute and then IPA for 20 seconds and then rinsed with de-ionized (DI) water. A SEM photograph of the patterned PMMA is shown in Fig. 3.8.

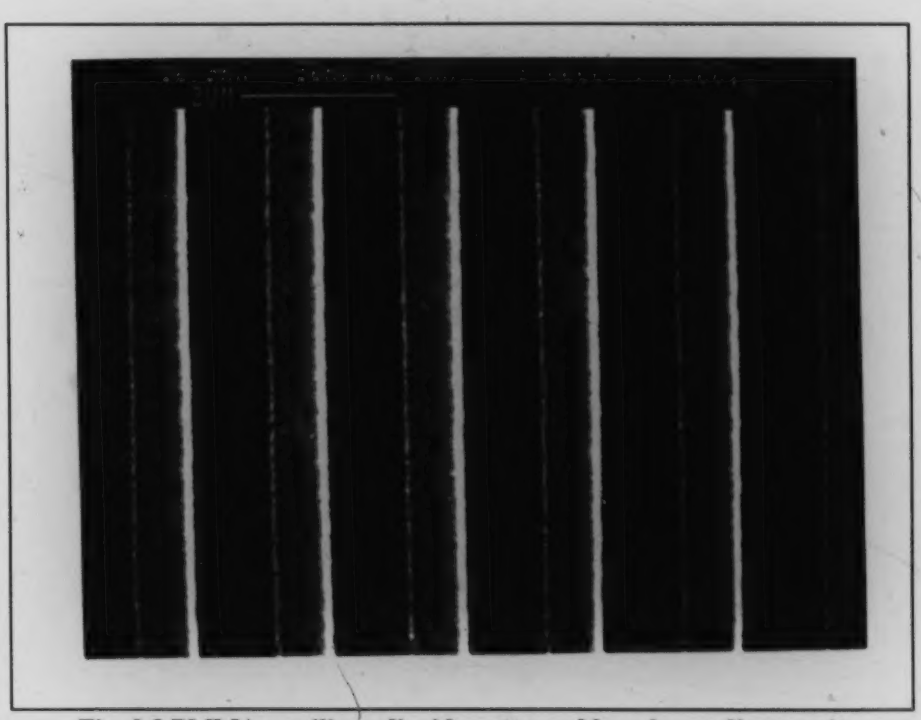

Fig. 3.8 PMMA on silicon dioxide patterned by e-beam direct write

The grating pattern on the PMMA is then transferred to the underlying oxide layer in the RIE. The recipe used in the RIE is 80% CHF_3, 5% O_2 at 40 mTorr pressure and 140 Watts of power. The SiO_2 is etched at a rate of 400 A°/min and the PMMA at 1000 A°/min. Therefore, in order to etch the 0.1 μm of SiO_2, 3 minutes of etching is sufficient, and in this duration only 0.3 μm of PMMA is etched. As PMMA is not a very good masking layer for most common etchants and etches almost three times faster than SiO_2 in the RIE, only a thin oxide layer can be patterned. It is for this reason that the SiO_2 was etched back to 0.1 μm from 0.7 μm during the substrate preparation. Fig. 3.9 shows a SEM photograph of the patterned SiO_2.

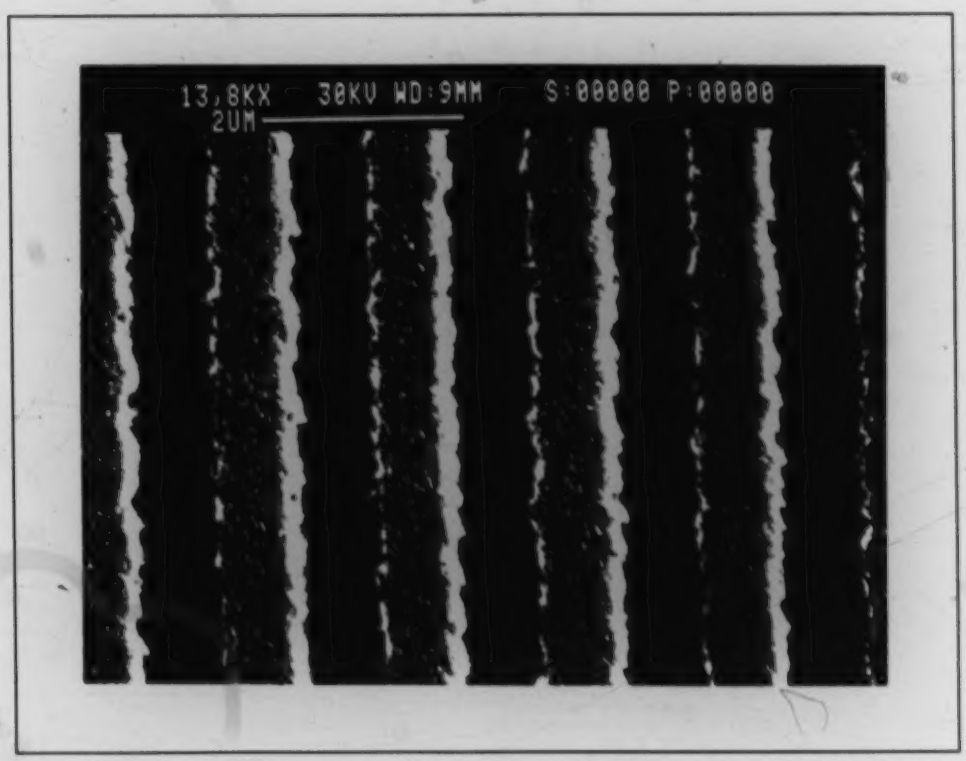

Fig. 3.9 Silicon dioxide pattern on (100) silicon, transferred from PMMA by RIE

There is a noticeable sidewall roughness which is inherent in the RIE process, but this is removed in the next step, the V-groove formation by anisotropic etching.

3.4.3 Sub-micron Micromachining of Silicon

After patterning, the sample was dipped in a 30% wt. concentration KOH solution for etching. The etch was carried out at 80 ^{o}C and the etch rate in the vertical <100> direction varied between 0.8 and 1.2 μm/min, depending upon the batch and the age of the etchant. As the openings in the SiO2 mask were 0.8 μm wide, the depth of the V-groove in the <100> direction would be 0.56 μm. The sample was etched for 2-3 minutes, even though this etch time is much longer than required, in order to get rid of any native oxide that might have formed on the surface of the silicon. Fig. 3.10 is a SEM photo of the V-grooves etched. It can be seen that sides of the V-grooves are very smooth and any roughness in the patterning stage has been removed by the crystallographic selective etch.

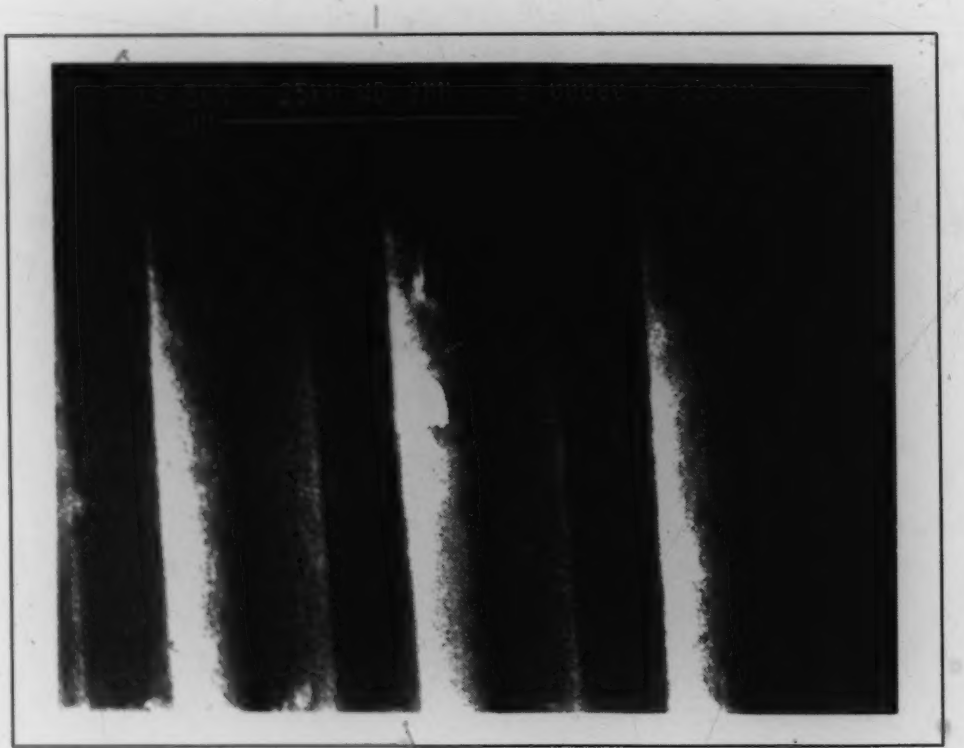

Fig. 3.10 V-grooves formed after the anisotropic etching in 30% KOH at 80^{o}C

However, if there is any misalignment with the (110) flats during the writing process, undercutting will occur until the etch front reaches the slowly etched {111} planes. This will occur in a series of plate like steps as shown in Fig. 3.11. The residual SiO_2 is stripped off and a 2 μm thick layer of Si_3N_4 is deposited by plasma chemical vapor deposition (PECVD) on the V-grooves so that the grooves are completely filled up.

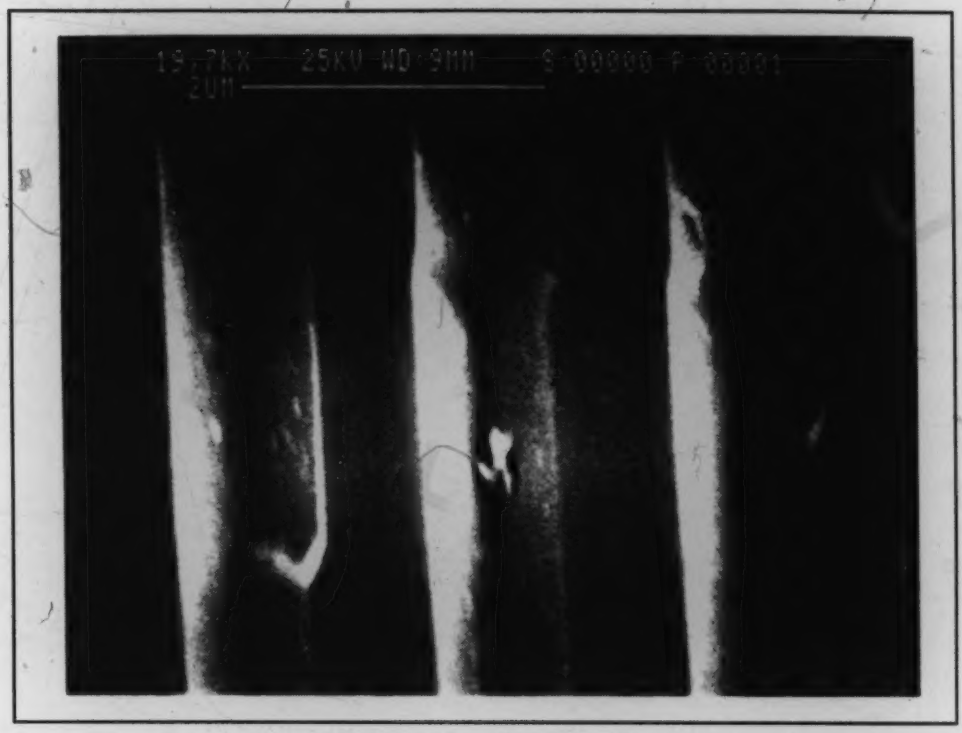

Fig. 3.11 Formation of plate like structures due to misalignment of the pattern with (110) flats

The wafer is then turned over and a 0.5 micron thick Si_3N_4 layer is deposited at the back of the silicon substrate. A silicon wafer which has pre-etched 500 X500 μm square holes, is used as a contact mask to pattern an opening in the Si_3N_4 layer at the back of the substrate in the RIE (see Fig. 3.7). The recipe used to etch the exposed Si_3N_4 in the RIE is 50% carbon tetrafluoride (CF_4) at 50 milli-Torr and 60 watts of RF power. The etch was carried out for 5 minutes at an etch rate of 1200 A°/min. The wafer was once again dipped in a

KOH solution at 80° C for 6-8 hours to etch right through the 500 μm thick silicon wafer. The etching will stop once the Si_3N_4 layer on the front side is encountered, and this results in the formation of a Si_3N_4 diaphragm with the V-bump gratings hanging on the underside. The 0.5 micron Si_3N_4 layer at the back stands up as a good mask over such long etch periods and is practically inert to KOH. The SEM photographs of the fabricated sub-micron Si_3N_4 V-bumps are shown in Fig. 3.12. The smooth surface of the gratings can also be observed in the photograph.

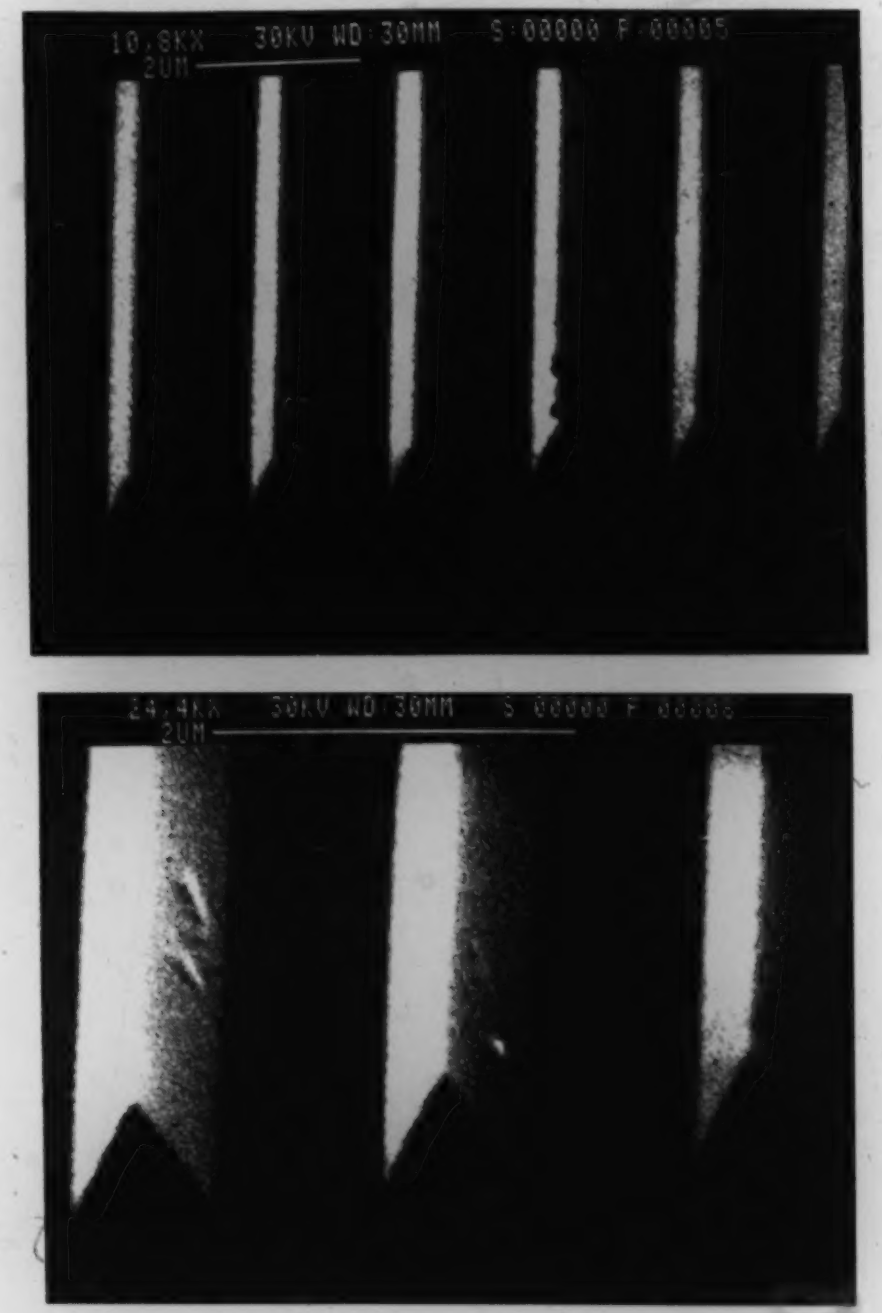

Fig. 3.12 Silicon nitride V-bump gratings formed on a 2 μm thick diaphragm

3.5 Experimental Results and Discussion

The scalar theory prediction of the performance of the grating at different wavelengths is shown in Fig. 3.13. The grating was tested at two wavelengths, namely 675 nm and 1300 nm. The experimental setup used to test these gratings is similar to the one shown in Fig. 2.8.

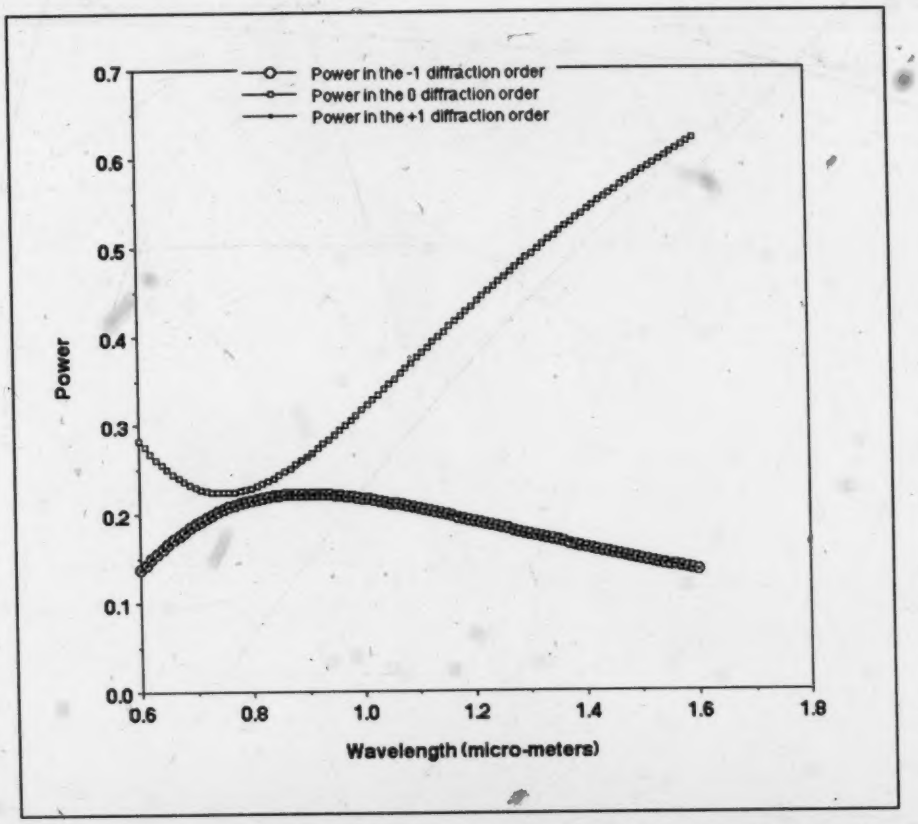

Fig. 3.13 Intensity distribution of the -1, 0, 1 diffracted orders for the Si_3N_4 V-bump grating at different wavelengths as predicted by scalar theory

The results are shown in Fig. 3.14 and Fig. 3.15. These gratings are designed to work as 1:3 equal intensity splitters at 780 nm and experimental results at that wavelength are not available due to the lack of a single mode source at that wavelength. However the performance of the gratings at other wavelengths is a good indicator for evaluation. From Fig. 3.14 and Fig. 3.15, it could be observed that there is some discrepancy between the pre-

dicted and the experimental results which may be due to many reasons.

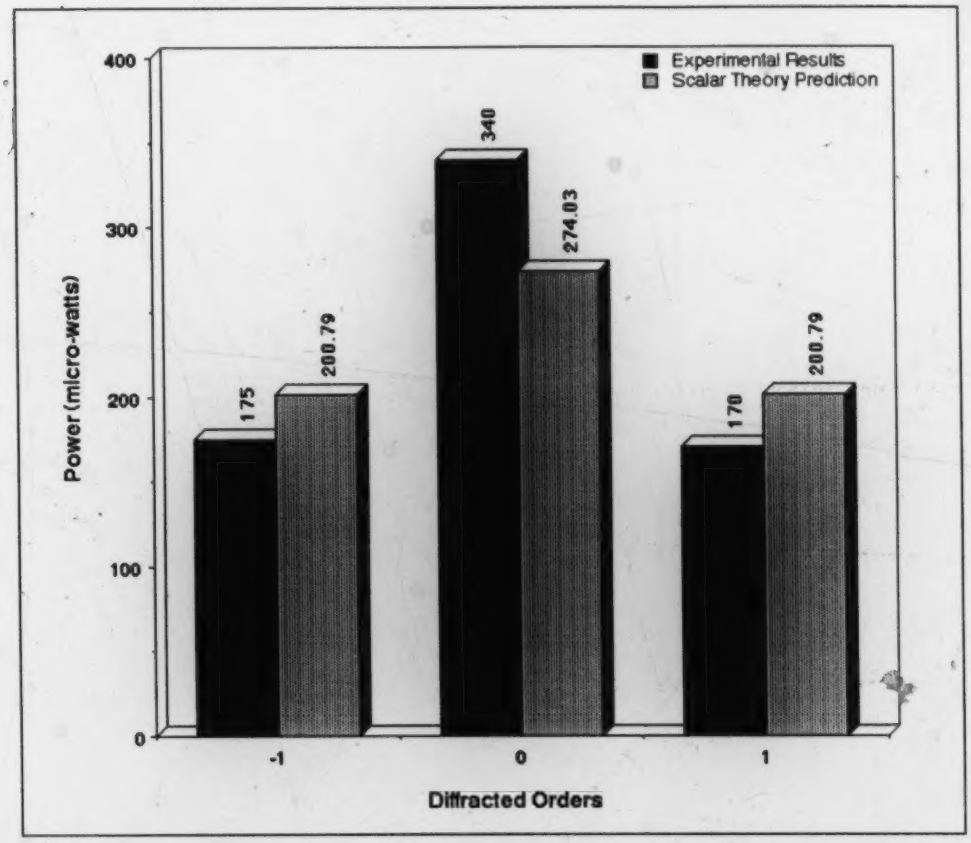

Fig. 3.14 Intensity distribution of the diffracted orders, measured at 675 nm

A simple scalar diffraction theory was used in the grating designs and such an approximation may not yield very accurate results considering the small dimensions of the grating features. A more sophisticated model based on rigorous electromagnetic theory may give us the right design numbers for the V-groove widths and spacing. The nature of the fabrication of the grating may also play a crucial role in determining its performance. The Si_3N_4 diaphragm is under a compressive stress and this may affect the optical properties of the material which may be partially anisotropic. It was also observed that the thickness of lines written by e-beam writing, for some unknown reason, is not very consistent in all areas. This would cause an aberration in the periodic grating structure and thus affect the

performance.

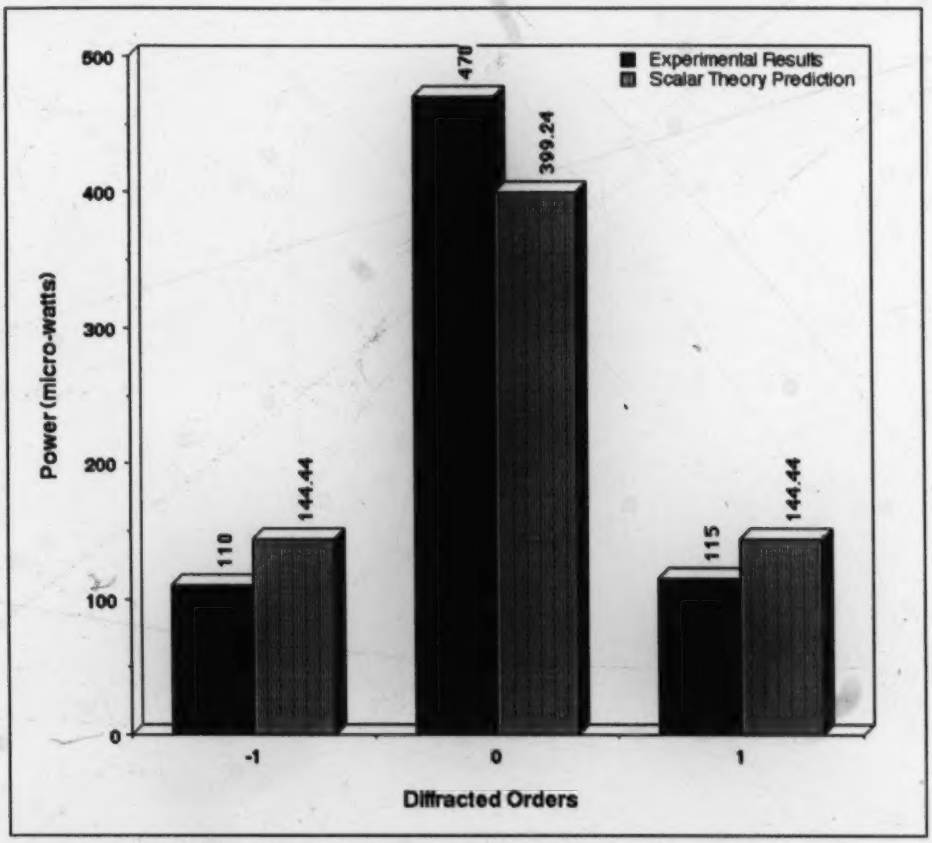

Fig. 3.15 Intensity distribution of the diffracted orders, measured at 1300 nm

Despite the discrepancy between theory and experiment, this work into the novel V-groove grating structures clearly indicates the promise of this technique for realising 1:N beam splitters. To summarize, the main advantages of using this technique are (a), the self-limiting etching process which allows the groove depth to be dependent upon only the groove width which in turn is defined by lithography and (b) the ability to obtain smooth grating profiles which are otherwise impossible to realize in gratings that utilize RIE etching.

Chapter-4

Free Space Optical Distribution for Optoelectronic Switching

The concept of optoelectronic switching was introduced in chapter 1. In this chapter, the work done in free-space signal distribution for an optoelectronic cross-point switch is described. Free-space optical distribution has the advantage of higher density of interconnections and reduced cost when compared to the guided wave approach. However, it is a known fact that when compared to the guided wave approach, free-space interconnects suffer from cross-talk due to unwanted light coupled from adjacent channels. The reason for the spurious coupling may be due to scattering or free space diffraction of the light beams. But careful design can significantly reduce optical-crosstalk to a level where it is no longer the principal bottle-neck in the performance of the overall system. Two novel low cross-talk techniques for free space optical distribution have been conceived and implemented in this work and are described in the following sections [42]-[44].

4.1 3x3 Optoelectronic Cross-bar Switch

The basic design of the 3x3 free space optoelectronic switch(OES) is shown in Fig. 4.1. The inputs to the switch, labelled 1, 2 and 3, are compact coherent optical sources. The outputs are shown as electrical lines (A, B, C) in a vertical plane. The cross-points of the switch are 9-metal-semiconductor-metal (MSM) photodetectors in a 3x3 rectangular array. The outputs (A, B or C) are the summed electrical currents of the corresponding rows of the detectors. Each input is vertically split three ways to illuminate one photodetector in each row by a focusing and beam-splitting element. Switching is achieved by turning the detectors ON or OFF with bias voltages to the control inputs labelled a1 to c3. If the signal in input '1' is to be switched to the output channel 'B', the crosspoint b1 is biased to the ON-state or if input '3' is to be switched to output channel 'A' the detector a3 is biased to the ON-state.

In this work the detectors used are gallium arsenide (GaAs) MSM photodetectors and each MSM in the 3x3 matrix is positioned on 250 μm centres with respect to each other. This would mean that the inputs (1,2,3) must also be positioned at 250 μm centre to centre spacings between any two adjacent sources.

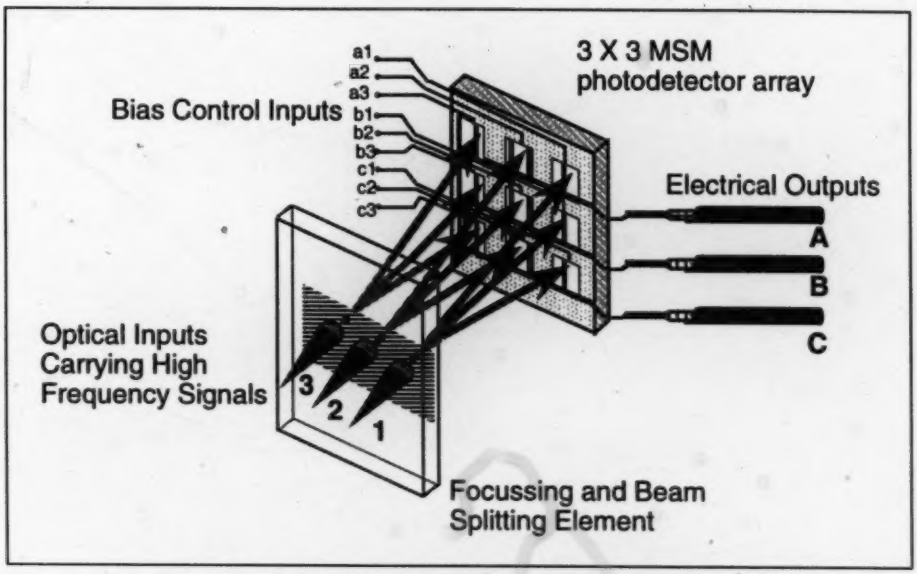

Fig. 4.1 Basic design of the 3x3 optoelectronic switch

The OES can be configured in either an optical-in electrical-out(OIEO) mode or in an electrical-in electrical-out(EIEO) mode. The OIEO configuration is shown in Fig. 4.2(a). Connectorized single mode fibre (SMF) pigtails aligned by silicon V-grooves [45] on 250 μm centres act as the optical sources inside the switch. Optical signals carrying the high frequency payload are connected to these pigtails, and switched to any desired output electrical channels by the OES. In the present work the OIEO configuration was tested using pigtailed 675 nm laser diodes. A realization of the EIEO configuration is shown in Fig. 4.2(b). The high speed signals carried on coaxial lines serve as inputs to laser driver circuitry for an array of vertical cavity surface emitting lasers (VCSEL's) that are the optical sources in the switch. The VCSELs used in this work emitted light at 850 nm wavelength. The theory and design of the optical distribution is described in the following section.

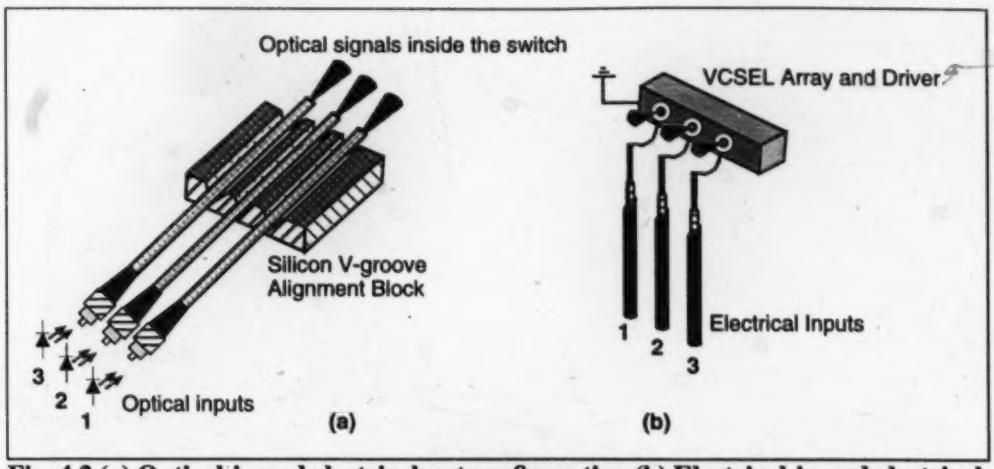

Fig. 4.2 (a) Optical-in and electrical-out configuration (b) Electrical-in and electrical-out configuration

4.1.1 Free Space optical Distribution: Theory and Design

The most important element in Fig. 4.1 is the focusing and beam splitting element. The beam splitting is achieved by a 1:3 Dammann grating of period 20 μm. The grating has been fabricated by techniques described in chapter 2. The etch depths are 0.73 μm for the OIEO case ($\lambda_o = 0.675\ \mu m$) and 0.92 μm for the EIEO case ($\lambda_o = 0.850\ \mu m$). A 0.1μm SiO_2 layer is deposited by CVD on the back side of the grating and ultra violet (UV) light curable polymer microlenses are dispensed on 250 μm centres on the SiO_2 as shown in Fig. 4.3. The oxide layer ensures that the polymer lenses have uniform shapes and good adhesion. The microlenses are deposited by a patented computer controlled pressure dispensing technique developed at TRLabs [46],[47]. The fabrication process is very robust, well suited for mass production and gives excellent repeatability of the microlenses. A SEM photo of the polymer micro lenses is shown in Fig. 4.4.

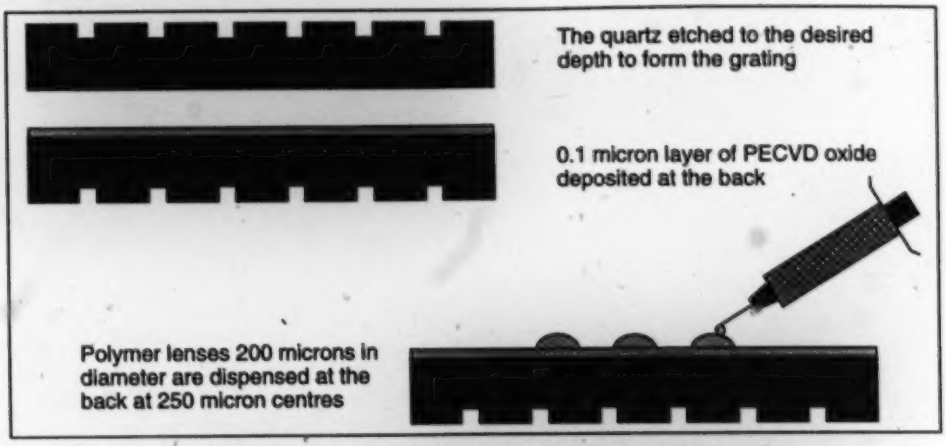
The quartz etched to the desired depth to form the grating
0.1 micron layer of PECVD oxide deposited at the back
Polymer lenses 200 microns in diameter are dispensed at the back at 250 micron centres

Fig. 4.3 Fabrication of the focusing and beam splitting element

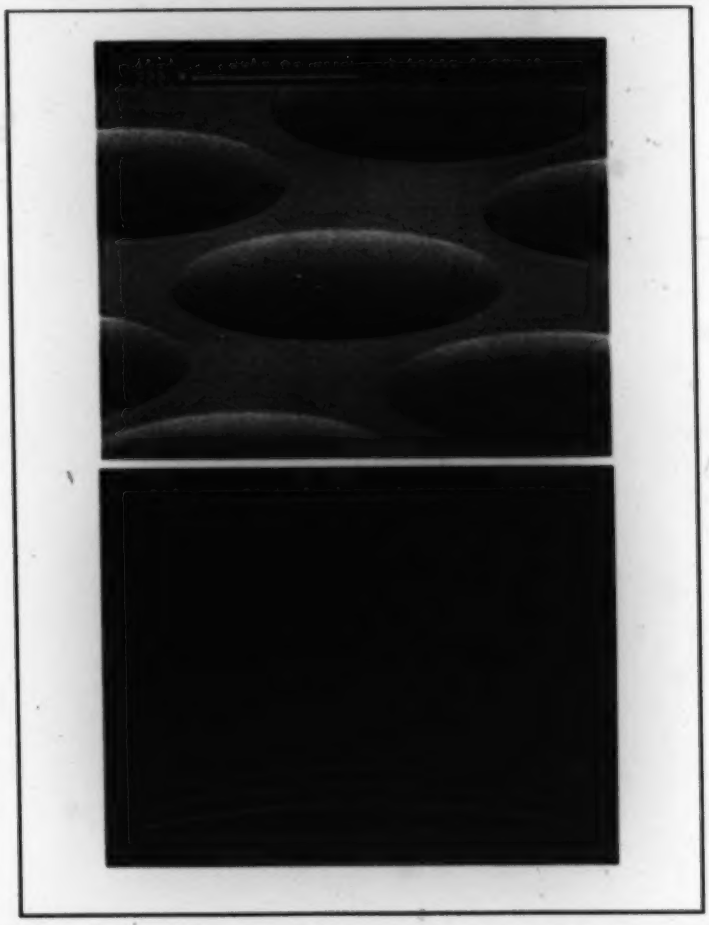

Fig. 4.4 SEM photographs of the polymer microlenses, top view and side view

A simplified schematic of the optical distribution of one input is shown in Fig. 4.5. The Dammann grating has a period of 20 μm, and the angle of divergence between the 0 and ± 1 diffraction orders is given by

$$\Phi = Sin^{-1}\left(\frac{\lambda_o}{\Lambda}\right) \qquad 4.1$$

where Λ is the grating period. At the detector plane we require that the separation d between the 0 and ± 1 diffraction orders be 250 μm. The image distance v' that would give this separation at the detector plane can be calculated from

$$\tan\Phi = \frac{d}{v'} = \frac{d}{\frac{t}{n} + v} \qquad 4.2$$

Where t and n are the thickness of the grating substrate and refractive index respectively.

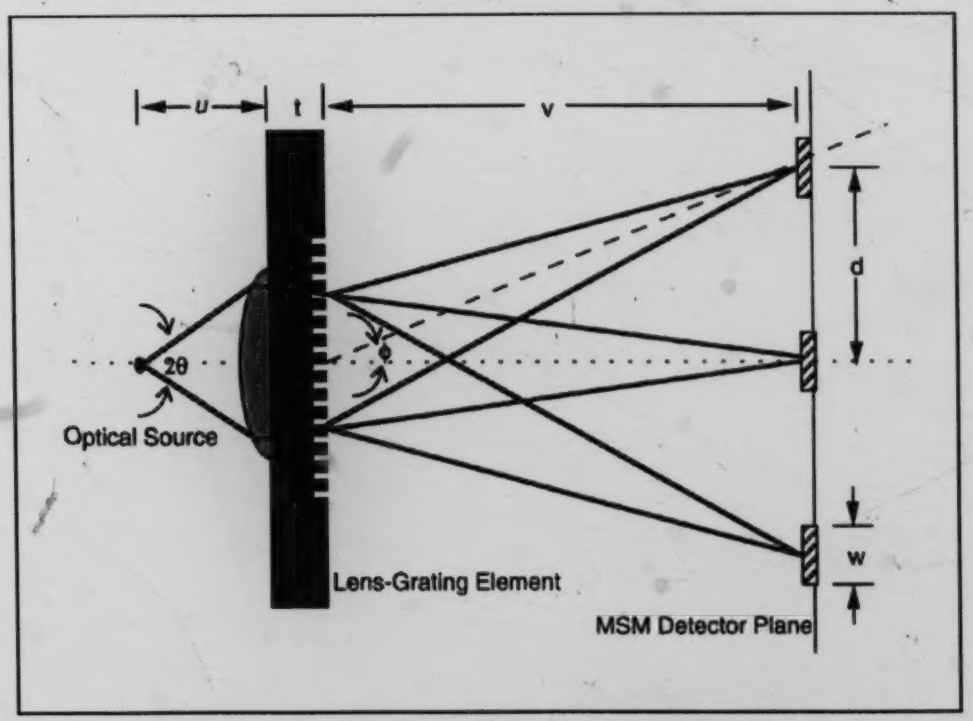

Fig. 4.5 Simplified ray diagram of the optical distribution

In this work t = 1 mm and n =1.46 for quartz, and from Eq.4.1 and Eq.4.2 the image distance v is calculated to be 7.4 mm for the OIEO (λ_o = 675 nm) case and 5.8 mm for the EIEO case (λ_o = 850 nm) case. The function of the microlens is to collect the diverging beam from the source and focus it onto the MSM photodetectors in the image plane. A gaussian beam optics theory for the design and evaluation of the single lens imaging system used is described in the following section.

4.1.2 Beam Optics Theory for Single Lens Imaging

Consider the case of a single lens through which a gaussian beam of waist radius Wo and wavelength λ_o travels as shown in Fig. 4.6. If the location of the waist is taken as the reference point for the beam (i.e. z=0), the complex amplitude of this beam travelling along the Z-axis is given by [48],

$$U(\bar{r}) = \frac{A_o W_o}{W(z)} \exp\left(\frac{-\rho^2}{W^2(z)}\right) \exp\left(-jkz - jk\frac{\rho^2}{2R(z)} + j\zeta(z)\right) \qquad 4.3$$

where W(z) is the width of the wave front at any point z on the axis and

$$W(z) = W_o\left(1 + \left(\frac{z}{z_o}\right)^2\right)^{1/2} \qquad 4.4$$

R(z) is the radius of curvature of the beam and is given by,

$$R(z) = z\left(1 + \left(\frac{z_o}{z}\right)^2\right). \qquad 4.5$$

$\zeta(z)$ is the excess phase factor given by

$$\zeta(z) = \tan^{-1}\left(\frac{z}{z_o}\right). \qquad 4.6$$

Wo is the beam waist or W(z=0) and is related to z_o or the Rayleigh range by

$$W_o = \left(\frac{\lambda z_o}{\pi}\right)^{1/2}. \qquad 4.7$$

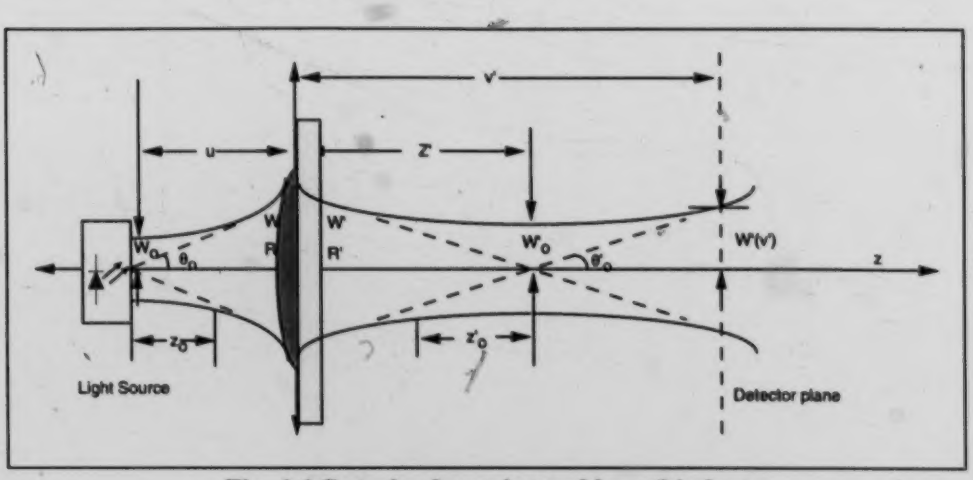

Fig. 4.6 Gaussian beam imaged by a thin lens

The goal is to find for a given lens type the optimum object distance u_{opt} so that the spot size 2W'(v') at the detector plane is minimum.

A lens is characterised by its F-number which is the ratio of its focal length f to the diameter D,

$$F = \frac{f}{D} \qquad 4.8$$

For a given lens diameter, the lower the F, the shorter would be its focal length. Now consider a light source of beam divergence θ_o at the object plane. This beam would be focused in the detector plane if u > f. Also if the lens is to capture at least 86% of the diverging beam from a source placed at the focal plane, the maximum allowable F that the lens can take can be calculated from (see Fig. 4.6)

$$\tan\theta_o = \frac{D}{2f} = \frac{1}{2F} \qquad 4.9$$

$$F_{max} = \frac{1}{2\tan\theta_o} \qquad 4.10$$

If the F of the lens used is higher than that given by Eq. 4.10, portions of the diverging

beam will escape the lens. It follows for a given F lens, the object distance u can have a value any where between

$$FD \leq u \leq F_{max} D \qquad 4.11$$

For the OIEO case $\theta_o = 6.8^o$, $F_{max} = 4.17$ and for the EIEO case $\theta_o = 9.8^o$, $F_{max} = 2.89$.

In this work a polymer microlens of F2.72 and diameter of $210\mu m$ is employed, and is adequate for both OIEO and EIEO cases.

In order to find the optimized u_{opt} which results in the smallest spot size $2W'(v')_{min}$ at the detector plane, it is necessary to first find z' and W_o' of the beam transmitted through the convex lens. Once the location of the waist z' and the waist radius Wo' in the image side of the lens is known, the transmitted gaussian beam is completely characterized and the beam parameters at any distance from the lens can be computed using the relations in Eq. 4.4 to 4.7. Now, Eq 4.5 can be rearranged as

$$z^2 - zR + z_o^2 = 0 \qquad 4.12$$

Also from equations 4.4 and 4.7 we have

$$z^2 - z_o \frac{W^2 \pi}{\lambda} + z_o^2 = 0 \qquad 4.13$$

From Eq. 4.12 and Eq. 4.13 we obtain

$$z_o = \frac{\lambda R z}{W^2 \pi} \qquad 4.14$$

Substituting Eq. 4.14 in Eq. 4.13 we have for z

$$z = \frac{R}{\left[1 + \left(\frac{\lambda R}{\pi W^2}\right)^2\right]} \qquad 4.15$$

And from Eqs. 4.7, 4.14 and 4.15 we can obtain for the beam waist

$$W_o = \frac{W}{\sqrt{1+\left(\frac{\pi W^2}{\lambda R}\right)^2}} \qquad 4.16$$

Equations 4.15 and 4.16 give the location of the waist and the waist radius if the width of the beam and the radius of curvature is known at any point away from the waist. When a beam travels through a lens of focal length f and transmittance given by $\exp\left(jk\rho^2/(2f)\right)$, the complex amplitude of the beam is multiplied by this phase factor [48]. The phase of the beam arriving at the plane of the lens is given by

$$kz + \frac{k\rho^2}{2R} - \zeta \qquad 4.17$$

The phase of the transmitted wave is altered to

$$kz + \frac{k\rho^2}{2R} - \zeta - \frac{k\rho^2}{2f} = kz + \frac{k\rho^2}{2R'} - \zeta \qquad 4.18$$

where

$$\frac{1}{R'} = \frac{1}{R} - \frac{1}{f} \qquad 4.19$$

The radius of curvature R' of the beam at the lens plane after transmission through a lens of focal length f can be computed from Eq. 4.19. The width of the beam W' after transmission through the lens is approximately the same as that arriving at the lens plane for a thin lens, therefore for a thin lens we can state

$$W(z=u) \cong W' \qquad 4.20$$

From Eqs. 4.19 and 4.20 we obtain the radius of curvature and beam width of the transmitted wave and using this data in Eqs. 4.15 and 4.16, the location of the waist Z' and the waist radius W_o' of the beam in the image side of the lens is computed. The spot size of the beam at the detector plane is then calculated using Eq. 4.4

$$2W'(v') = 2W'_o\left(1+\left(\frac{v'-z'}{z_o'}\right)^2\right)^{1/2} \qquad 4.21$$

where

$$z_o' = \frac{W_o'^2 \pi}{\lambda} \qquad 4.22$$

Based on the above theoretical analysis, a C program was written to evaluate the spot size 2W'(v') for different values of the source distance, u. The results are plotted in Fig. 4.7 for both EIEO and OIEO cases.

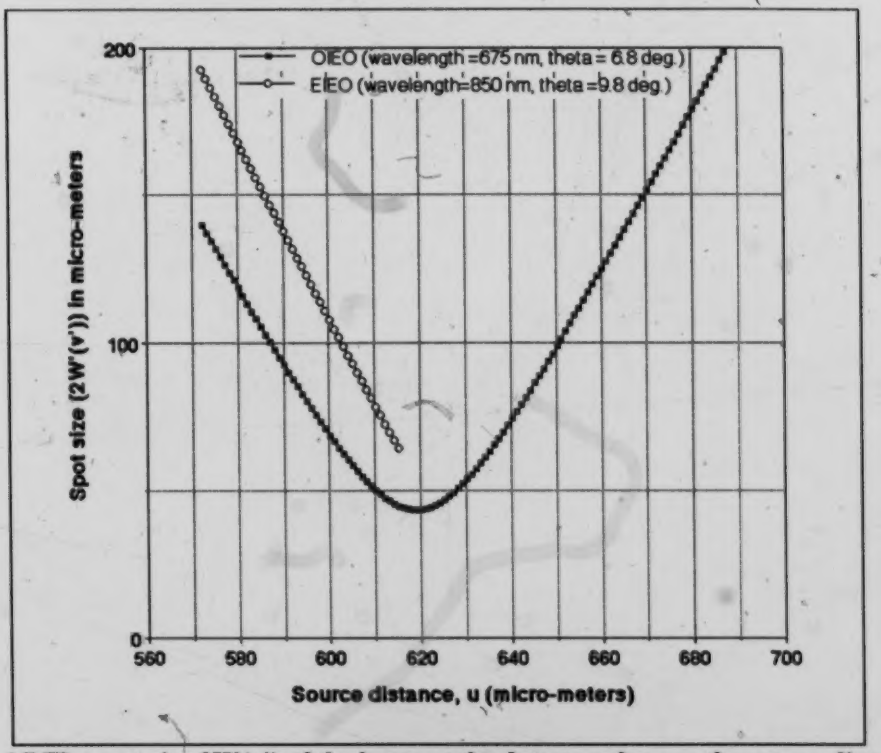

Fig. 4.7 The spot size 2W(v') of the beam at the detector plane vs the source distance u away from the lens

The spot size (2W'(v')) for the EIEO case is not computed for source distances (u) greater than $615\mu m$, because u exceeds $F_{max}D$ and portions of the diverging beam from the source would escape the lens. The MSM detectors are $100\mu m$ x $100\mu m$ in size and in both cases the minimum theoretical spot size achievable is smaller than the detector area. A camera image of the optical distribution is shown in Fig. 4.8. The dotted lines represent

the outline of the MSM photodetectors and it can be seen that the spot size is well contained within the detector area.

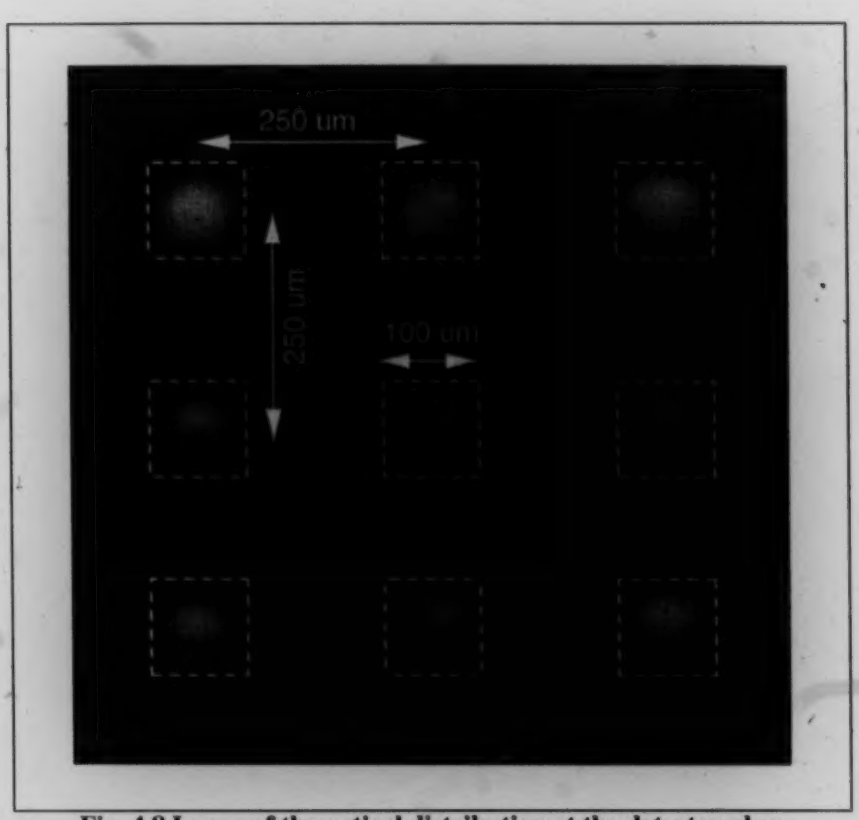

Fig. 4.8 Image of the optical distribution at the detector plane

The imaged spots are slightly bigger than those predicted by theory because of many factors such as lens aberration, non-strictly gaussian nature of the beam, and inaccurate data regarding the beam divergence of the source amongst others.

4.1.3 Experimental Results

In order to evaluate the performance of the optical distribution, DC cross-talk measurements and ON-OFF contrast measurements are carried out. The cross-talk caused by the optical distribution system is measured by illuminating one column of the detectors, (the lasers operating at constant power without any modulation) and measuring the

detected DC photocurrent in the MSMs of the neighbouring columns. The average cross-talk for the OIEO case is found to be -38.1 dB electrical and for the EIEO it is -38.3 dB electrical. A probable source of cross-talk is scattered light caused by the multiple reflections between the detector and grating plate.

The other important performance criteria for an optoelectronic switch is the ON-OFF contrast. This was measured by comparing the current in the MSM detectors when switched ON with that in the MSM's with both ends grounded. The ON-OFF contrast is found to be 37.7 dB. A better contrast is easily achieved by precision biasing the OFF-state so that the current nearly goes to zero. This has been experimentally verified by biasing one of the detectors to 17.6 mV. the contrast then obtained was 69.5 dB.

The cross-talk due to the optical distribution is only one of the many sources of cross-talk that occur in the optoelectronic switch. The overall cross-talk of the system is calculated by taking into account the cross-talk in the input laser sources (if any), the frequency dependent electrical cross-talk in the signal and bias lines of the detector cross points and finally the cross-talk due to the optical distribution. The layout of the monolithic 3x3 MSM array is shown in Fig. 4.9. It can be seen that the signal and the bias lines which carry the high frequency current are in close proximity, and this would result in significant electromagnetic coupling between the various lines. In order to evaluate the adjacent channel cross-talk of the cross-point array at different frequencies a simulation is performed using the Hewelett Packard Microwave Design System (MDS) software package. The coupling between the metal lines of channel-2 and channel-3 are simulated, and the results plotted in Fig. 4.10. The simulation design file is given in Appendix B1. It can be seen that at frequencies above 100 MHz the adjacent channel cross-talk increases beyond -20 dB. It is therefore imperative that in order to employ the present switch architecture for higher bandwidth, the layout of the signal and bias lines in the detector cross-point array have to be modified, in order to reduce the cross-talk. One approach is to provide ground tracks between the signal lines to obtain a coplanar waveguide type configuration[49]. This approach was tried and simulated in MDS using the design file given in Appendix B2.

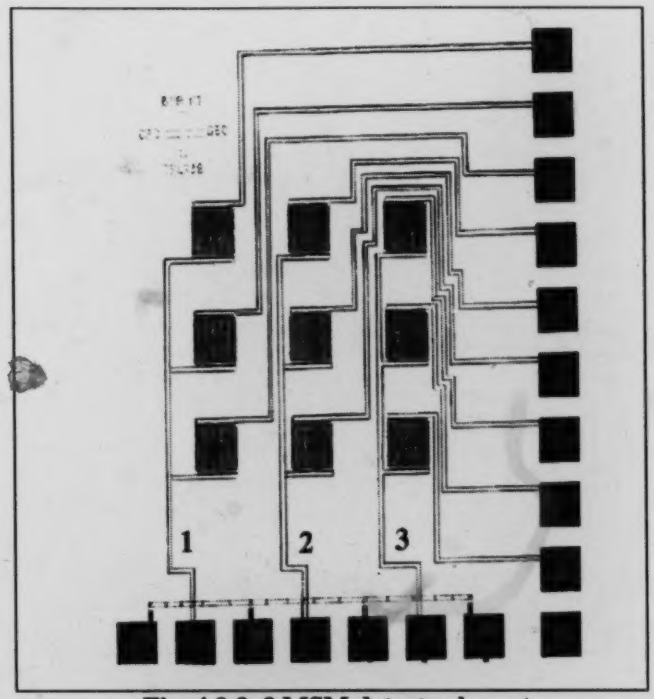

Fig. 4.9 3x3 MSM detector layout

The results of the simulation are shown in Fig. 4.11. It can be seen that the adjacent channel cross-talk is less than -30 dB up to 2 GHz and below -25 dB up to 10 GHz. There is a dramatic improvement in the cross-talk performance over that shown in Fig. 4.10, and the reason for this is because the coplanar waveguide structure provides better field confinement and hence reduces adjacent channel coupling. The details of coplanar waveguide structures will be given in chapter 5.

Another technique to increase the bandwidth of operation is to employ linear arrays of MSM detectors instead of 2-dimensional arrays. The optical distribution is then modified to accommodate the change in the cross-point array configuration. This approach has been studied, and a prototype for a 4x4 free space OES employing linear MSM's and capable of bandwidths in the GHz range is explained in the following sections.

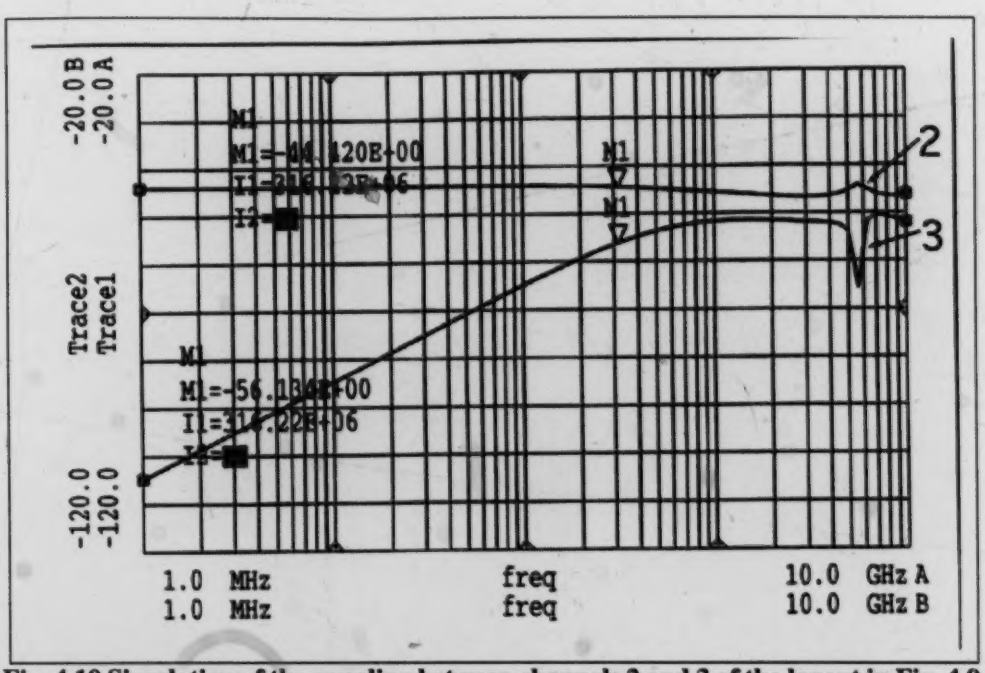

Fig. 4.10 Simulation of the coupling between channels 2 and 3 of the layout in Fig. 4.9 for frequencies between 1 Mhz to 10 GHz.

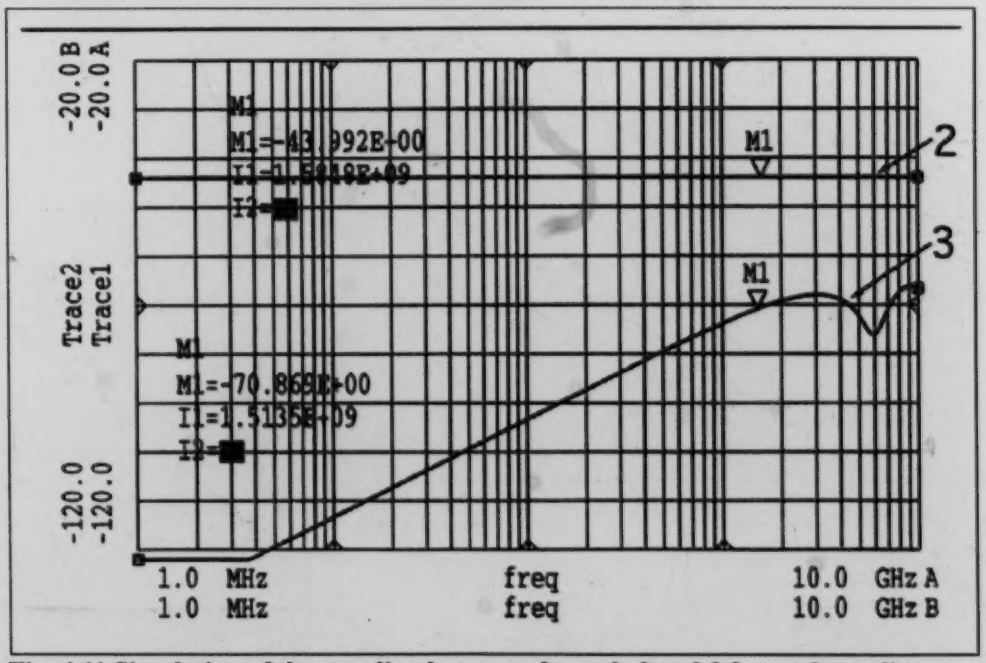

Fig. 4.11 Simulation of the coupling between channels 2 and 3 for coplanar lines

4.2 4x4 Optoelectronic Switch Prototype

The concept for a 4x4 free space broadband OES is shown in Fig. 4.12. The four input light beams are collected and split by a lens-grating element, similar to the one used in the 3x3 OES. The grating used is a 1:2 splitter, and splits the input beams two ways in the vertical plane. The beams are further split two ways by the beam splitter to achieve the 1:4 overall split.

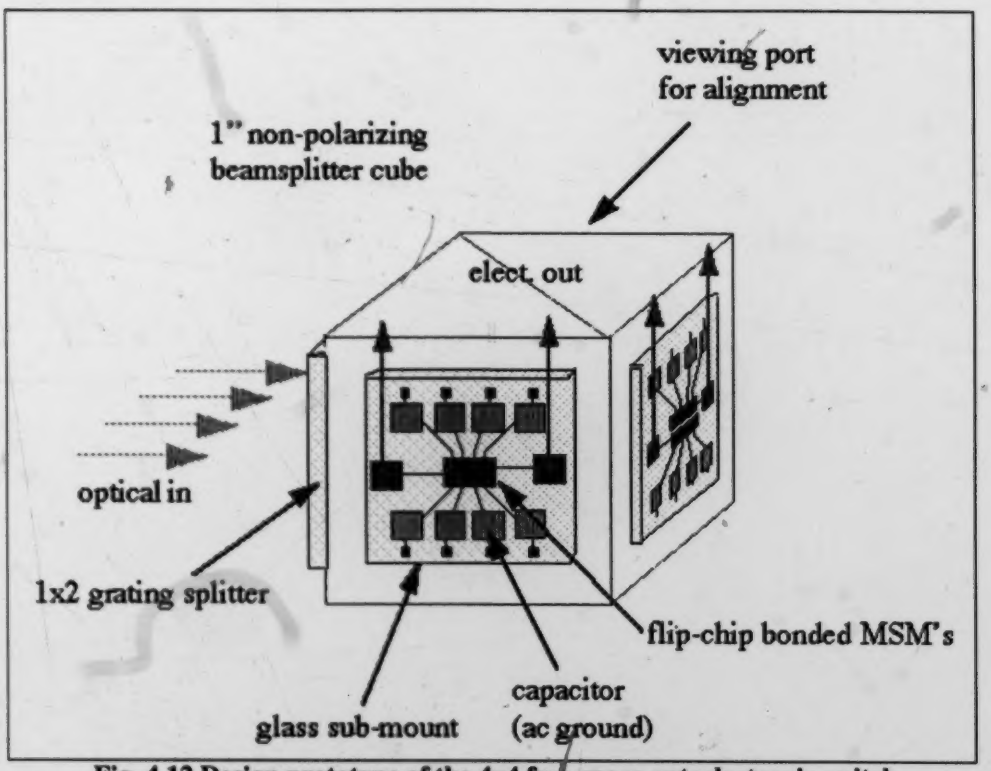

Fig. 4.12 Design prototype of the 4x4 free-space optoelectronic switch

The concept is illustrated in Fig. 4.13 where the trace of one input beam is shown as it passes through the grating and the beam splitter. The light spots on the face of the beam-splitter cube are detected by linear arrays of MSM photodetectors mounted by flip-chip bonding on a separate glass submount. The biasing and RF circuitry are also mounted

on the glass submounts, the details of which are explained in the next chapter. The input beams are separated from each other by 500 μm and could be from a VCSEL array or SMFs aligned at 500 μm centres by a V-groove array. The design for the optical distribution is examined in the following section.

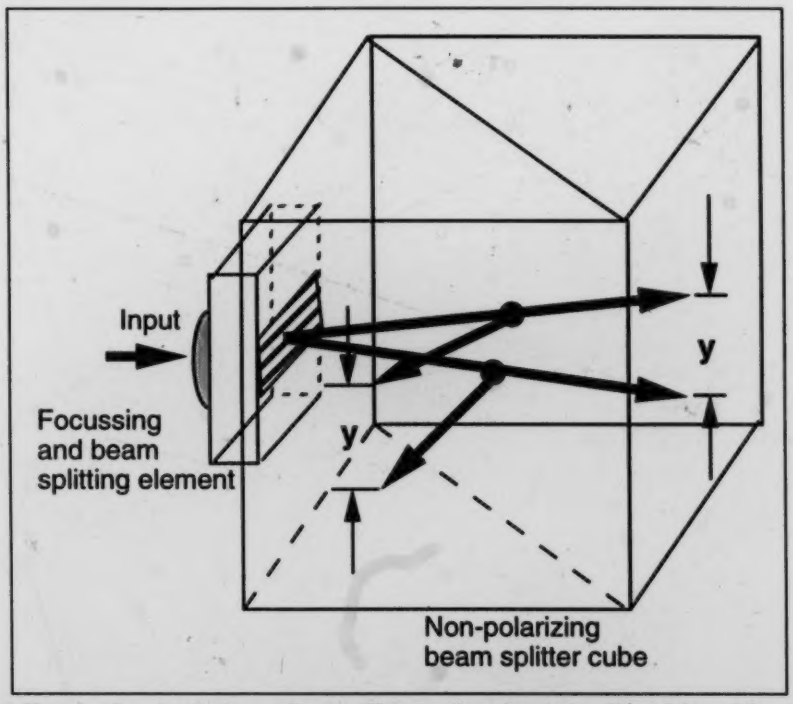

Fig. 4.13 Trace of a single input beam illustrating the 1:4 split achieved by the grating and the beam-splitter

4.2.1 Optical design of the 4x4 OES

The total length of free space region that the beams must travel can be calculated by summing the optical thickness of the grating plate, the beam-splitter cube and the detector submount, i.e.

$$t_{total} = \frac{t}{n} + \frac{t'}{n'} + \frac{t''}{n''} \qquad 4.23$$

where (t, t', t'') and (n, n', n'') are the thicknesses and refractive indices of the respective

elements. The 1:2 grating has a period of 19.230 μm and is fabricated using the technique detailed in chapter 2. The angle in glass of diffraction between the ± 1 and 0^{th} diffraction order for a wavelength of 850 nm, calculated from Eq. 4.1, is $\Phi = 2.53°$. The two linear arrays of MSM detectors, which are flip-chip bonded on the same submount, have to be placed at a separation such that the centre-to-centre distance between the MSMs in the two arrays is given by,

$$y = 2t_{total}\tan\Phi \qquad 4.24$$

where t_{total} is given by Eq.4.23. Now for the grating plate (t = 1 mm, n = 1.46), for the beam splitter cube (t' = 25.4 mm, n" = 1.53) and for the detector submount (t" = 0.71 mm, n" = 1.53). From the above data, the separation of the MSMs in the two linear arrays can be calculated from Eq. 4.23 and Eq. 4.24 as y = 1.588 mm. The lateral separation of the detectors in the same array is fixed by the lateral spacing of the source, and is 500μm in our case.

The MSM detectors used have an active area of 75μm x75μm. It is therefore desired that the spot size of the beam arriving at the detector plane be no more than 75μm. A theoretical analysis for the optimum object distance, u_{opt}, can be performed using the analysis in Section 4.1.2 with small modifications. After the lens, the beam travels through three regions of different refractive index. Since the bulk of the transmission occurs inside the beam splitter cube we can approximate $n = n'' = n' = 1.53$ in order to simplify the computations. The radius of curvature in Eq. 4.19 is now modified to

$$\frac{n'}{R'} = \frac{1}{R} - \frac{1}{f} \qquad 4.25$$

The plot of the spot size for different object distance u, for the F2.72 lens used is shown in Fig. 4.14. It can be seen that the minimum spot size at the detector plane that can be achieved is around $100\mu m$, but if lenses of F-numbers less than F2.72 are employed smaller spot sizes may be achieved.

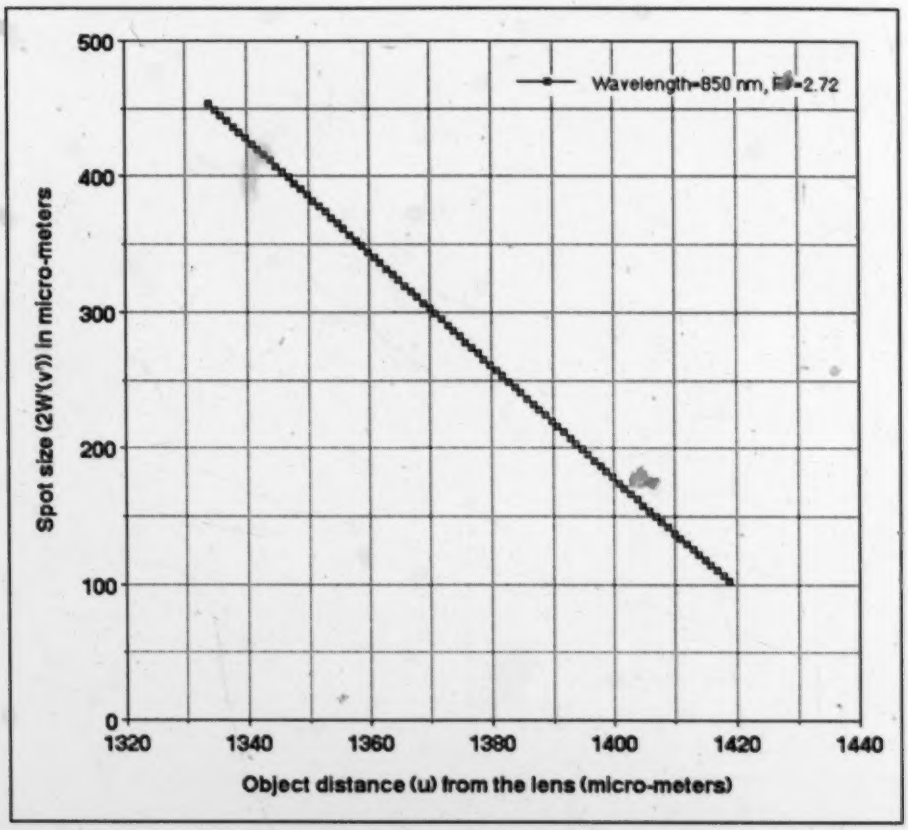

Fig. 4.14 Spot size 2W'(v') at the detector plane vs object distance, u, from the lens

This point is illustrated in Fig. 4.15, where the minimum achievable spot size at the detector plane has been plotted as a function of the F-number of the lens. Note that the optimum object distance (u_{opt}) at which the minimum spot size is obtained is different for each of the different F-number lenses. For F-numbers less than 2.68, the object distance can be adjusted so that the lens captures all the light from the source and focuses it at the detector plane.

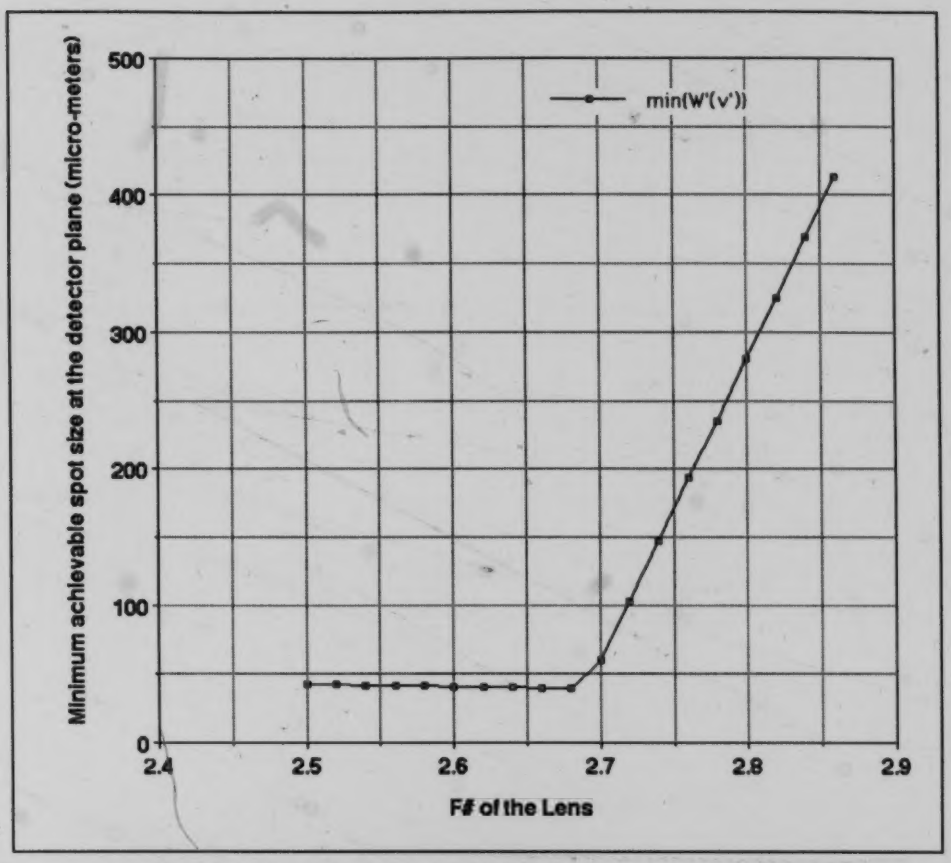

Fig. 4.15 Minimum achievable spot size $\{2W'(v')\}_{min}$ at the detector plane vs F# of the micro-lens

4.2.2 Experimental Results

A camera image of the spots, at an intermediate distance between the grating and the detector plane, is shown in Fig. 4.16 to illustrate the 4x2 optical distribution at a beam splitter face. As the camera's numerical aperture is not large enough to capture the entire optical distribution at the detector plane, only the +1 diffracted orders have been imaged to study the spot size of the beams illuminating the linear array of MSM detectors, and are shown in Fig. 4.17. The spot size is slightly bigger than that predicted by theory and possible reasons for this could be (as mentioned earlier), lens aberration, non gaussian beam or imprecise VCSEL beam divergence data specified by the manufacturer.

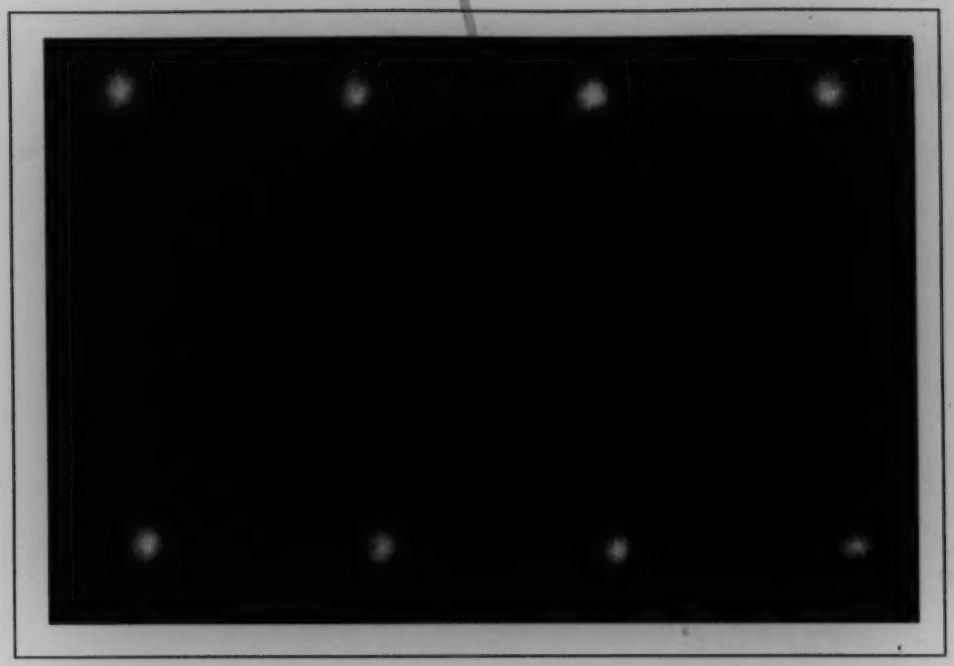

Fig. 4.16 Image of the optical distribution at a distance of 17 mm from the grating

However, the crucial performance factor is the cross-talk in the adjacent channel caused by the optical distribution. This is measured using similar techniques used for the 3x3 OES, and the average cross-talk is found to -44.8 dB.

Fig. 4.17 The +1 diffracted orders imaged at the detector plane

Even though the spot size is bigger than $75\mu m$, there is a 7 dB improvement in isolation over the 3x3 OES case. In the 3x3 OES, the distance between the grating plate and the detector plane is 5.8 mm as compared to 27 mm in the 4x4 OES. If the cross-talk is caused by the multiple reflections between the grating and the detector substrate, it

would be lower for the 4x4 OES because the reflected beams would be more diffused, due to the greater distance between the grating and the detector substrate.

The optical distribution schemes used for the 3x3 OES and 4x4 OES have their own advantages and disadvantages. In the 3x3 OES, a two-dimensional monolithic MSM array must be used. If the array is to be designed for low cross-talk performance, the lay-out becomes complicated. But the advantage gained is that the optical distribution is greatly simplified. On the other hand, in the 4x4 OES, linear arrays of MSMs are used which greatly simplify the detector layout design and the cross-talk at the detector substrate is almost a non-issue. The optical distribution, however, is more complicated than in the 3x3 OES.

Chapter 5

High Frequency Design of the Optoelectronic Switch

An optoelectronic switch embedded in a fibre optic network would function as a cross-connect switch to route signals through different paths. It is therefore necessary that the bandwidth of the OES be greater than, or equal to, the bandwidth of the signals in the fibre channels to be re-routed. Bandwidth limits of an OES are set by the terminal devices that perform the electro-optical and opto-electrical conversions, i.e., the lasers and detectors. The bandwidth of operation of lasers and detectors is determined by the semiconductor device characteristics and the limits imposed due to parasitics in the high frequency packaging of these devices. The following sections discuss in detail the high frequency aspects of the lasers and detectors to be used in the 4x4 OES.

5.1 Transmitter Design

Vertical cavity surface emitting laser arrays (VCSELs) are used for electro-optical conversion at the input stage in the 4x4 OES. VCSELs have optical cavities orthogonal to those of conventional edge-emitting lasers [50]-[54]. The simple change in cavity orientation produces radical differences in the beam characteristics, and allows for more flexible optoelectronic designs. VCSELs typically emit circularly symmetric gaussian beams in contrast to the astigmatic beams of the edge emitters, and therefore require no anamorphic correction.

A microscope image of a semiconductor die (courtesey of VIXEL Corp., Colorado, USA) containing 12 VCSELs at 250μm centre-to-centre separation is shown in Fig. 5.1(a). The VCSELs emitting light under current injection are shown in Fig. 5.1(b).

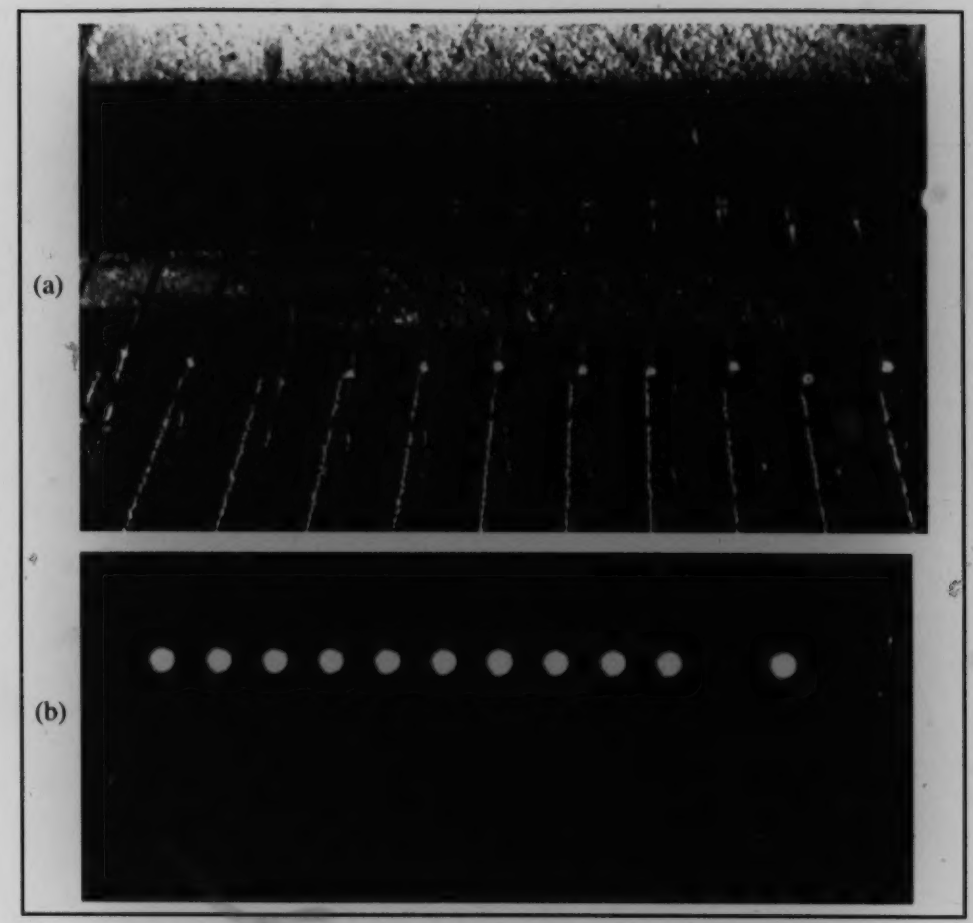

Fig. 5.1 (a) A VCSEL die containing 12 lasers at 250 μm pitch, (b) VCSELs emitting light under current injection

5.1.1 Multichannel High Frequency Modulation: Design Issues

If simultaneous wideband modulation of multiple lasers in the array is desired, a critical issue to be addressed is that of the access lines feeding RF signals to the lasers. The access lines, usually microwave transmission lines of characteristic impedance Z_o, fan in from the electrical peripherals (bias-T's, impedance matching circuitry etc.) on the microwave substrate to the laser array as shown in Fig. 5.2. In order to wire bond to the bond pads on the die, the access lines must fan in to similar lengths of separation as the lasers.

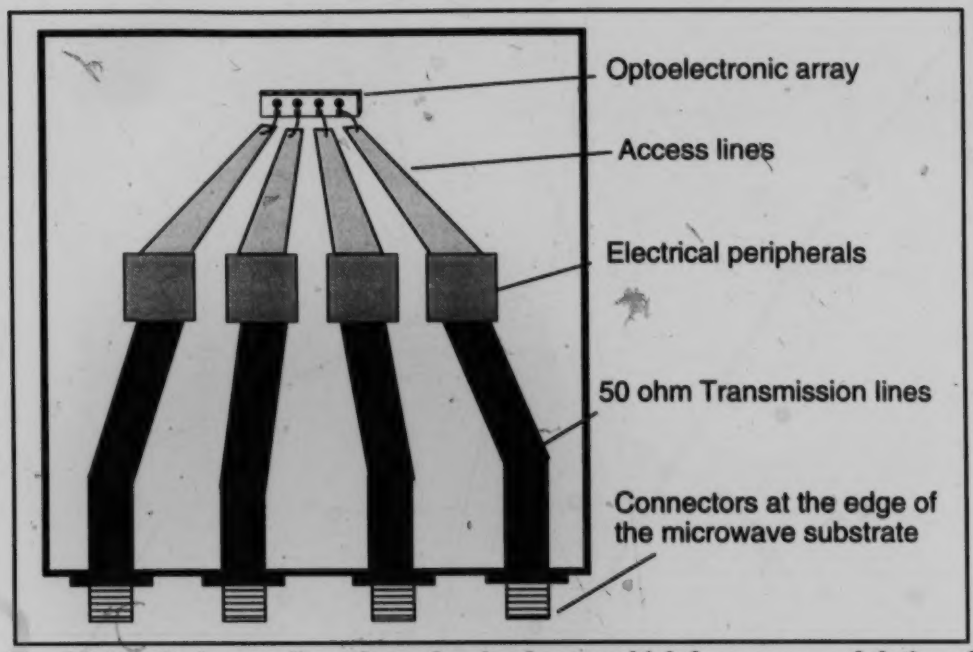

Fig. 5.2 A typical access line scheme for simultaneous high frequency modulation of an optoelectronic array

The access lines commonly used are microstrip transmission lines and have a geometry as shown in Fig. 5.3. The characteristic impedance Z_o of the microstrip line is a function of ε_r the relative permittivity of the substrate material, w the width of the microstrip line and d the thickness of the substrate used [55].

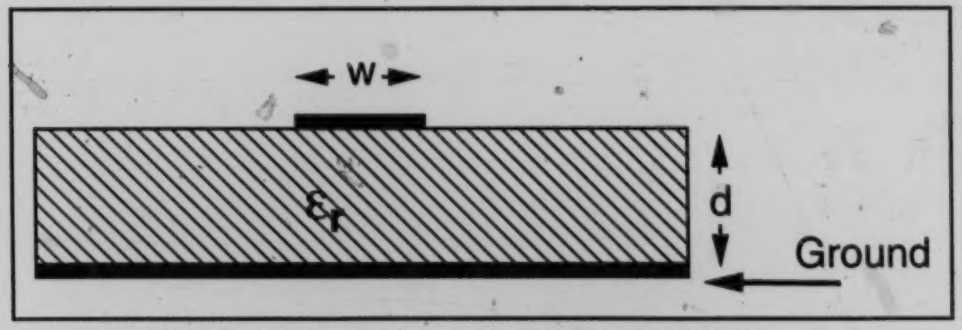

Fig. 5.3 Geometry of a microstrip transmission line

For a given substrate type ε_r and thickness d there is a unique value of w for a specific characteristic impedance. For example, a microwave substrate such as aluminium nitride of thickness d = $625\mu m$ and ε_r = 8.9, would have a w = $675\mu m$ for a Z_o = 50 ohm. If microstrip access lines have to be brought physically close together at a few hundreds of microns separation, it would be necessary to taper the lines. The performance of these lines would be limited to the lower Giga-Hz region because of the impedance mismatch associated with the taper section [56]. An even greater bottle-neck that would limit the frequency of operation of the system is that of the electrical cross-talk among the adjacent channels caused by coupling in the access lines and wire bonds. The cross-talk contribution due to the wire bonds and access lines has been studied by Hayashi et al [57]. It is found that the cross-talk contribution of the access lines is much greater than that of the bonding wires, provided the length of the bond wires are kept at typical values of $500\mu m$ or less, a task quite easily achieved.

A typical access line layout using microstrip lines for devices on $500\mu m$ pitch is shown in Fig. 5.4.

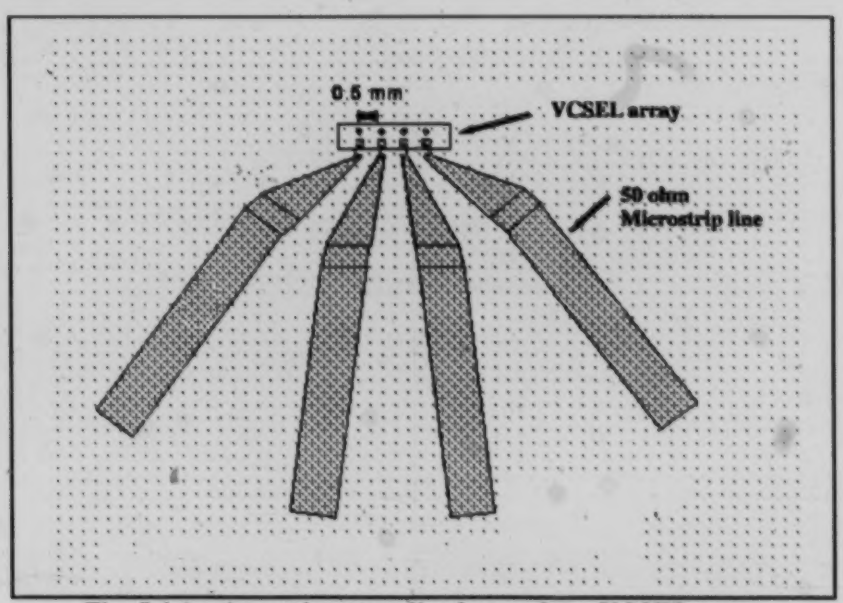

Fig. 5.4 A microstrip access line layout for a VCSEL array

The layout was simulated in MDS to study the cross-talk performance as a function of frequency and the results are plotted in Fig. 5.5. The design file for the simulations is given in Appendix B3. It can be seen that the cross-talk isolation degrades below 20 dB for frequencies above 5 GHz.

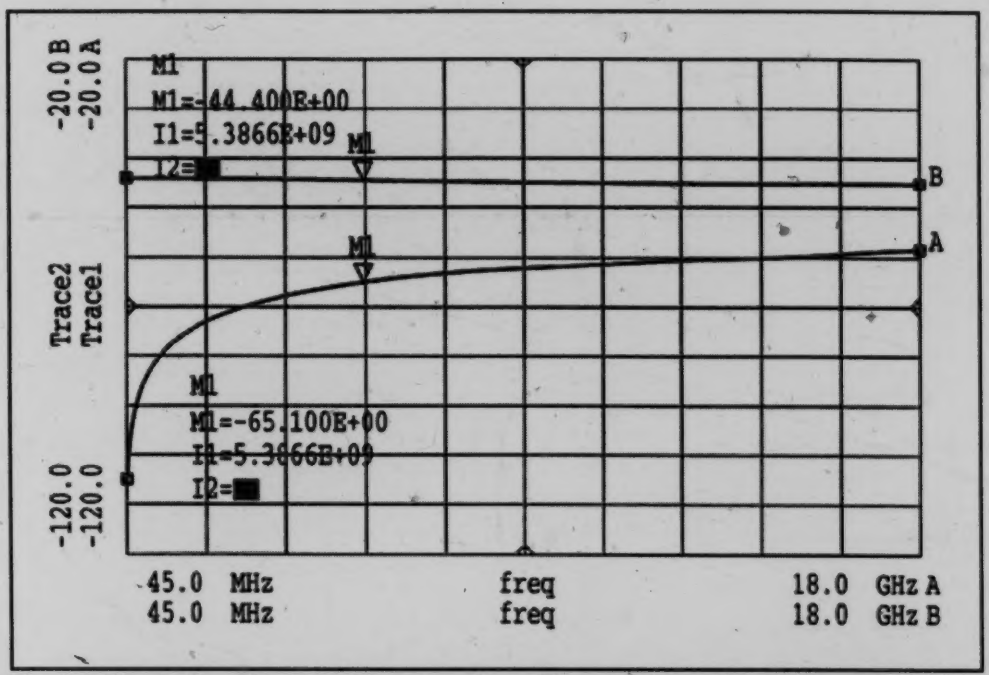

Fig. 5.5 Simulation of microstrip access lines. Trace-B shows the response of a single channel, and Trace-A is the cross-talk in the adjacent channel due to coupling

One of the ways of reducing the cross-talk in the access lines is to increase the channel pitch. However, this would result in waste of active devices and make the modules larger. Another technique is to shorten the distance between the electrical peripherals and the laser array. This would require tight bends in the lines for side channels, which degrade transmission characteristics [58]. To overcome these problems, the use of thin substrates which would require thinner microstrip widths (w) has been extensively investigated by Hayashi et al [57]. However, the frequency response of such techniques is limited to 2 GHz because of material dispersion and high attenuation. To surmount these problems, we have come up with a novel access line scheme with low adjacent channel cross-talk using coplanar waveguide (CPW) techniques.

5.1.2 Coplanar Waveguide Access Lines

The geometry of a coplanar waveguide is shown in Fig. 5.6. It consists of a central "hot" conductor of width 'w', separated by slot 's' from two adjacent ground planes. The characteristic impedance (Z_o) of a CPW is a function of $\varepsilon_r(f)$, w, s and d.

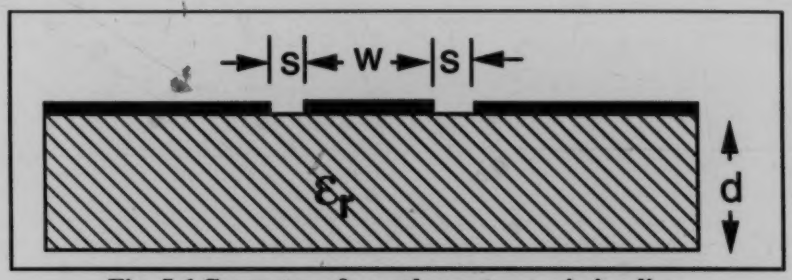

Fig. 5.6 Geometry of a coplanar transmission line

The exact analytical expression for Zo, derived from quasi-static approximations is quite involved and is studied extensively in [59]-[62]. One of the greatest flexibilities provided by the coplanar waveguide is the ability to design transmission lines of almost any desired dimensions by varying the width (w) and slot (s) for a fixed substrate thickness (d) and permittivity ε_r. This allows the design of tapers without causing any impedance changes in the line, a feature not possible with microstrip lines. Employing CPWs, it is possible to design access lines of any Zo, and also small dimensions, to enable easy fan-in to the laser array for wire bonding. By use of properly designed tapers, the access lines are tapered out to larger dimensions to allow easy soldering of the peripheral components such as resistors, capacitors, etc. But the greatest advantage of using CPW access lines is the low adjacent channel crosstalk, even when the lines are brought in to a few hundreds of microns separation from each other. Fig. 5.7 shows four transmission lines of Z_o =50 ohms that taper and fan-in to $500\mu m$ separation. The width of the "hot track" (w) is 1 mm at the edge and $100\mu m$ in the access lines. The slot (s) between the "hot track" and the ground is $290\mu m$ at the edge and $45\mu m$ in the access lines. The above dimensions were computed using the MDS line calculator, for a substrate thickness (d) of $625\mu m$ and permit-

tivity (ε_r) of 8.9.

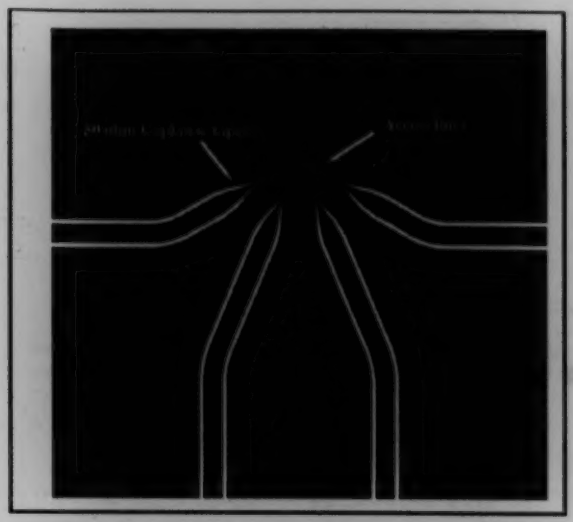

Fig. 5.7 Coplanar access line layout for a VCSEL array

The layout was also simulated to study the adjacent channel coupling and the simulation design file is given in Appendix B4. The results of the simulation for the frequency range between 45 MHz and 18 GHz are shown in Fig. 5.8.

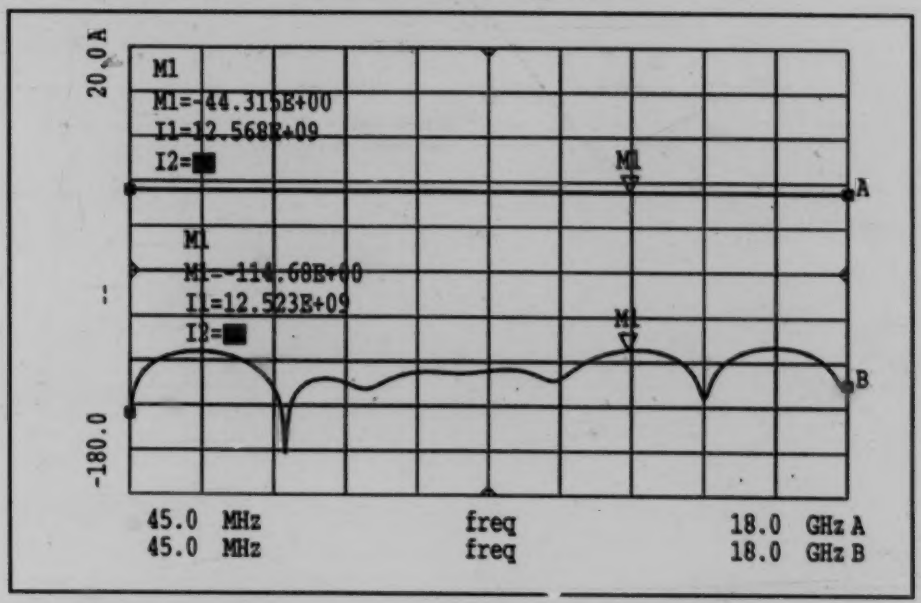

Fig. 5.8 Simulation of coplanar access lines. Trace-A is the response of a single channel, and Trace-B is the cross-talk in the adjacent channel

There are more than 70 dB of cross-talk isolation between the adjacent channels up to 18 GHz. This is, no doubt, a significant improvement over the microstrip access lines. In order to experimentally verify the performance of CPW access lines, the pattern in Fig. 5.7 was fabricated.

5.1.3 Fabrication of Coplanar Access Lines

The smallest feature size in the layout of Fig. 5.7 is $45\mu m$ and occurs as the slot width (s) in the access lines. Such small features cannot be fabricated using conventional printed circuit board (PCB) manufacturing techniques as their resolution is limited. It is therefore essential to use semiconductor lithographic processes, where the pattern is transferred from a mask to a photoresist layer spun on the metallised substrate. The fabrication process is shown in Fig. 5.9.

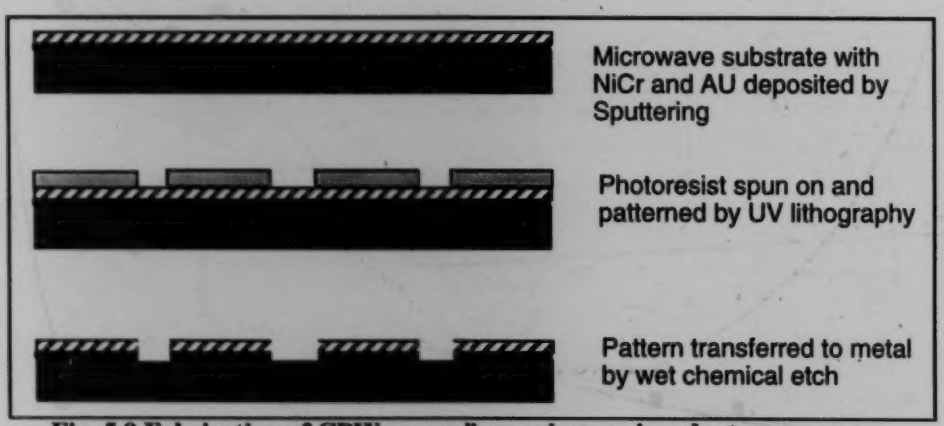
Microwave substrate with NiCr and AU deposited by Sputtering
Photoresist spun on and patterned by UV lithography
Pattern transferred to metal by wet chemical etch

Fig. 5.9 Fabrication of CPW access lines using semiconductor processes

Aluminium nitride (AlN), with d = $625\mu m$ and ε_r = 8.9, has been chosen as the microwave substrate. The reasons for its selection is explained later. In the first step a thin layer of nickel-chromium (NiCr) of thickness less than $0.1\mu m$ is sputtered on to the substrate and then a thin film of gold (Au) approximately $3.5\mu m$ thick is sputtered on top. The NiCr, unlike Au, adheres well to the AlN and serves as an intermediate adhesion layer. The pattern after being transferred to the photoresist layer is transferred to the metal layers by wet chemical etching. The thickness of the Au layer to be deposited is determined by

the skin depth δ_{skin}, of the microwave signal given by[63]

$$\delta_{skin} = \sqrt{\frac{1}{\pi\mu\sigma f}}, \qquad 5.1$$

and is the distance into the conductor where the fields and currents have decayed to e^{-1} of their surface values. At high frequencies current density is concentrated at a thin layer on the surface, for example δ_{skin} for Au at 10 GHz is $0.786\mu m$. As a rule-of-thumb, it is desired that the thickness of Au deposited be at least three times δ_{skin}, so that a uniform current distribution assumption can be assumed within the conductor for estimating the conductor losses[64]. In the present fabrication, the thickness of Au deposited is $3.5\mu m$ and is adequate for our applications.

5.1.4 Experimental Setup and Results

The signals are picked up using a Pico-probe Inc. dual microwave probe as shown in the camera image of Fig. 5.10.

Fig. 5.10 Camera image of the substrate showing the dual pick-up microwave probes

The microwave signals are launched through SMA connectors and microwave probes. The dual probes have a centre-to-centre separation of 500 um and are rated to have a cross-talk lower than -35 db at 40 Ghz [65]. In the first step the S_{21} of Channel 1 is measured using the HP vector analyser and Channel 2 is terminated in 50 ohm broad band loads at both ends as indicated in Fig. 5.11.

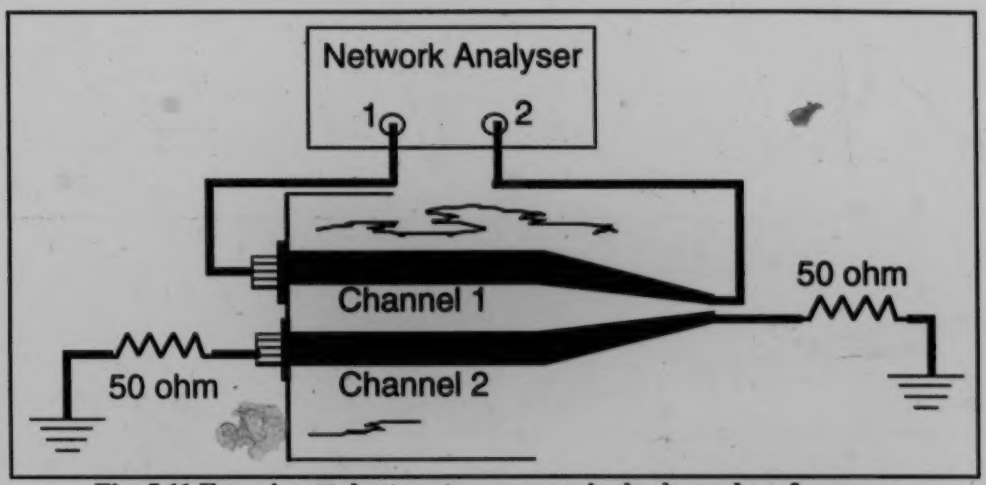

Fig. 5.11 Experimental set-up to measure single channel performance

The S_{21} and the S_{11} are plotted in Fig. 5.12(a) for a frequency range between 45 MHz and 7 Ghz. The S_{11} is less than -10 dB almost over the entire frequency range. This indicates that the coplanar tapers fabricated have a low associated impedance mismatch[66]. The phase response is shown in Fig. 5.12(b). To measure the cross talk, the signal is launched in channel-1, which is terminated in 50 ohm load and the coupled signal is picked up from the channel-2 probe as shown in Fig. 5.13. The S_{21} plots for the forward transmission in channel-1 and the crosstalk in channel-2 for the frequency range between 45 MHz and 18 GHz are shown in Fig. 5.14. The adjacent channel cross-talk is well below -45 dB up to 3.6 Ghz and well below -30 dB up to 8 Ghz. Between 8 and 18 Ghz the average crosstalk is below -25 dB. The above results are the lowest figures for access line cross-talk reported by any research group so far. There is, however, a significant difference in the cross-talk figures between the simulation plot of Fig. 5.8 and the experimental results of Fig. 5.14.

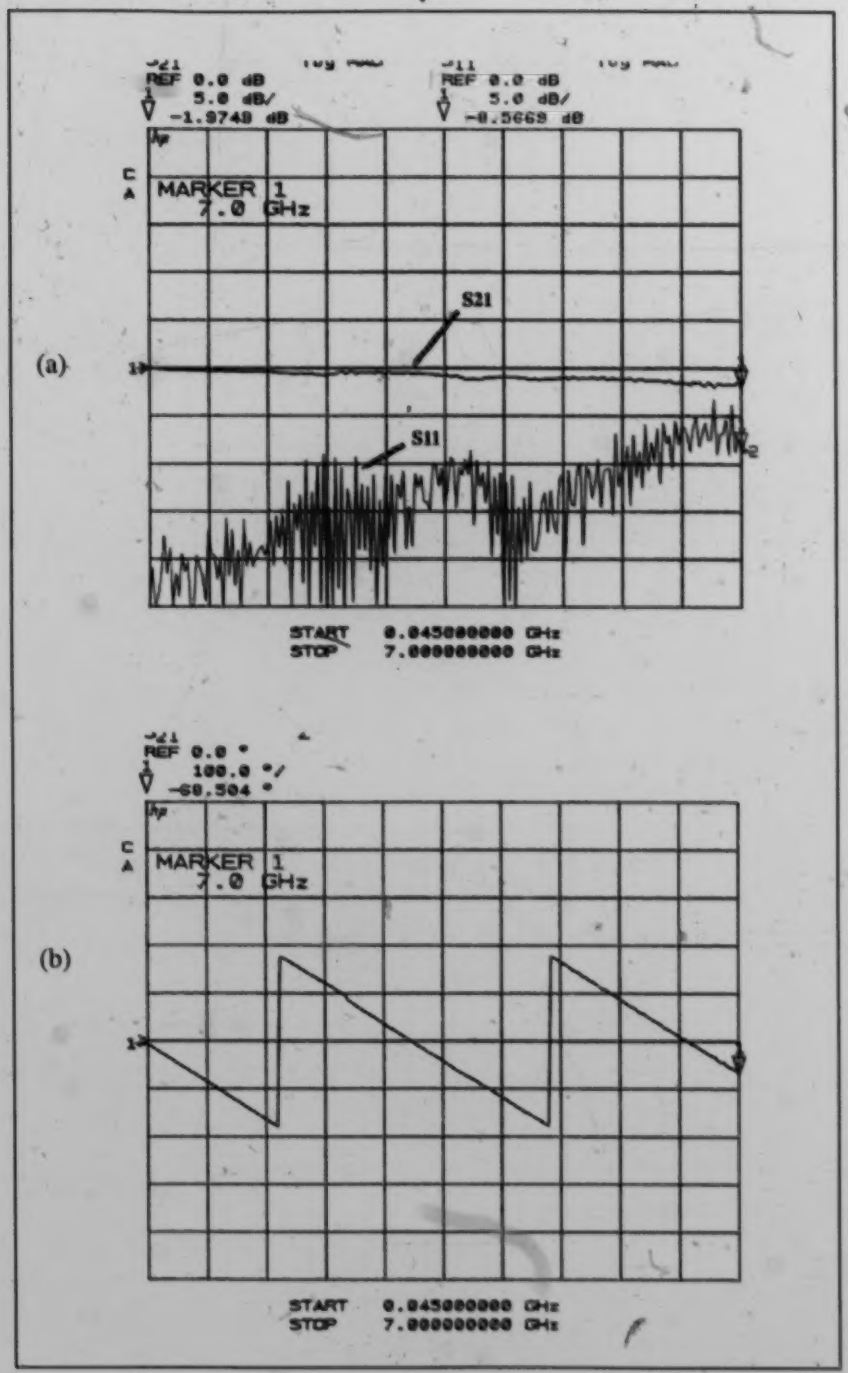

Fig. 5.12 (a) S_{21} and S_{11} of a single channel (b) the phase response

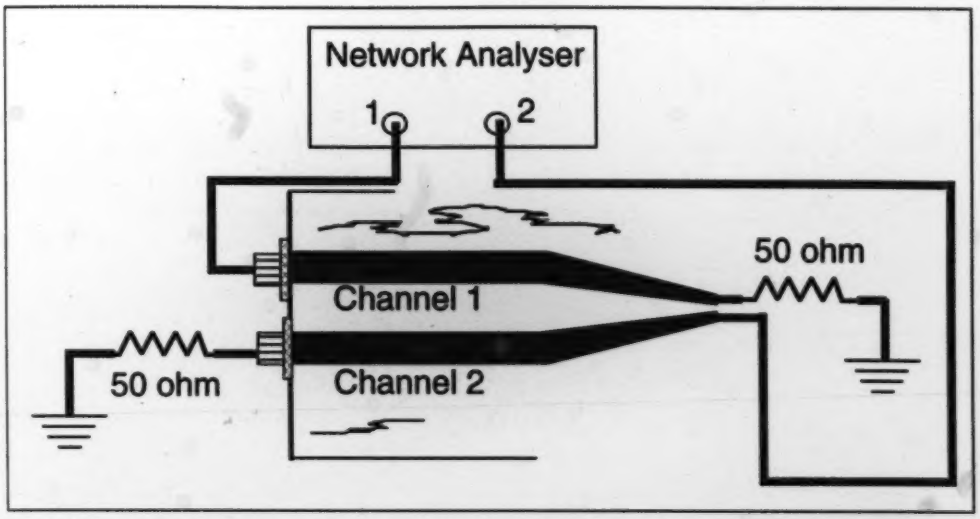

Fig. 5.13 Experimental set-up for adjacent channel cross-talk measurement

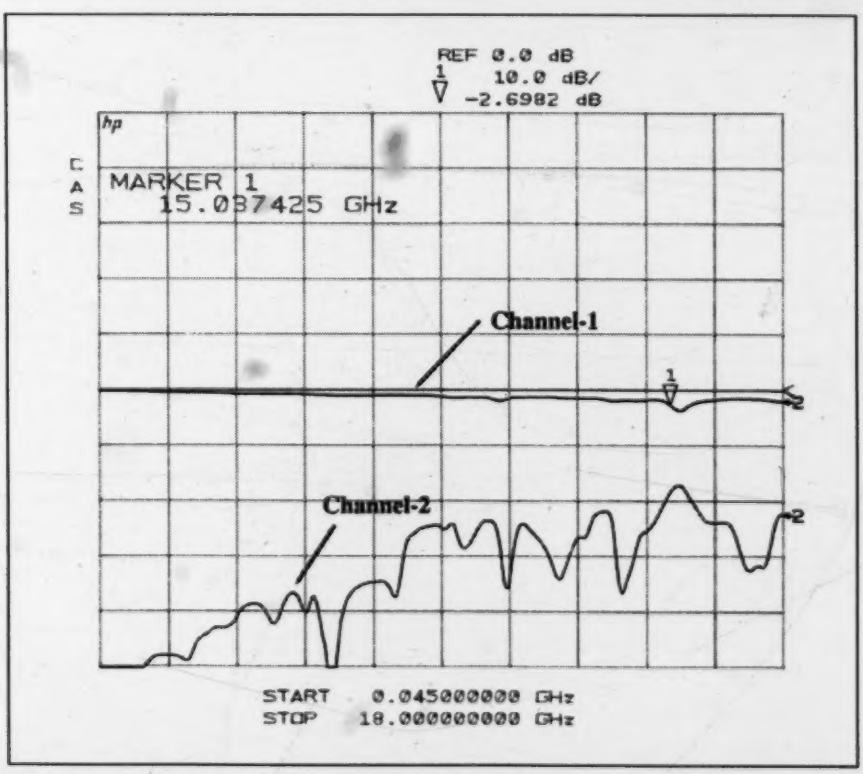

Fig. 5.14 Plot showing the S_{21} of channel-1 and cross-talk signal picked up in channel-2

One of the reasons for the disparity may be changes in Z_o, due to fabrication errors, which cause an increase in the coupling between the adjacent lines. The effect of fabrication errors is dealt with separately in section 5.1.7. Another reason may be related to the ideal parameter values assumed by the HP MDS simulator when performing the simulations.

5.1.5 Design of the 4-Channel High Frequency VCSEL Driver

The VCSELs are driven using a bias-T type driver [67] as shown in Fig. 5.15. A R-C type of bias-T has been chosen instead of the conventional L-C type for the sake of simplicity.

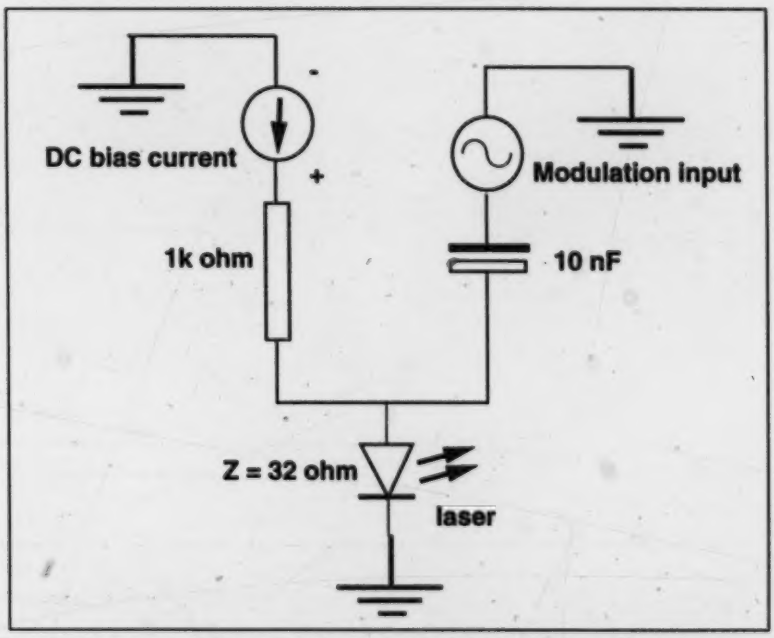

Fig. 5.15 A typical bias-T driver configuration for modulating a laser

The dynamic impedance of the laser is approximately 32 ohms and the 1000 ohm resistor isolates the AC signal by ~30 dB, in the DC path. The AC modulation signal is coupled through a 10 nF ceramic chip capacitor. The RC low frequency cut-off of the bias-T is at 497 kHz, and the high frequency roll-off, which is dependant on the self-resonant frequen-

cies of the resistor and capacitor, is greater than 7 GHz. AlN is chosen as the microwave substrate because of its high thermal conductivity (~ 170 W/m-K) [68], which enables it to act as a passive heat sink for the VCSEL array, thus eliminating the need for active Peltier coolers. In addition AlN also has a low dielectric loss, with the loss tangent $\tan\delta_\varepsilon$ = 0.0025. The substrate was supplied by the courtesy of Westaim Corp., Alberta, Canada. The VCSEL array, resistors and capacitors were bonded to the AlN substrate using thermally cured conductive silver epoxy. A fine grain silver epoxy, Epotek-3, was used which has a low contact resistance (<0.6 ohm) when cured. A photograph of the 4-channel high frequency VCSEL package is shown in Fig. 5.16, and the metal layout drawing is given in Appendix C1.

Fig. 5.16 Four-channel high frequency VCSEL package fabricated on AlN

The width of the CPW hot track (w) is 1.25 mm at the edge of the substrate, and it tapers down to $100\mu m$ in the access lines. Alternate VCSELs at $500\mu m$ pitch were wire-bonded to the access lines. The bond wires are kept shorter than 0.5 mm in order to minimize the parasitic inductance. The DC bias tracks are connected to the CPWs by wire

bonding across the ground tracks, as shown in Fig. 5.17.

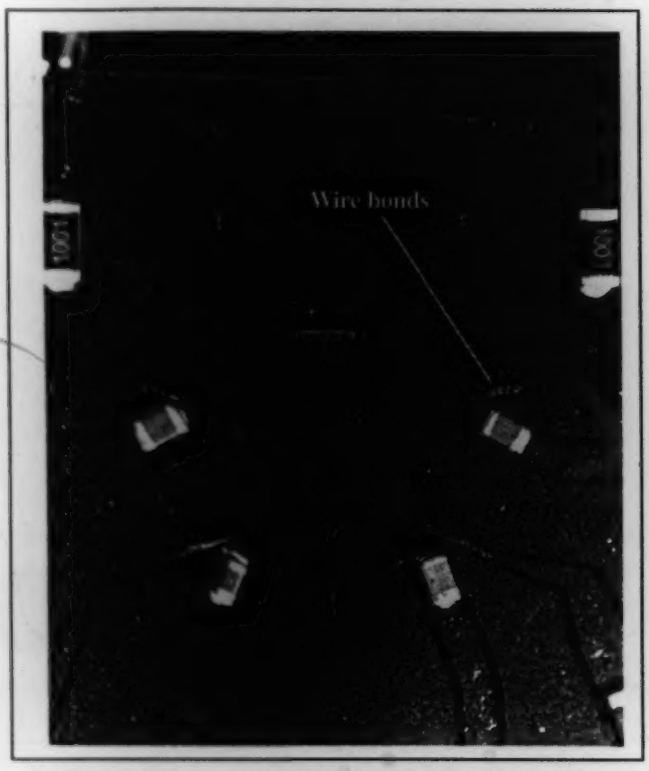

Fig. 5.17 Picture showing the details of the bias-T

5.1.6 Experimental Results of the 4-Channel VCSEL Driver

The VCSELs used in this work have a threshold current (I_{th}) between 8 and 8.5 mA and a slope efficiency of 0.4 mW/mA [69]. The operating current (I_{op}) is selected to be between 10 and 10.5 mA and the input AC peak-to-peak modulation swing is 4 mA. At I_{op} the laser emits 1.0 mW of continuous wave (CW) power P_e, and under modulation, the minimum to maximum swing is from 0.2 mW to 1.8 mW. The modulation frequency from the network analyzer is swept from 45 MHz to 5 GHz, and the output light is picked up by a $50\mu m$ core multimode fibre. The experimental setup is shown schematically in Fig. 5.18(a) and a photograph showing the fibre pick-up is given in Fig. 5.18(b).

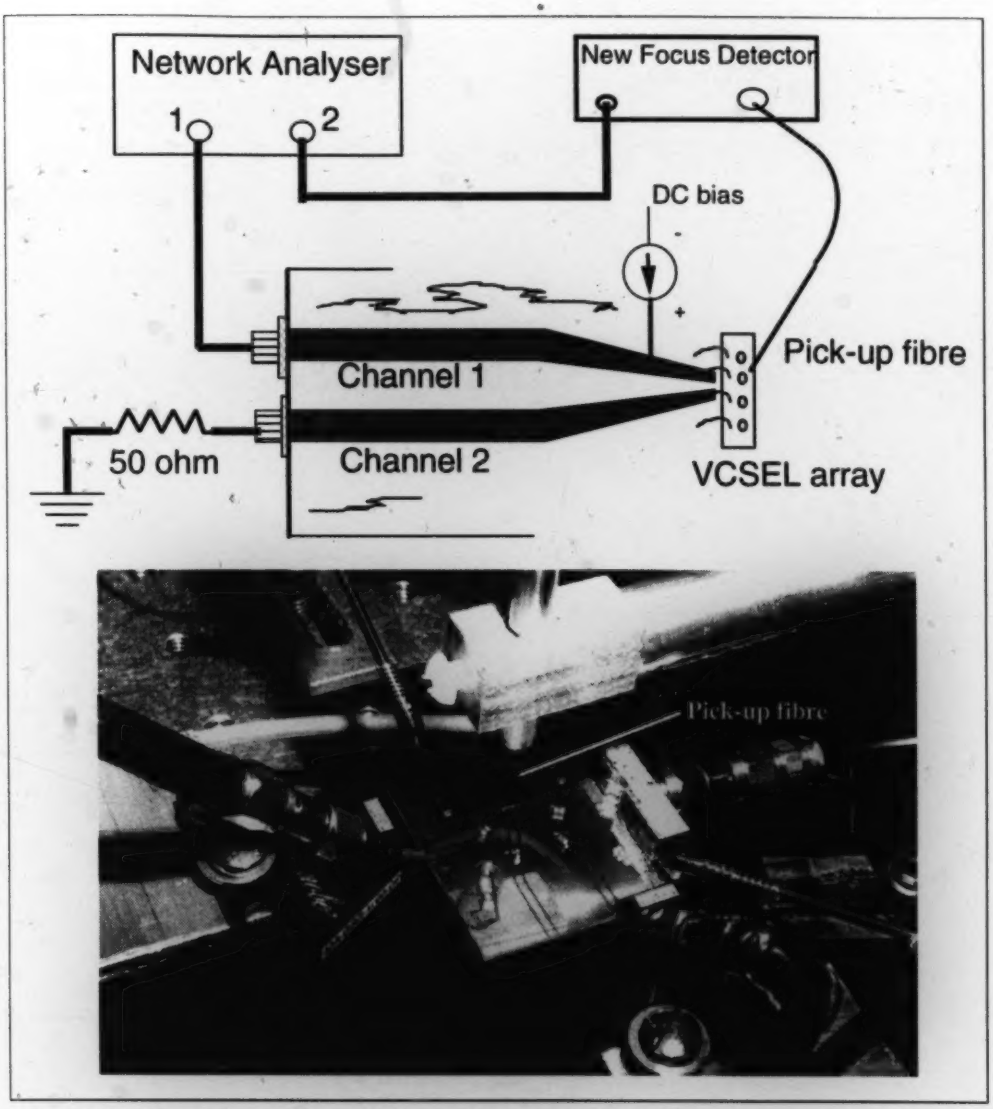

Fig. 5.18 (a)Experimental set-up for measuring the laser frequency response (b) picture of the measurement setup showing the pick-up fibre

The modulated light is detected using a New Focus detector, and fed to port-2 of the network analyzer. The S_{21} responses of the VCSELs for different bias currents are shown in Fig. 5.19(a). The S_{21} phase response and the S_{11} are illustrated in Fig. 5.19 (b) and (c) respectively. The 3 dB bandwidth of the laser is 2.64 GHz for bias currents above 10 mA.

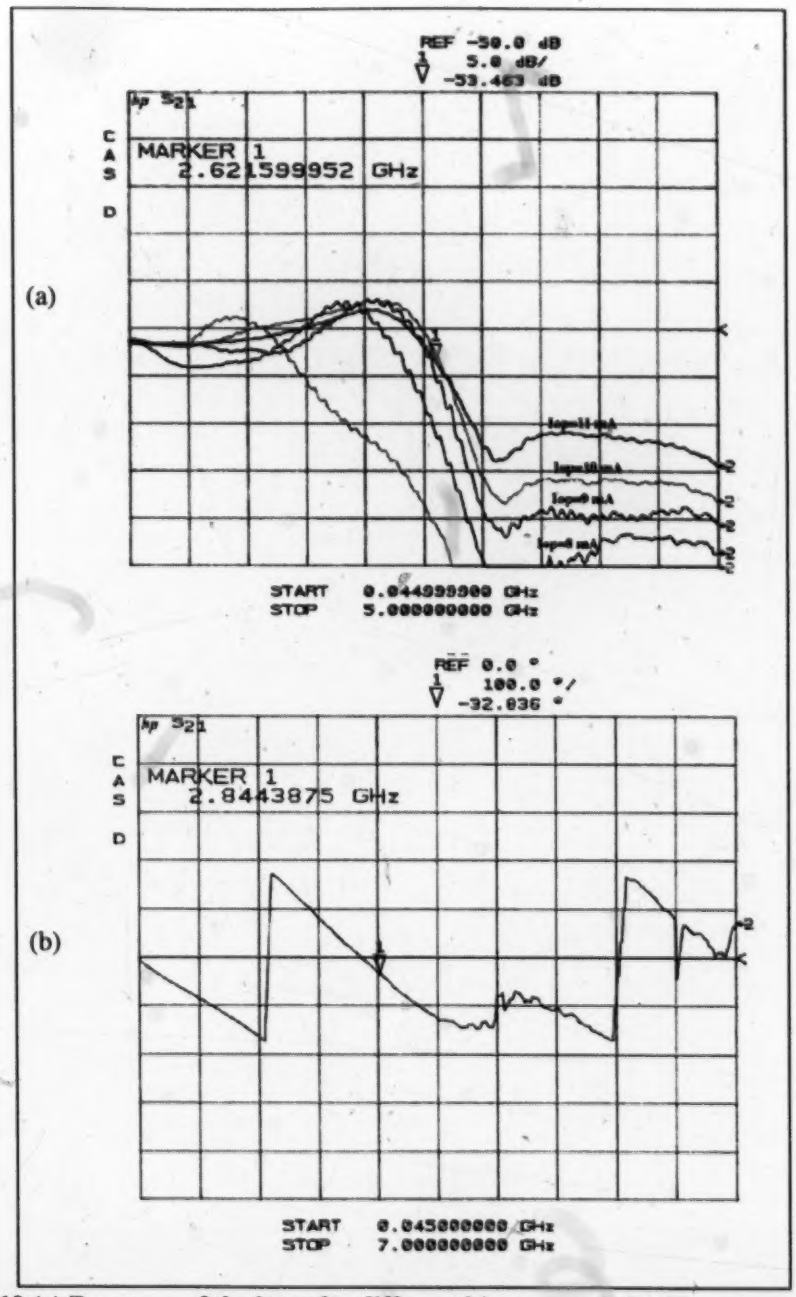

Fig. 5.19 (a) Response of the laser for different bias currents (b) Phase response at I_{op} = 11 mA

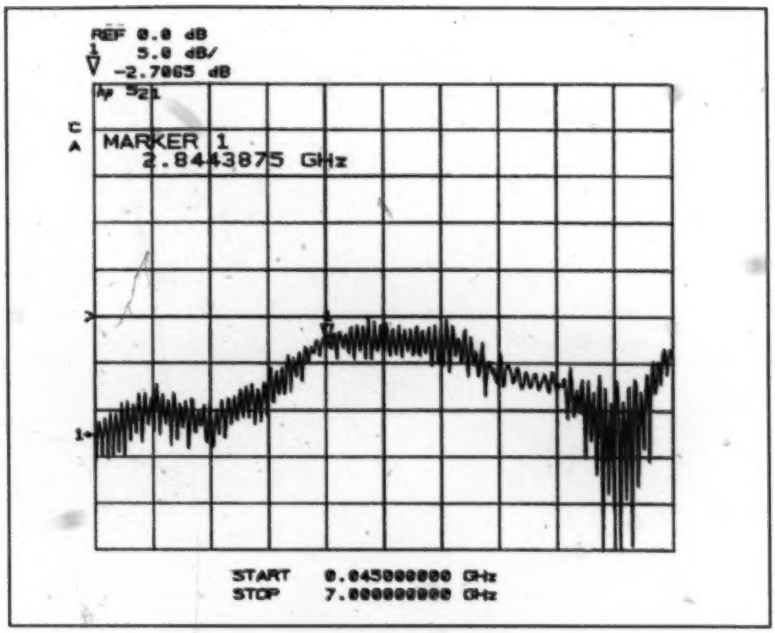

Fig. 5.19 (c) S_{11} of the laser package

In order to measure the cross-talk, the RF modulation signal is applied to an adjacent channel biased at I_{op}. The pick-up fibre is left at the same position and the laser bias is kept at I_{op}. The input is terminated in a 50 ohm load as shown in Fig. 5.20.

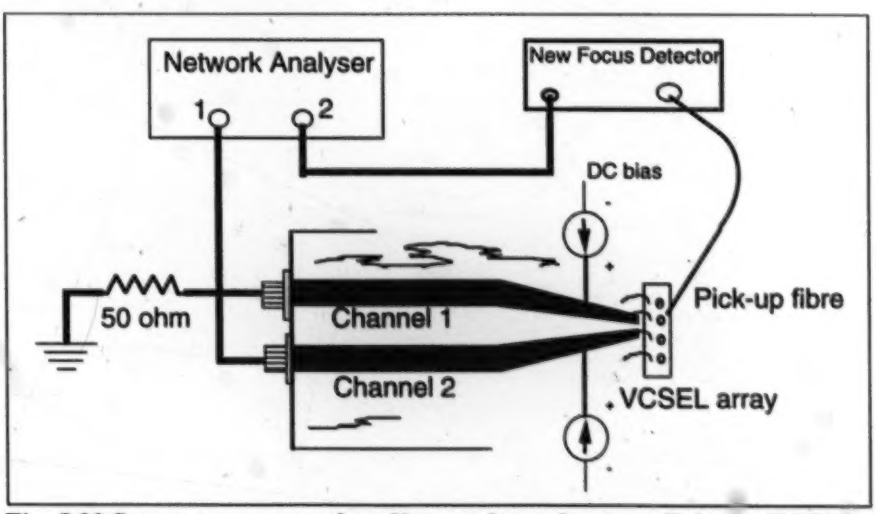

Fig. 5.20 Set-up to measure the adjacent channel cross-talk in the VCSEL

The light output from the fibre is detected and fed to the network analyzer to measure the modulation due to cross-talk. The response of the VCSEL to a modulation signal applied at its input, and the response to a modulation applied in the adjacent channel is plotted in Fig. 5.21. The average cross-talk signal is well below -33 dB up to 2 GHz and it is below (-25 dB) up to the 3 dB bandwidth frequency of 2.64 GHz. The measured cross-talk values are the lowest reported for VCSELs by any group so far [70]-[73].

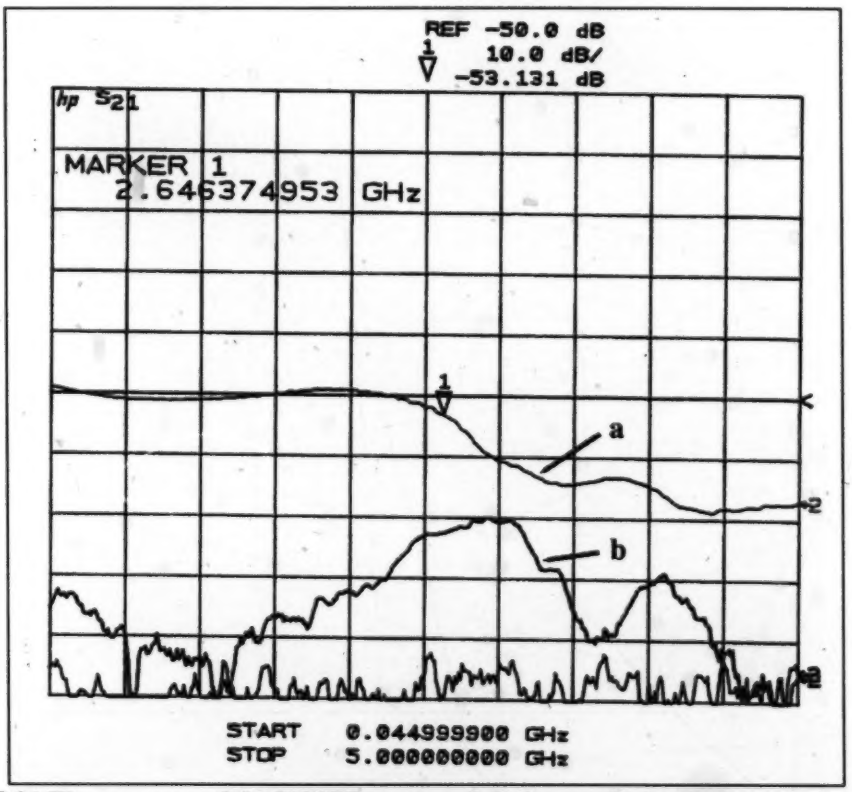

Fig. 5.21 The response of the VCSEL, to a modulation applied at its input is shown in Trace-a, and to a modulation applied in the adjacent channel is shown in Trace-b

From Fig. 5.14 it is seen that the cross-talk contribution due to the access lines is well below -45 dB up to 3.6 GHz. It could therefore be concluded that the cross-talk seen in Fig. 5.21 is entirely due to the parasitics inherent in the VCSEL device. The multichannel VCSEL driver, is therefore, not package limited but device limited. As the cross-talk in the package is very low, it can be also used as a test jig for experimentally measuring the inherent device cross-talk of VCSELs and other similar optoelectronic arrays.

5.1.7 Fabrication Errors

It is mentioned in Section 5.1.3, that the exposed photoresist pattern is transferred to the metal layers by wet chemical etching. The etching process is isotropic in nature, i.e. the metal is etched equally in all directions, resulting in an undesirable undercut of the metal tracks. The extent of undercut depends upon the thickness of metal deposited and the length of time the substrate is left in the etchant. Typically, for a metal thickness of $3.5\mu m$ the undercut in any exposed side would also be approximately $3.5\mu m$. So, for the $100\mu m$ track in Fig. 5.7, the total undercut for the two sides would be $7\mu m$. This would result in the 'hot track' width (w) in the access lines to be reduced to $93\mu m$ and the slot (s) to increase from $45\mu m$ to $52\mu m$. This change in dimensions would cause a change in Z_o, resulting in impedance mismatches. The change in Z_o, as a function of undercut is plotted in Fig. 5.22, for the access line (w = $100\mu m$, s = $45\mu m$) and for the coplanar line at the edge (w = 1mm, s = $290\mu m$). As expected, it is seen that the Z_o of the access lines are more susceptible to undercut than the wider coplanar lines at the edge.

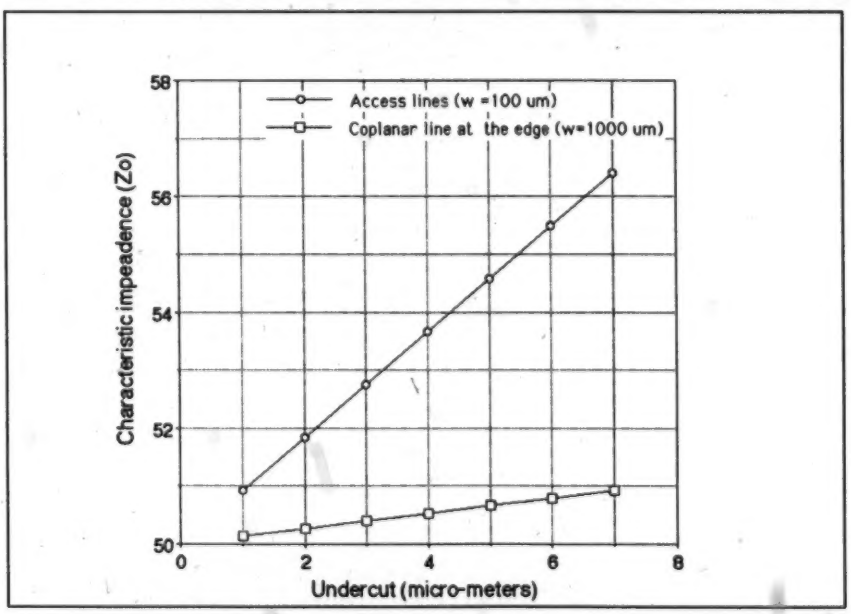

Fig. 5.22 Plot showing the change in Zo as a function of the metal undercut

5.2 Detector Cross-point Design

The detector cross-points used, as mentioned before, are linear arrays of MSM photodetectors. The planar MSM, illustrated schematically in Fig. 5.23, consists of a semiconductor absorbing layer on which two inter-digitated electrodes have been deposited to form back to back schottky diodes [74]-[77].

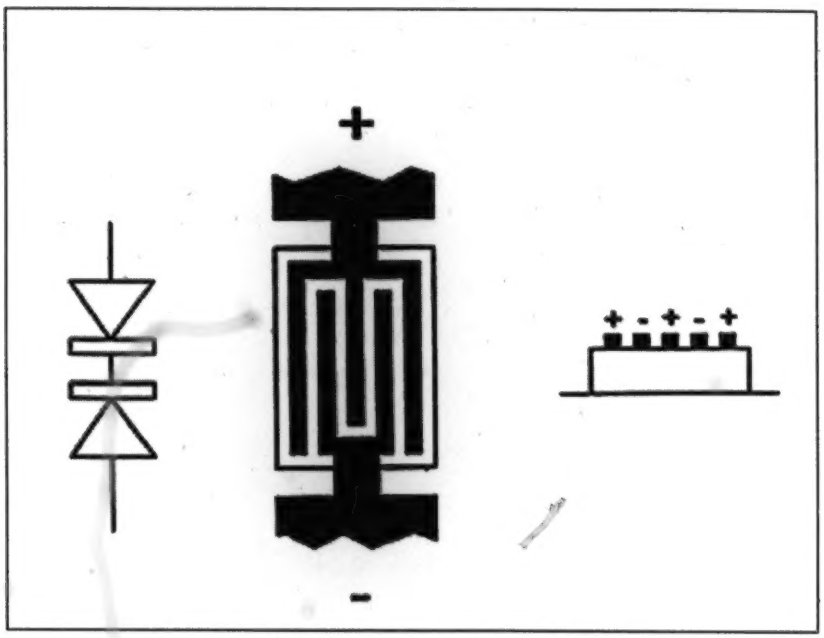

Fig. 5.23 Structure of a planar MSM

The semiconductor used in the present work consists of a thin epitaxial layer of intrinsic GaAs grown on a semi-insulating GaAs substrate. The device was designed in TRLabs and fabricated at Communication Research Centre (CRC), Ottawa [78]. The metal fingers are separated by $3\mu m$ and the overall detector area is $75\mu m$ x$75\mu m$. A photograph of the MSM detector used is shown in Fig. 5.24(a) and that of the array in Fig. 5.24(b). The array has twelve detectors separated on $250\mu m$ pitch, and for the present work any four detectors at $500\mu m$ separation could be used.

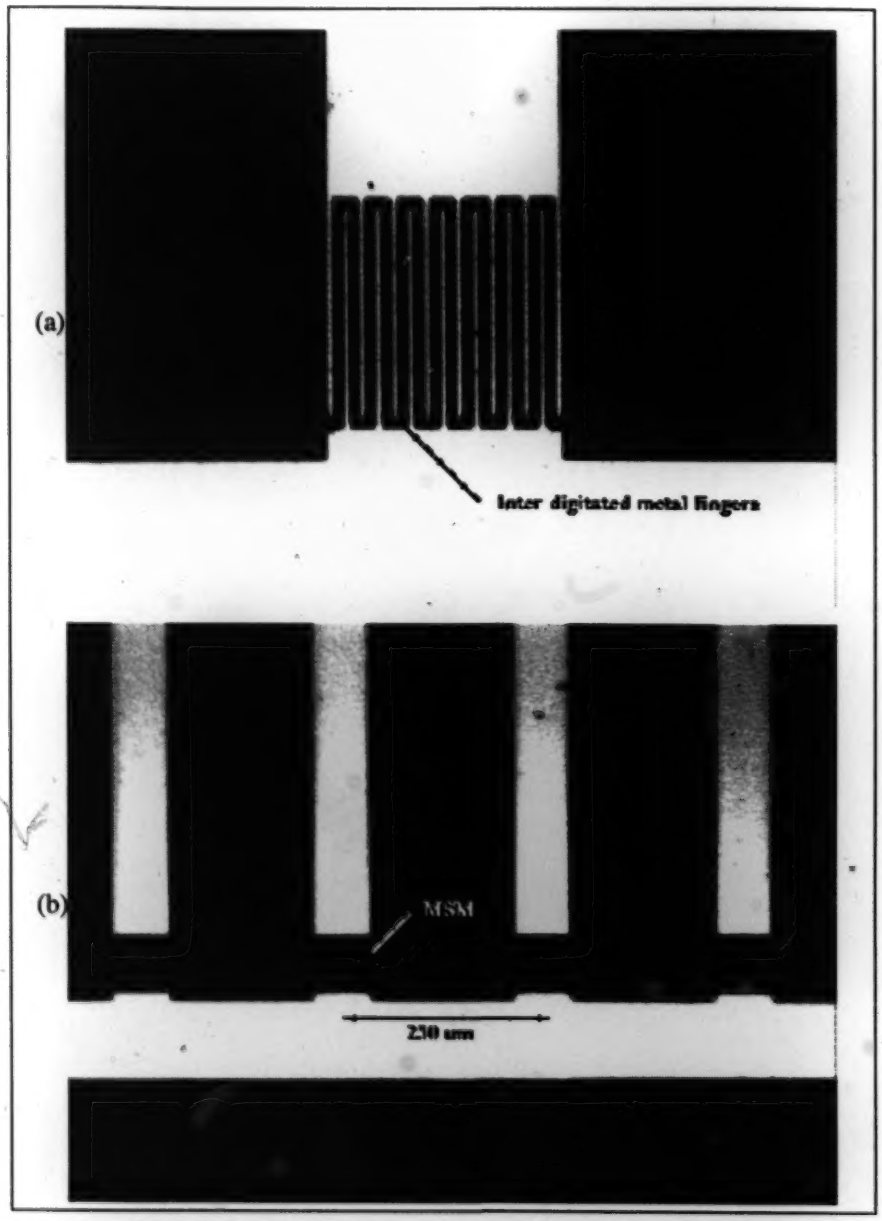

Fig. 5.24 (a) An MSM detector showing the metal fingers (b) an array of MSMs

5.2.1 MSM Biasing

The biasing circuit for the high frequency operation of the MSM array is shown in

Fig. 5.25 . The AC currents generated by the MSMs are coupled to the following amplifier stages by a 50 ohm transmission line. The AC loop on the ground side, is completed through the decoupling capacitors C1 and C2. The DC loop is completed through a 500 ohm terminating resistor, R1.

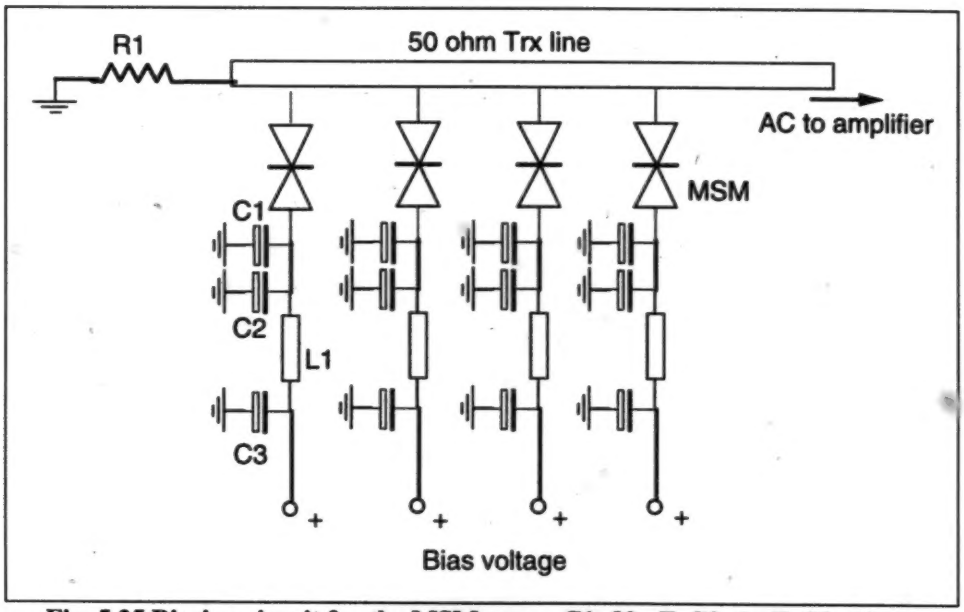

Fig. 5.25 Biasing circuit for the MSM array. C1=82 pF, C2=1 nF, C3=10 nF, L1=10 nH, R1=500 ohm

For a stable bias voltage across the MSM, it is essential that the DC potential of the 50 ohm transmission line be constant. Variations in the MSM DC current, cause a change in the MSM bias voltage, due to a variable drop across R1. The small drop across R1 may be sufficient to partially turn ON a MSM, which otherwise is biased in the OFF state, and thus severely degrade the ON-OFF contrast. To overcome this problem, feedback stabilising circuits have been suggested, and are dealt with in detail in [79]-[80]. One of the factors crucial to the high bandwidth operation of the packaged array is the proximity of the decoupling capacitor C1 to the MSM detector. The metal track between the MSM bond pad and C1 will behave, at high frequencies like a transmission line stub and exhibit frequency dependent resonant effects. To push these resonances to a frequency outside the band of interest, it is necessary to keep the physical separation of C1 from the MSM as

small as possible. Fig. 5.26(a) and (b) show the MDS simulations of the packaged array for two different proximities of C1 to the MSM.

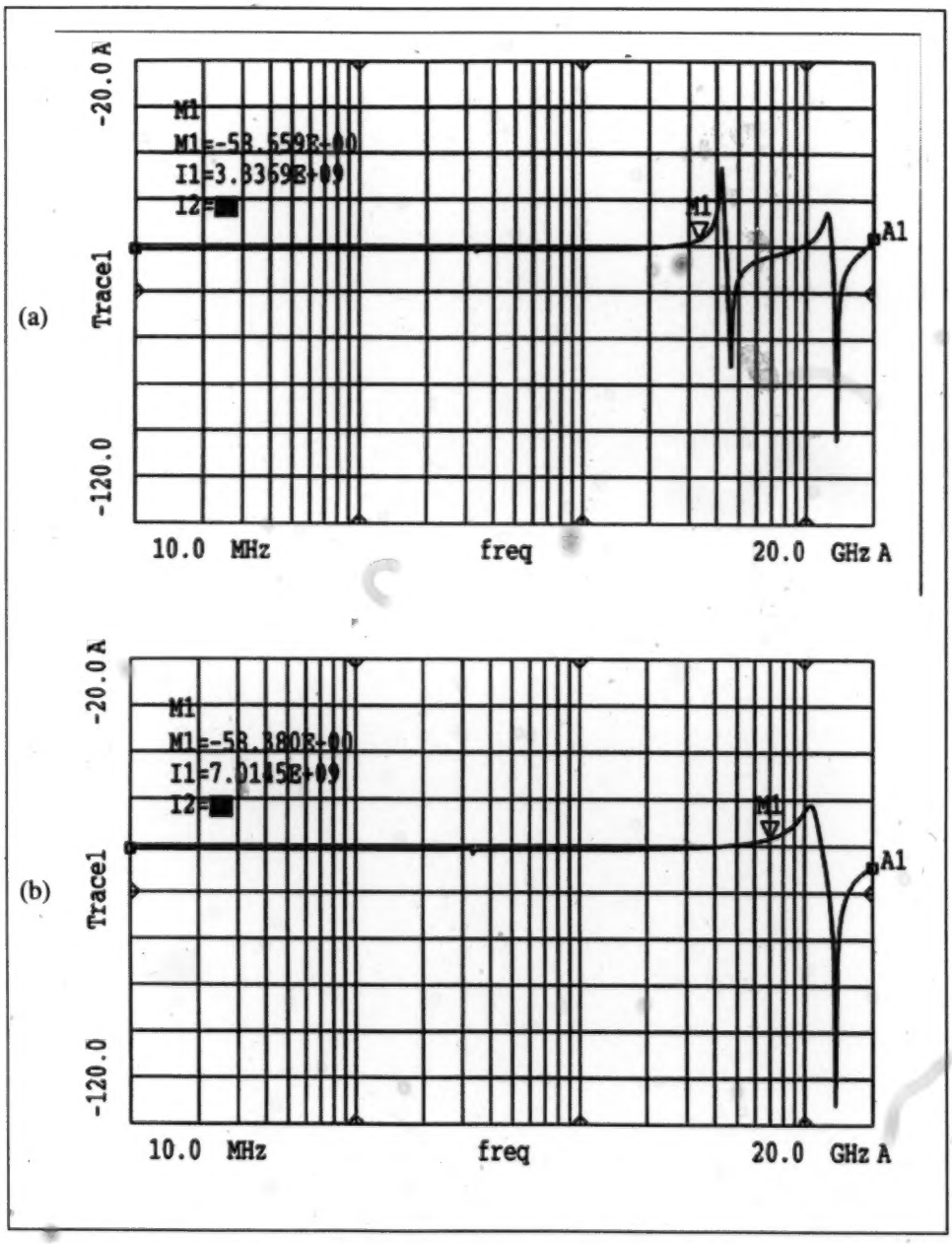

Fig. 5.26 (a) Response of the MSM array package when C1 is 9 mm away from the detector (b) response when C1 is 3 mm away

The design files are given in Appendices B5 and B6. It can be seen that the onset of resonances is pushed to 7 GHz when C1 is 3mm away, in comparison to 3.3 GHz when C1 is at 9 mm separation. The design and fabrication of a flip-chip bonded MSM detector package on Corning 7059 glass is described in the following section.

5.2.2 Fabrication of the High Frequency Detector Submount

The metal layout for the detector cross-point is shown in Fig. 5.27. The metallisation used is $3.5\mu m$ of Au on a $0.1\mu m$ NiCr adhesion layer. The pattern is transferred to the Corning 7059 glass substrate, using similar techniques as those used for the AlN substrate in Fig. 5.9. The thickness of the glass substrate is 0.71 mm, the permittivity ε_r is 5.84, and the loss tangent $\tan\delta_\varepsilon$ is 0.0036 at 10 GHz. The width of the hot track (w) is $500\mu m$ and the slot (s) is $90\mu m$ at the detector end, with w = $1000\mu m$ and s = $160\mu m$ at the edge of the substrate.

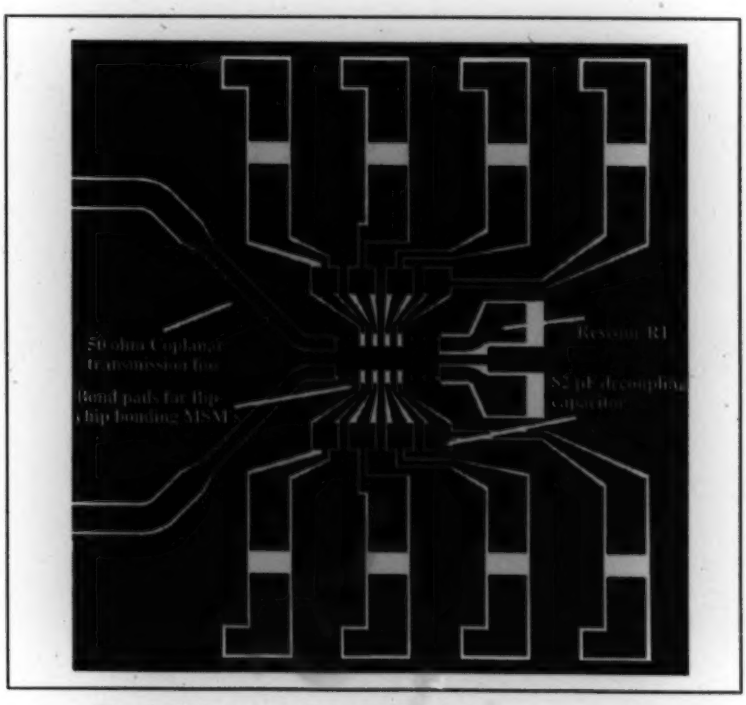

Fig. 5.27 Layout of the MSM detector cross-point

The performance of the CPW on glass substrate was tested using a setup similar to the one shown in Fig. 5.11 for frequencies up to 18 Ghz. The signals are launched and picked up by microwave probes. The S_{21} and S_{11} are plotted in Fig. 5.28(a), the phase response, group delay and the Smith chart of the S_{21} are plotted in Fig. 5.28 (b), (c) and (d) respectively.

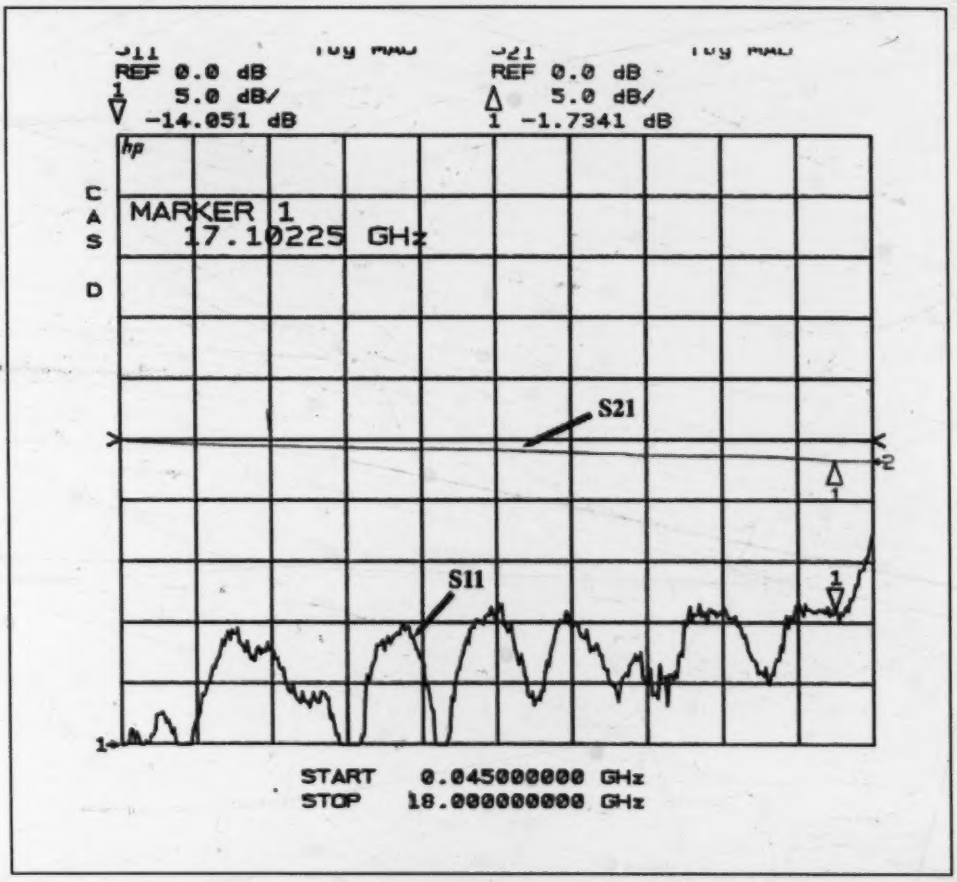

Fig. 5.28(a) The S_{21} and S_{11} of the coplanar transmission line fabricated on Corning 7059 glass substrate

The S_{21} shows very little attenuation, -1.7 dB at 18 GHz, and the phase response indicates no discernable dispersion over the measured frequency range. The results confirm the excellent microwave properties of the substrate and suggest Corning-7059 glass as a suitable transparent substrate for optoelectronic applications.

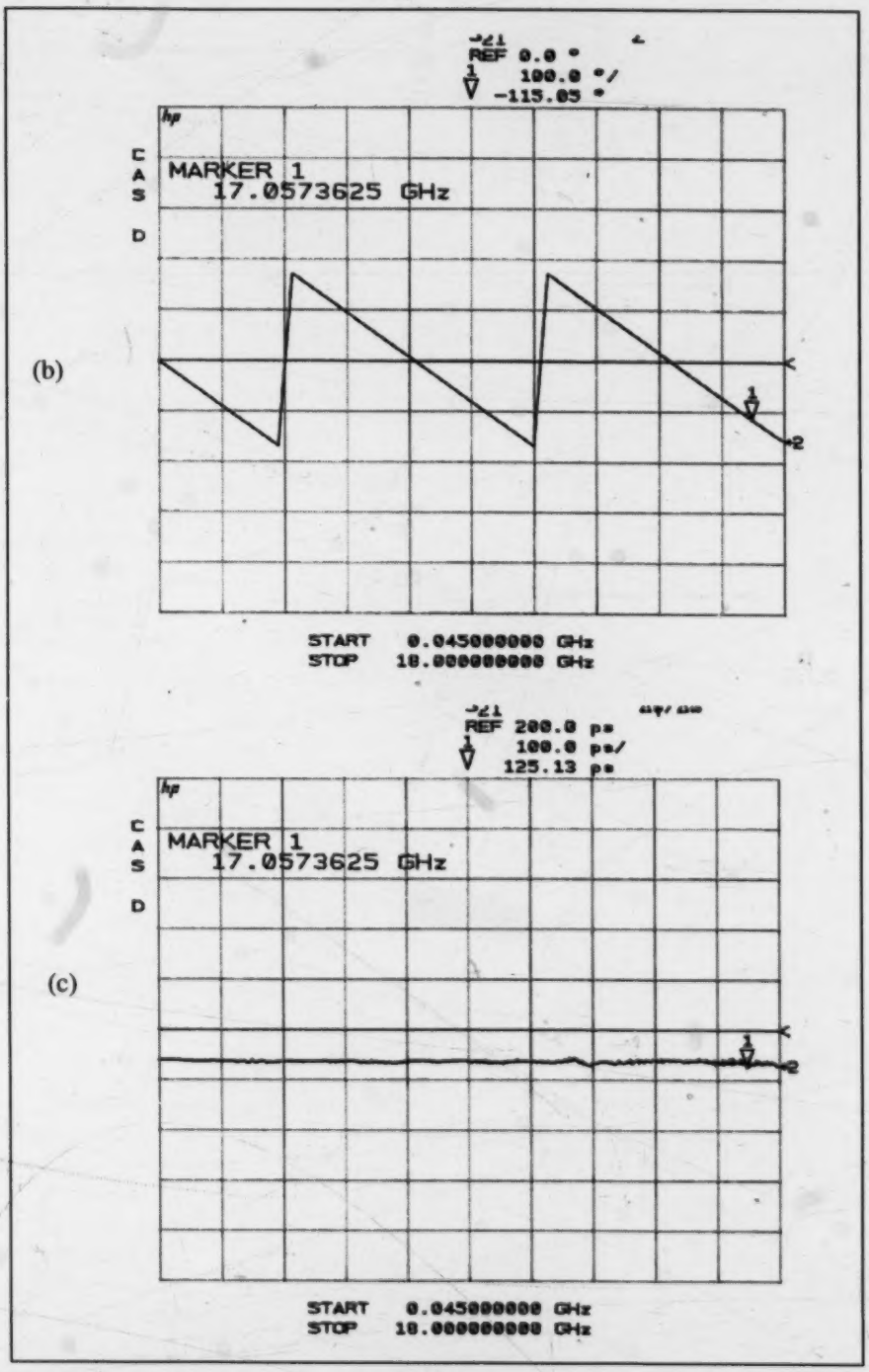

Fig. 5.28 (b) phase response of the coplanar line on glass (c) the group delay

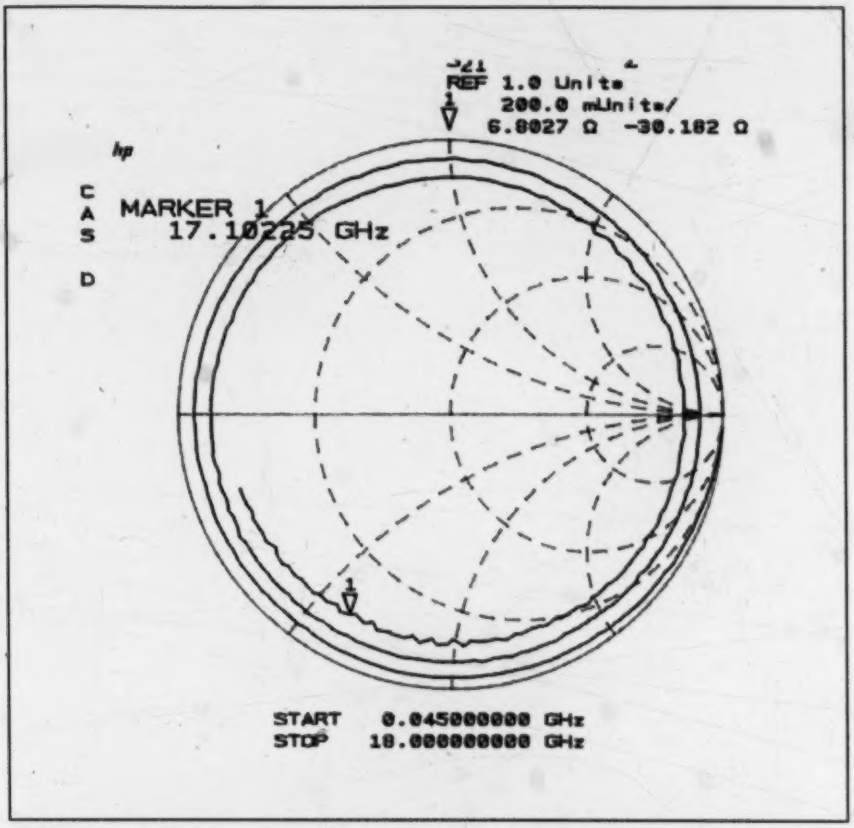

Fig. 5.28 (d) Smith chart of the S_{21} of the coplanar line on glass

The MSM detectors are mounted on the substrate by flip-chip bonding. Silver epoxy drops are first dispensed by a pressure dispensing system on the bond pads in the glass substrates. The substrate is then flipped over and carefully aligned to the bond pads on the MSM array under a magnifying camera, and bonded by pressure contact. The substrate with the MSM is placed in an oven at 120°C for 15 min. to cure the silver epoxy. Fig. 5.29 shows the flip-chip bonded MSM on the glass substrate. The other passive components are also bonded using silver epoxy. A photograph of the substrate with all components mounted is shown in Fig. 5.30. The top side of the 82 pF (C1) micro-capacitors are wire bonded to the ground tracks. To minimize parasitic inductances, the length of the wire bonds must be kept as small as possible.

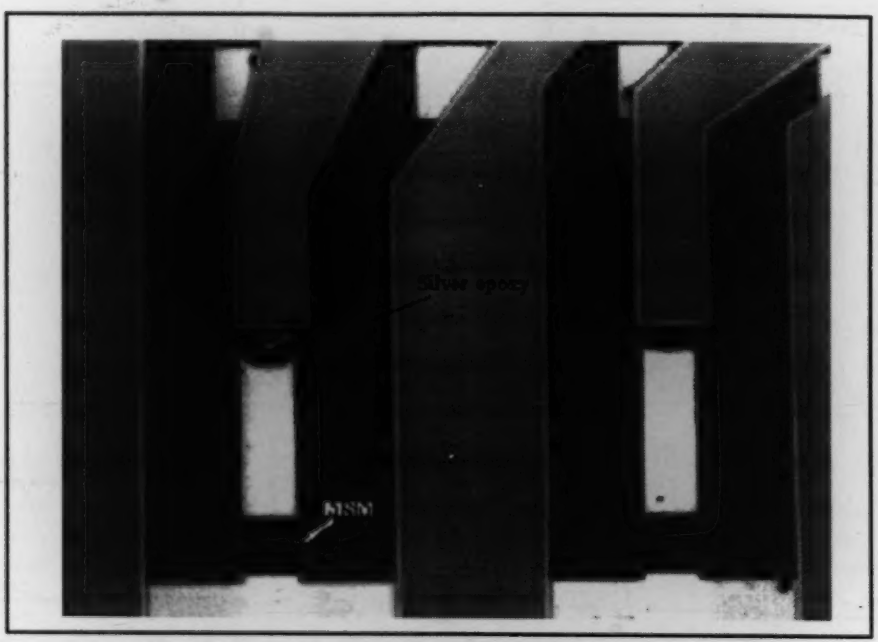

Fig. 5.29 Picture showing the MSMs flip-chip bonded with silver epoxy

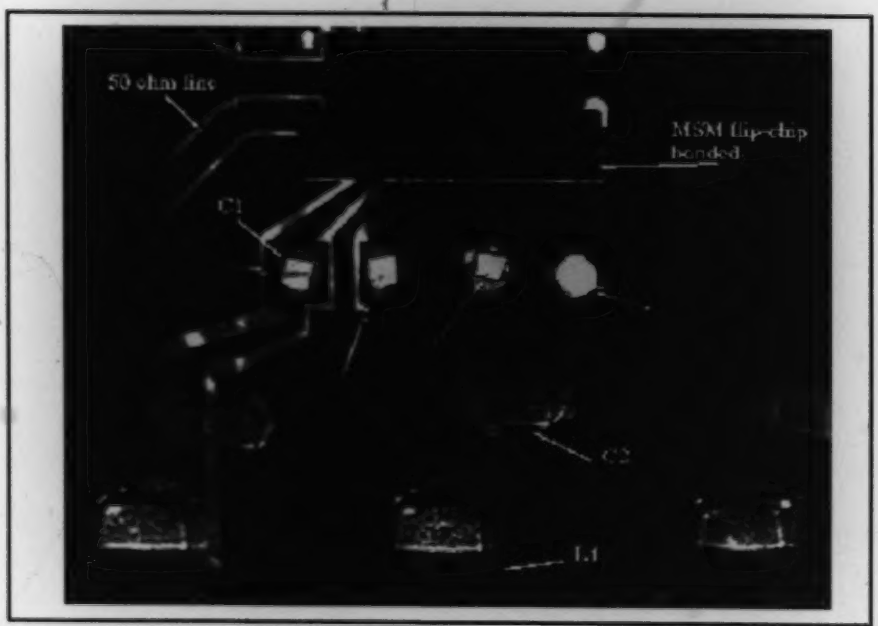

Fig. 5.30 The detector substrate with flip-chip bonded MSMs and associated biasing circuitry

5.2.3 Experimental Results

In order to test the detector performance, the setup of Fig. 5.31 is used. An 830 nm external-Mach-Zehnder modulated laser source is used as the optical input to the detector. The modulation input to the Mach-Zehnder, biased in the linear region, is derived from the network analyzer Port-1 and the detected signal from the MSM detector is fed to Port-2. The response of the MSM detector, for different bias voltages, is shown in Fig. 5.32(a) and the phase response is shown in Fig. 5.32(b). The 3 dB bandwidth of the cross-point module is approximately 2 GHz for a 10 V bias voltage. The bandwidth of the module is device limited and not package limited. This fact is confirmed from the phase response as no abrupt phase changes associated with parasitics of the packaging are seen.

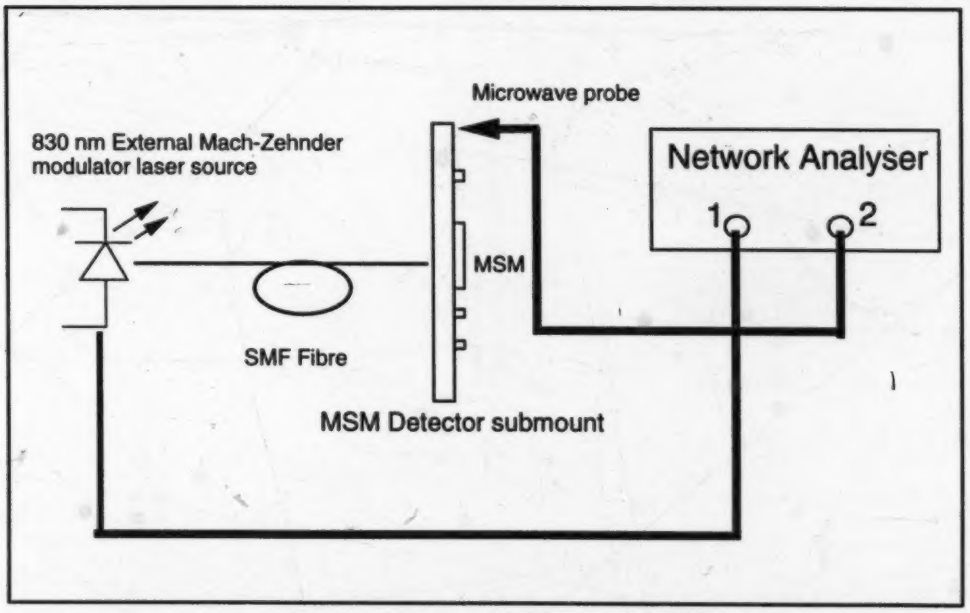

Fig. 5.31 Experimental set-up used to test the performance of the detector submount

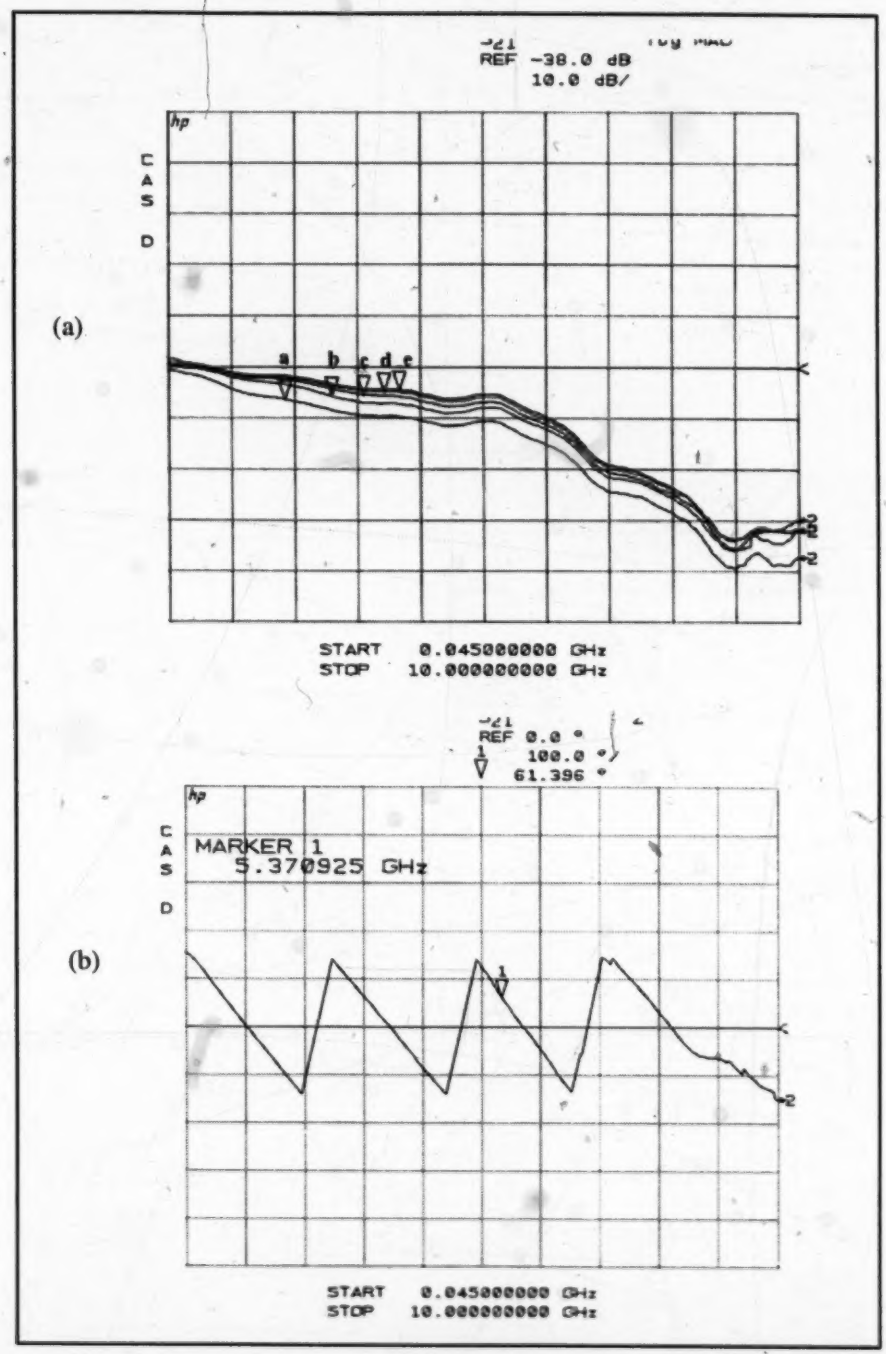

Fig. 5.32 (a) The frequency response of the MSM array at different bias voltages. The traces a, b, c, d, e are at 2V, 4V, 6V, 8V, 10V bias respectively. (b) the phase response

5.3 System Issues

In order to understand the performance limitations of the 4x4 OES, it is essential to study the various noise contributions in the system. The three main sources of impairments, which manifest as noise current at the receiver are:

- Laser Noise - laser relative intensity noise (RIN), noise due to adjacent channel electrical cross-talk
- Noise due to cross-talk in the optical distribution
- Receiver noise - shot noise, thermal noise

The average power output from the laser is $\bar{P}_e$=1 mW. The available power($\bar{P}_o$)at the detector is calculated by taking into account the (1/4) split ratio, the efficiency of the grating (82%), Fresnel reflections (~5%) and the aperture function (86%) of the beam to give

$$\bar{P}_o = 0.25\text{x}0.82\text{x}0.95\text{x}0.86\text{x}\bar{P}_e$$

$$= 0.167 \text{ mW}$$

The responsivity (R) of the MSMs is approximately 0.16 A/W [81], giving a generated photocurrent

$$\bar{I}_p = \text{R}\bar{P}_o = 26.68\ \mu A$$

The various noise contributions are calculated for a bandwidth (B) of 2 Ghz.

Laser Noise

The relative intensity noise of the laser is given by the supplier as RIN = -125 dB/Hz. The noise at the receiver due to the laser RIN ($\overline{i^2_{RIN}}$) is given by [82]

$$\overline{i^2_{RIN}} = R^2 (RIN) \bar{P}_o^2 B \qquad 5.2$$

$$= 4.51 \text{ x } 10^{-13} \text{ A}^2$$

The average cross-talk isolation computed numerically from the data of Fig. 5.21 is -35 dB for the 2 GHz bandwidth. The electrical cross-talk noise $\overline{i^2_{ECN}}$ at the receiver for this isolation is calculated to be,

$$\overline{i^2_{ECN}} = 2.26 \times 10^{-13}\ A^2$$

Noise due to cross-talk in the optical distribution

The measurement of the cross-talk isolation to stray light in the optical distribution was described in Section 4.2.2, and is found to have a value of -44.8 dB electrical. The stray light would contribute to an optical cross-talk noise $\overline{i^2_{OCN}}$ at the receiver and is calculated to be

$$\overline{i^2_{OCN}} = 2.36 \times 10^{-14}\ A^2$$

Receiver Noise

The total receiver shot noise $\overline{i^2_{SN}}$ is given as [83]

$$\overline{i^2_{SN}} = 2eB\left(\overline{I_p} + \overline{I_d}\right) \qquad 5.3$$

where $\overline{I_d}$ is the dark current of the MSM detector, e is the electronic charge. The dark current of the detectors were measured to be approximately 0.2 μA for a 10 V bias. The shot noise from Eq. 5.3 is calculated to be

$$\overline{i^2_{SN}} = 1.72 \times 10^{-14}\ A^2$$

The thermal noise of the receiver $\overline{i^2_{TN}}$ is given by [83]

$$\overline{i_{TN}^2} = \frac{4KTBF_n}{R_L} \qquad 5.4$$

where K is the Boltzman constant, T is the temperature in kelvin, F_n is the noise figure of the amplifier following the detector, R_L is the load resistance as seen by the detector. The MSM array is terminated into a low impedance (R_L = 50 ohm) front end amplifier. The amplifier has a noise figure of 3.9 dB and is a monolithic microwave integrated circuit (MMIC) packaged in TRLabs. The thermal noise at the room temperature is calculated from Eq. 5.4 to be

$$\overline{i_{TN}^2} = 1.62 \times 10^{-12}\ A^2$$

The signal-to-noise ratio of the system is given by

$$S/N = \frac{\overline{I_p}^2}{\overline{i_{RIN}^2} + \overline{i_{ECN}^2} + \overline{i_{OCN}^2} + \overline{i_{SN}^2} + \overline{i_{TN}^2}} \qquad 5.5$$

and is calculated to be

$$S/N = 24.84\ \text{dB}$$

It is easily seen from the calculation of all the noise components, that the receiver is thermal noise limited. The second dominant source of noise in the present system is the laser noise, both RIN and electrical cross-talk noise. By employing VCSELs with higher output powers and MSMs with better responsivity, it is possible to improve the S/N ratio, up to a level beyond which the laser noise would dominate, establishing a S/N ceiling. The S/N ceiling for the present system is computed to be ~ -30 dB. If further improvements in the S/N is desired, VCSELs with lower intrinsic RIN and lower device cross-talk have to be employed. VCSEL technology, having just emerged from the laboratory is far from being mature. It is the author's belief that over the next few years VCSELs with lower RIN and lower device cross-talk will be available commercially.

Chapter 6

Conclusions

The feasibility of realising a broadband optoelectronic cross-bar switch employing free-space optical signal distribution has been the main focus of research in this thesis. By design and fabrication of novel diffractive and refractive micro-optical devices, two optical distribution schemes have been implemented. In order to evaluate the bandwidth limits of the proposed OES, work has also been done in the high frequency electro-optical and opto-electrical aspects of the switch. In addition to the work on broadband free-space OES, investigations have also been carried out into the theory and fabrication of novel diffraction gratings, obtained by micromachining of silicon.

A brief description of the work done in this thesis, summarizing the important results, is described in the following sections. Future directions for further developing the free-space OES concept, and other important projects that could be engineered from the results obtained in this thesis, are also detailed.

6.1 Synopsis of Work done in Novel V-groove Gratings

A new approach to infrared beam splitting transmission gratings is proposed based on V-grooves etched in silicon. Using simple scalar theory, it is shown that 1:3, 1:5 and 1:7 equal intensity beam splitters are possible. The advantage of this method is that the self- limiting nature of anisotropic etching in silicon makes the groove depth dependant on only the groove width defined by photolithography. Designs for a V-groove beam splitter grating that can be used as a master for replication in a lower refractive index material for applications at wavelengths below the infrared are also studied. Theoretical simulations have shown the possibility of designing 1:3, 1:5 and 1:7 gratings with efficiencies of 87%, 65% and 82% respectively, in a material of refractive index 1.5. In order to experimentally verify the theoretical predictions, V-bump gratings were fabricated on a $2\mu m$ thin silicon nitride diaphragm using elaborate micromachining techniques. The gratings were tested at 675 nm and 1300 nm wavelengths by comparing the powers measured in the diffracted

orders with those predicted by theory. The results are in agreement with the theory to within 15% . It is believed that more accurate designs could be obtained if rigorous diffraction theory were used for the design of these gratings.

6.2 Synopsis of Work Done in Free-space OES

The work done in this area can be categorised into four parts; optical distribution, transmitter design, detector design and system issues.

6.2.1 Optical Distribution

Two techniques of optical imaging were designed and implemented for signal distribution in 3x3 and 4x4 OES prototypes. The cross-points of the 3x3 OES are 9 monolithic GaAs MSM photodetectors in a 3x3 rectangular array at $250\mu m$ centre-to-centre spacings. The optical distribution is achieved by convex focusing micro-lenses and a 1:3 equal intensity beam-splitting Dammann grating. The 1:3 Dammann binary gratings have a $20\mu m$ period and were etched by reactive ion etching in a CHF_3/O_2 plasma. Two configurations of the switch are considered; optical-in/electrical out and electrical-in/electrical-out. The cross-talk caused by the optical distribution system is measured to be -38.1 dB electrical for the EIEO case and -38.3 dB electrical for the OIEO case. The ON-OFF contrast obtained is -69.5 dB.

In the 4x4 OES, four input beams are collected and split by a lens-grating arrangement followed by a non-polarizing beam splitter cube. The grating used is a 1:2 splitter and the beams are further split two ways by the beam splitter cube to achieve the overall 1:4 split. The 1:2 gratings have a diffraction efficiency of 82% and are fabricated using similar RIE techniques as the gratings in 3x3 OES. The light spots on the face of the beam splitter cube are detected by linear arrays of MSM photodetectors, mounted by flip-chip bonding on a separate glass submount. The cross-talk due to the optical distribution for this scheme is measured to be -44.5 electrical.

6.2.2 Transmitter Design

Vertical cavity surface emitting laser arrays (VCSEL) are used for the electro-optical conversion of the input signals in the 4x4 OES. As the bandwidth limits of the OES are set by its terminal devices, the multichannel VCSEL array should be designed for wideband operation with low adjacent channel cross-talk. Aluminium nitride was chosen as the substrate for the transmitter module, and it acts as a good microwave substrate and a thermal heat sink for the VCSELs. The low adjacent channel electrical cross-talk is achieved by employing novel coplanar access lines. The access lines are measured to have less than -45 dB adjacent channel cross-talk up to a frequency of 3.6 GHz and well below -30 dB from 3.6 to 8 GHz. Between 8 and 18 GHz, the average adjacent channel cross-talk is well below -25 dB. The VCSELs have a 3 dB bandwidth of 2.64 GHz. The average adjacent channel cross-talk is -35 dB up to 2 GHz and well under -25 dB between 2 and 2.5 GHz. From the cross-talk results obtained for the access lines, it is concluded that the cross-talk seen in the VCSELs is entirely due to parasitics inherent in the device and not the package. The transmitter module developed is essentially device limited and not package limited. The cross-talk figures obtained for the VCSELs and the access lines are the lowest reported so far by any group.

6.2.3 Detector Cross-point Design

The detector submounts have been fabricated on Corning 7059 glass substrates. The MSM detectors are mounted on the substrate by flip-chip bonding. The performance of the CPW on glass substrate was tested for frequencies up to 18 GHz. The response shows very little attenuation, -1.7 dB at 18 GHz, and the phase response shows no discernable dispersion in the measured frequency range. The results confirm the excellent microwave properties of the substrate and suggest Corning-7059 glass as a viable transparent substrate for optoelectronic applications. The MSM's are measured to have a 3 dB bandwidth of 2 GHz, for a 10 volt bias. It is confirmed from the phase response that the bandwidth of the detector submount is device-limited, and not limited in any way by the parasitics in the package.

6.2.4 System Issues

A noise analysis was done from the various experimental data, in order to study the various impairments of the 4x4 free-space OES. The overall signal to noise ratio is calculated to be 24.84 dB for a 2 GHz bandwidth. The principle noise source is the receiver thermal noise ($\bar{I}_p^2 / \overline{i_{TN}^2}$ = 26.43 dB). The other dominant contributions are from the intrinsic laser RIN ($\bar{I}_p^2 / \overline{i_{RIN}^2}$ = 31.98 dB), and the noise due to electrical cross-talk in the laser ($\bar{I}_p^2 / \overline{i_{ECN}^2}$ = -35 dB). By employing VCSELs with higher output powers and MSMs with better responsivities, it is possible to improve the S/N ratio to a ceiling established by the laser noise (both RIN and electrical cross-talk noise). The S/N ceiling for the present system is computed to be ~ 30 dB. Another technique for improving the S/N up to the ceiling level, is by reducing the thermal noise contribution of the receiver. This could be achieved by employing a transimpedance amplifier front-end instead of the low impedance (50 ohm) front end used in the present system. Any further improvements would require better devices with lower intrinsic RIN and lower device cross-talk.

6.3 Future Directions

The work done in this thesis is the first attempt at designing an OES with free-space optical distribution. From the results obtained during the course of this thesis, it is now possible to engineer an OES commercial product that utilizes free-space signal distribution. Further development work needs to concentrate on the proper mechanical packaging of the various components. With the availability of better VCSELs and MSMs in the future, greater bandwidths with lower S/N should be achievable with the packaging technology currently developed.

In addition to free-space OES, the results obtained in this thesis have many other potential applications. By utilizing the low cross-talk high frequency packaging technique

currently developed, multi-channel optical transmitter modules for board-to-board and rack-to-rack interconnects have been designed [84]. Also, it is now a recognized fact that future fibre-optic networks would employ wavelength division multiplexing(WDM) techniques to increase the payload per optical fibre. Multi-wavelength monolithic laser arrays for transmitters and multi-channel monolithic detectors as the receivers for WDM systems are currently under investigation [85]-[86]. The low cross-talk access line scheme developed could be used in the packaging of these sources and detectors to surmount the packaging limitations currently in existence.

References

[1]John E. Midwinter ed., Photonics in switching: Vol. I & II, Academic Press Inc., San Diego, 1993.

[2] L. Thylen, G. Karlsson, O. Nilsson, "Switching technologies for future guided wave optical networks: potentials and limitations of photonics and electronics", IEEE Communications magazine, pp. 106-113, Feb. 1996.

[3] J. M. Hammer, "Modulation and switching of light in dielectric waveguides"in Integrated Optics, T. Tamir, ed. Springer-Verlag, New York, 1979.

[4] M. Gustavsson et al., "Monolithically integrated 4x4 InGaAsP/Inp laser amplifier gate switch arrays", Electron. Lett., vol. 28, pp. 2223, 1992.

[5] R. I MacDonald, E. H. Hara, "Optoelectronic broadband switching array", Electron. Lett., vol. 16, pp. 502-503, 1978.

[6] S. R. Forrest, G. L. Tangonan, V. Jones, "A simple optoelectronic 8x8 crossbar switch", J. Light wave Technol., vol. 7, no. 4, pp. 607-614, 1989.

[7] M. Veilleux, R. I. MacDonald, "An optoelectronic switching Matrix with high isolation", JLT, vol. 10, pp. 988-991, 1992.

[8] R. Sharma, Broadband optoelectronic switching and signal processing, Ph.D Thesis, Univ. of Alberta, 1996

[9] B. E. Swekla, R. I. MacDonald, "Optoelectronic transversal filter", Electron. Lett., 27, pp.1769-1770, 1991.

[10] R. I MacDonald, S.S. Lee, "Photodetector sensitivity control for weight setting in optoelectronic neural networks:, Appl. Opt., vol. 30, pp.176-178, 1991

[11] E. Munter, J. Parker, "High capacity ATM switch: Architecture and technologies," Proc. SPIE Conf. Optical Interconnects in Broadband Switching Architectures-Photon. '96 San Jose, CA, vol. 2692, Jan.-Feb. 1996, pp. 64-71.

[12] H. S. Hinton et al., "Free-space digital optical systems", Proc. of the IEEE, vol.82, no.11, pp. 1632-1649, 1994.

[13] E. G. Loewen, "Diffraction optics - A century from basic studies to mass production", Technical Digest Series-5, OSA Spring Topical Meetings '96, Boston, Massachusetts, April-May 1996, pp. 208-210.

[14] J. A. Cox, B. S. Fritz, "Tunable diffractive optical filter for imaging applications", Technical Digest Series-5, OSA Spring Topical Meetings '96, Boston, Massachusetts, April-May 1996, pp. 90-93.

[15] R. L. Morrison, "An extensible, diffractive optical system for interconnecting optoelectronic device arrays", Technical Digest Series-5, OSA Spring Topical Meetings '96, Boston, Massachusetts, April-May 1996, pp. 79-82.

[16] S. L. Dobson, P. Chen Sun, Y. Fainman, "Diffractive optical element for chromatic confocal imaging", Technical Digest Series-5, OSA Spring Topical Meetings '96, Boston, Massachusetts, April-May 1996, pp. 86-89..

[17] J. Jahns, M. M. Downs, Streibl N., Walker S.J., "Damman gratings for laser beam shaping" Opt. Eng., 28, pp.1267-1275, 1989.

[18] H. Dammann, K. Gortler, "High-efficiency in-line multiple imaging by means of multiple phase holograms," Opt. Commun. 3, pp. 312-315, 1971.

[19] H. Dammann, E. Klotz, "Coherent-optical generation and inspection of two-dimensional periodic structures", Optica Acta, **24**, pp.505 - 515, 1977.

[20] L. P. Boivin, "Multiple imaging using various types of simple phase gratings", Appl. Opt. 11, pp. 1782-1792, 1972.

[21] W. H. Lee, "High efficiency multiple beam gratings", Appl. Opt. 18, pp. 2152-2158, 1982.

[22] U. Killat, G. Rabe, W. Rave, "Binary phase gratings for star couplers with high splitting ratio", Fiber and Integrated Opt., 4, pp. 159-167, 1982.

[23] W. B. Veldkamp, J. R.. Leger, and G. J. Swanson, " Coherent summation of laser beams using binary phase gratings", Opt. Lett. 11, pp. 303-305, 1986.

[24] S. D. Conte and C. de Boor, Elementary Numerical Analysis, McGraw-Hill, New York , 1980.

[25] U. Krackhardt, N. Striebel, "Design of Dammann gratings for array generation", Opt. Commun., 74, pp. 31-36, 1989.

[26] Diffractive Optics workshop - Course Notes, Georgia Tech, March-1994.

[27] S. M. Shank, M. Skvarla, F. T. Chen, H. G. Craighead, P. Cook, R. Bussjager, F. Haas and D. A. Honey, "Fabrication of multi-level phase gratings using focused ion beam milling and electron beam lithography", Paper DWD3, p. 302-5, OSA Technical Digest, Diffractive Optics: Design, Fabrication and Applications, June 6-9, Rochester, NY, 1994.

[28] K. E. Bean, "Anisotropic etching of silicon" IEEE Trans. Elect. Dev., ED-25, pp. 1185-1193, 1978.

[29] U. U. Graf, D. T. Joffe, E. J. Kim, J. H. Lacy, H. Ling, J. T. Moore and G. Rebeiz, "Fabrication and evaluation of an etched infrared diffraction grating", Appl. Optics, 33, pp. 96-102, 1994.

[30] Narendra R., McMullin J. N., "Single-mode, phosphorous-doped silica waveguides in silicon V-grooves", IEEE Phot. Tech. Lett., **5**, pp. 43-46, 1993.

[31] Tsang W., Wang S. , "Thin-film beam splitter and reflector for optical guided waves", App. Phys Lett. , **27**, pp. 588-590, 1975.

[32] Sriram S., Brandt G. B., Supertzi E. P., "Heterodyne receiver on silicon: an excercise in integration", Proc. SPIE Vol. 321, pp. 15, 1982

[33] Sriram S., Supertzi E. P., "Novel V-groove structures on silicon", App. Optics, 24, pp. 1784-1787, 1985.

[34] J. B. Price , "Anisotropic etching of silicon with KOH-H_2O-isopropyl alchohol", ECS Semiconductor Silicon 1973, pp. 339-353.

[35] H. Siedel et al., "Anisotropic Etching of crystalline silicon in alkaline solutions", J. Electrochem. Soc., vol.137, no.11, pp. 3612-3626, 1990.

[36] Ken Macleod, Micromachined serial taps in Si waveguides, Msc. Thesis, Univ. of Alberta, 1995.

[37] M. Mehreganry, S. Senturia, "Anisotropic etching of silicon in hydrazine", Sensors and Actuators, vol.13, pp. 375-390, 1988.

[38] G. Findler, J. Muchow, M. Koch, H. Munzel, "Temporal evolution of silicon surface roughness during anisotropic etching process", Proc. of Micro Electro Mechanical Systems '92, pp. 62-66, 1992.

[39] N. Rajkumar, J. N. McMullin, "V-groove gratings on silicon for infrared beam splitting", Appl. Opt., vol.34, no.14, pp. 2556-2559, !995.

[40] Allen Cox J., Felix P. Shvartsman, "Image quality assessment of diffractive elements replicated in Surphex", Paper DThB4, p. 346-9, OSA Technical Digest, Diffractive Optics: Design, Fabrication and Applications, June 6-9, Rochester, NY, 1994.

[41] R. Nagarajan, J. N. McMullin, "Fabrication and testing of silicon V-groove gratings", MJJ6, OSA Annual General Meeting at Portland, Oregon, Sept.-1995.

[42] N. Rajkumar, J. N. McMullin, B. P. Keyworth, R. I. MacDonald, "3x3 optoelectronic switch using diffractive optics", MJJ5, OSA Annual General Meeting at Portland, Oregon, Sept.-1995.

[43] N. Rajkumar, J. N. McMullin, B. P. Keyworth, "3x3 optoelectronic cross-bar switch using vertical cavity surface emitting laser arrays", Technical Digest Series-5, OSA Spring Topical Meetings '96, Boston, Massachusetts, April-May 1996, pp. 75-78

[44] N. Rajkumar, J. N. McMullin, B. P. Keyworth, "Optoelectronic cross-bar switching using free-space optical distribution", IEEE Photon. Technol. Lett., vol. 8, no.11, pp. 1534-1536, 1996.

[45]B. K. Senthil, "Connectors for fiber ribbon cables", Telecommunication Research Laboratories, Internal report, TR-92-07, July 1992.

[46] B. P. Keyworth, J. N. McMullin, "Method and apparatus for making optical components by direct dispensing of curable liquid", U.S. Patent 5 534 101, 9 July 1996.

[47] B. P. Keyworth, D. J. Corazza, J. N. McMullin, L. Mabbott, "Single-step fabrication of refractive micrlens arrays", Appl. Opt., to be published.

[48] B. E. A. Saleh, M. C. Teich, Fundamentals of Photonics, John Wiley and Sons Inc., pp. 80, 1991.

[49] Reinmut K. Hoffmann, Handbook of microwave integrated circuits, Artech House Inc., Norwood, MA, pp. 351, 1987.

[50] B. Weigel, M. Grabherr, R. Michalzik, G.Reiner, K. J. Ebeling, "High power single-mode selectively oxidised vertical cavity surface emitting laser arrays", IEEE Photon. Technol. Lett., vol. 8, no.8, pp. 971-973, 1996.

[51] M. K. Hibbs-Brenner, R. A. Morgan, et al., "Performance uniformity and yeild of 850 nm VCSELs deposited by MOVPE", IEEE Photon. Technol. Lett., vol. 8, no.1, pp. 7-9, 1996.

[52] P. R. Brusenbach, S. Swirhun, T. K. Uchida, M. Kim, C. Parsons, "Equivalent circuit for vertical cavity top surface emitting lasers", Electron. Lett., vol.23, no.23, pp. 2037-2038, 1993.

[53] T. E. Sale, J. S. Roberts, J. Woodhead, J. P. R. David, P. N. Robson, "Room tempra-ture visible (683-713 nm) all-AlGaAs vertical cavity surface emitting lasers (VCSELs)", IEEE Photon. Technol. Lett., vol. 8, no.4, pp. 473-475, April 1996.

[54] Y. Ohsio, K. Tateno et al., "Flip-chip bonded 0.85μm bottom emitting vertical cavity surface emitting laser array on an AlGaAs substrate", IEEE Photon. Technol. Lett., vol.8, no.9, pp. 1115-1117, 1996.

[55] E. H. Fooks, R. A. Zakarevicius, Microwave engineering using microstrip circuits, Prentice Hall of Australia, 1990, pp.40.

[56] E. H. Fooks, R. A. Zakarevicius, Microwave engineering using microstrip circuits, Prentice Hall of Australia, 1990, pp.92.

[57] T. Hayashi, M. Usui, M. Hosoya, K. Sato, S. Sekine, "Reducing electrical crosstalk in laser diode array modules by using a fim-carrier interconnection", J. Lightwave Technol., vol. 13, no.9, pp. 1885-1891, 1995.

[58] R. J. P. Douville, D. S. James, "Experimental study of symmetric microstrip bends and their compensation", IEEE Trans. Microwave Theory nad Techniques, vol. MTT-26, no.3, pp. 175-82, 1978.

[59] C. P. Wen, "Coplanar waveguide: A surface strip transmission line suitable for nonreciprocal gyromagnetic device applications", IEEE Trans. Microwave Theory nad Techniques, vol. MTT-17, pp. 1087-1090, 1978

[60] P. Dupuis, C. K. Campbell, "Characteristic impeadence of surface-strip coplanar waveguides", Electron. Lett., vol.23, pp. 354-355.

[61] Y. C. Shih, T. Itoh, "Analysis of conductor backed coplanar waveguide", Electron. Lett., vol,18, no.12, pp. 538-540, 1982.

[62] G. Ghione, C. U. Naldi, "Coplanar waveguides for MMIC applications: Effect of upper shielding, conductor backing, finite-extent ground planes, and line-to-line coupling", IEEE Trans. Microwave Theory and Techniques, vol. MTT-35, no.3, pp. 260-267, 1978

[63] David M. Pozar, Microwave Engineering, Addison-Wesley Publishing Inc., 1990, pp. 26.

[64] Reinmut K. Hoffmann, Handbook of microwave integrated circuits, Artech House Inc., Norwood, MA, pp.109, 1987.

[65] Product specifications for 40A-GSG-150-DUAL, Picoprobe by GGB Industries Inc., Naples, Florida.

[66] G. Gronau, A. Felder, "Coplanar-waveguide test fixture for characterisation of high speed digital circuits upto 40 GBit/s", Electron. Lett., vol.29, no.22, pp. 1939-1941, 1993

[67] John. M. Senior, Optical fiber Communications, 2 ed., Prentice Hall International (UK) Ltd., 1992, pp. 596.

[68] Westaim Corp., Alberta: Private Communication.

[69] Product specifications for VCSEL (LA-M), Vixel corp., Broomfield, Colorado.

[70] M. W. Maeda, C. Chang-Hasnain, A. Von Lehmen, H. Izadpanah et al., "Multigigabit/s operation of 16-wavelength vertical-cavity surface-emitting laser array", IEEE Photon. Technol. Lett., vol. 3, no.10, pp. 863-865, 1996.

[71] H. Kosaka, A. K. Dutta, K. Kurihara, Y. Sugimoto, K. Kasahara, "Gigabit-rate optical-signal transmission using verical cavity surface-emitting lasers with large-core plastic-cladding fibers", IEEE Photon. Technol. Lett., vol.7, no.8, pp. 926-928, 1996.

[72] Y. Wong, D. J. Muehlener et al., "Technology development of a high density 32-channel 16-Gb/s optical data link for optical applications for the optoelectronic technology consortium (OETC)", J. Lightwave Technol., vol. 13, no.6, pp. 995-1013, 1995.

[73] K. H. Hahn, "POLO-Parallel optical links for gigabyte data communication", Proc. 45th ECTC, Las Vegas, NV, May 1995, pp. 368-375.

[74] M. Makiuchi, H. Hamaguchi, T. Kumai, M. Ito, O. Wada, T. Sakurai, "A monolithic four-channel photoreceiver integrated on GaAs substrate using metal-semiconductor-matal photodiodes and FETs", IEEE Electron. Devices Lett., vol. EDL-6, pp. 634-635, 1985.

[75] J. B. D. Soole, H. Schumacher, "InGaAs Metal-semiconductor-metal photodetectors for long wavelength optical communications", IEEE J. Quantum Electron., vol.27, no.3, pp. 737-752., 1991.

[76] E. H. Bottcher, D. Kuhl, F. Hieronymi, E. Droge, T. Wolf, D. Bimberg, "Ultrafast semiinsulating Inp: Fe-InGaAs:Fe-InP:Fe MSM photodetectors: Modelling and performance", IEEE J. Quantum Electron., vol.28, no.10, pp. 2343-2357, 1992.

[77] S. Y. Wang, D. M. Bloom, "100 GHz bandwidth planar GaAs schottky diode", Electron. Lett., vol.19, pp. 354-355, 1983

[78] R. I. MacDonald, TRLabs: Private Communication.

[79] D. Lam, Optoelectronic Reflex signal processor, MSc Thesis, Univ. of Alberta, 1994.

[80] John E. Midwinter ed., Photonics in switching: Vol. I & II, Academic Press Inc., San Diego, 1993, pp. 184.

[81] Ray deCorby, TRLabs: Private Communication.

[82] John. M. Senior, Optical fiber Communications, 2 ed., Prentice Hall International (UK) Ltd., 1992, pp. 343

[83] John. M. Senior, Optical fiber Communications, 2 ed., Prentice Hall International

(UK) Ltd., 1992, pp. 476

[84] D. J. Corazza, N. Rajkumar, B. P. Keyworth, J. N. McMullin, R. I. MacDonald, "Wideband four channel optical transmitter package using vertical cavity surface emitting laser arrays", vol. 3005-47, Photonics West' 97, Proc. of SPIE conf. on Optoelectronic Interconnects and Packaging, San Jose, California, Feb. 1997.

[85] Y. H. Lo, L. A.Wang, A. S. Gozdz, P. S. D. Lin, M. Z. Iqbal, R. Bhat, T. P. Lee, "Four channel integrated DFB laser array with tunable wavelength spacing and 40-Gb/s signal transmission capacity", IEEE, J. Lightwave Technol. vol.11, no.4, pp. 619-623, 1993

[86] S. Chandrasekhar, L. D. Garret, L. M. Lunardi, A. G. Dentai, C. A. Burrus, E. C. Burrows, "Investigations of crosstalk performance of eight-channel p-i-n/HBT OEIC photoreceiver array modlues", IEEE Photon. Technol. Lett., vol.8, no.5, pp. 682-684, 1996.

Appendix A

Silicon Micromachining - The Fundamentals

Silicon belongs to the diamond cubic crystal structure. In the cubic structure the crystallographic directions are perpendicular to the crystal planes. It is known that the <111> direction has a very high atomic packing density in the (111) plane compared to, say the (100) or the (110) plane. This would cause etch rate, or epitaxial deposition growth rates to be considerably faster in the <100> and <110> directions than in the <111> direction. Strong alkaline solutions like KOH, for example, would etch silicon much faster in the <100> direction than in the <111> direction [34].

Fig. A.1(a) shows a (100) silicon wafer with (110) alignment flats. When this wafer is aligned along (110) flats and lines or windows parallel to the flats are patterned on a masking layer (SiO_2 or Si_3N_4) by lithography, and the wafer dipped in a KOH solution, interesting anisotropic etching phenomena are observed. The different stages of etching are shown in Fig. A.1(b) The etching proceeds in the <100> direction into the wafer until the etch front hits the {111} planes which limit the rate of etching drastically and for all practical purposes acts as an etch stop. If the wafer is left to etch for a long time, eventually the {111} planes will meet defining a V-shaped groove. The etch depth to oxide opening ratio is $(1/\sqrt{2})$. So, for example, if we open an oxide pattern line 10 μm wide, a groove 7.07 μm deep will be formed.

The two most commonly used anisotropic etchants for silicon are aqueous KOH and an aqueous mixture of ethylenediamine and pyrocatechol (EDP) [35]. Some of the rarely used etchants are hydrazine, tetramethyl ammonia hydroxide (TMAH), cesium hydroxide (CsOH), and ammonium hydroxide NH_4OH. For the present work KOH is used as the etchant as it is much safer than EDP, and its etch rate and performance are predictable and well characterized [36]. The exact etching mechanism is still not very well understood, but the general consensus [37]-[38], is that the reaction taking place is

$$Si + 2OH^- + 2H_2O \rightarrow SiO_2(OH)_2^{--} + 2H_2$$

The silicate $SiO_2(OH)_2^{--}$ dissolves into the etching solution and the hydrogen bubbles out.

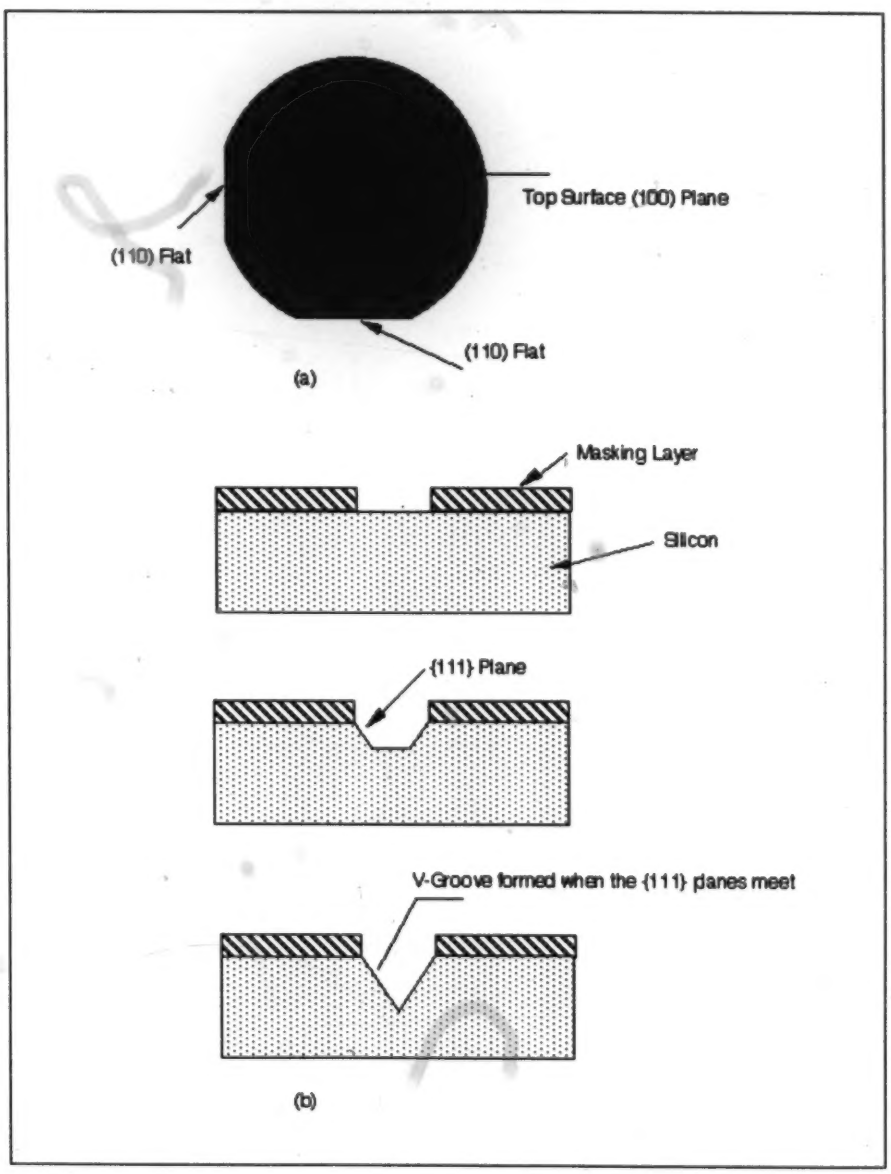

Fig. 3.1 (a) (100) silicon wafer (b) Stages in the anisotropic etching of silicon

Appendix B

MDS Design files

B1 Layout Simulation of Fig. 4.9.

B2 Simulation of Fig. 4.9 with coplanar lines

B3. Microstrip access lines

B4 Coplanar access lines

B5 Detector package with C1 9 mm away

B6 Detector Package with C1 3 mm away

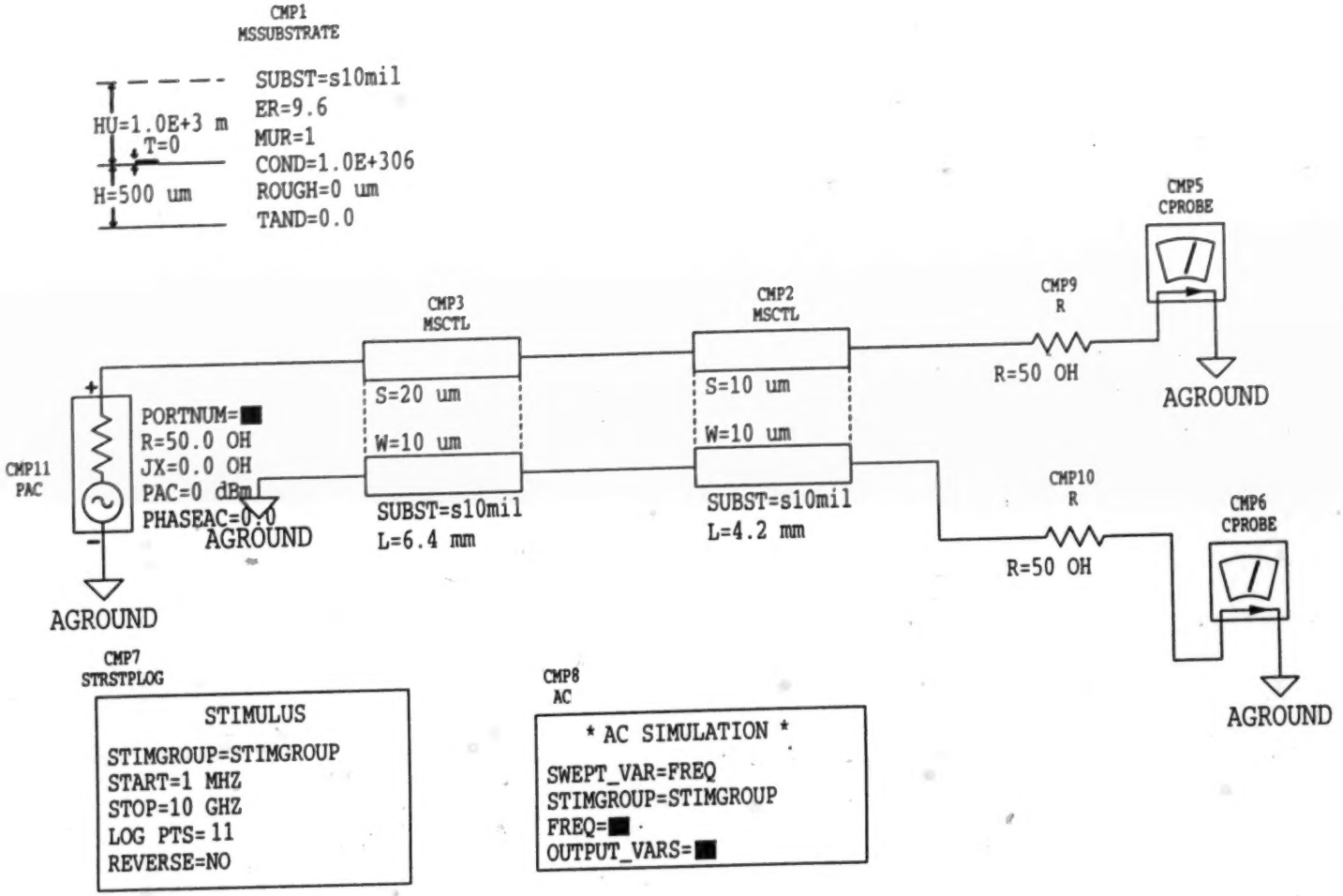
CMP1
MSSUBSTRATE
SUBST=s10mil
ER=9.6
MUR=1
COND=1.0E+306
ROUGH=0 um
TAND=0.0
HU=1.0E+3 m
T=0
H=500 um
CMP5
CPROBE
CMP9
R
R=50 OH
AGROUND
CMP3
MSCTL
CMP2
MSCTL
S=20 um
W=10 um
S=10 um
W=10 um
CMP11
PAC
PORTNUM=
R=50.0 OH
JX=0.0 OH
PAC=0 dBm
PHASEAC=0.0
AGROUND
SUBST=s10mil
L=6.4 mm
SUBST=s10mil
L=4.2 mm
CMP10
R
CMP6
CPROBE
R=50 OH
AGROUND
AGROUND
CMP7
STRSTPLOG
STIMULUS
STIMGROUP=STIMGROUP
START=1 MHZ
STOP=10 GHZ
LOG PTS=11
REVERSE=NO
CMP8
AC
* AC SIMULATION *
SWEPT_VAR=FREQ
STIMGROUP=STIMGROUP
FREQ=
OUTPUT_VARS=

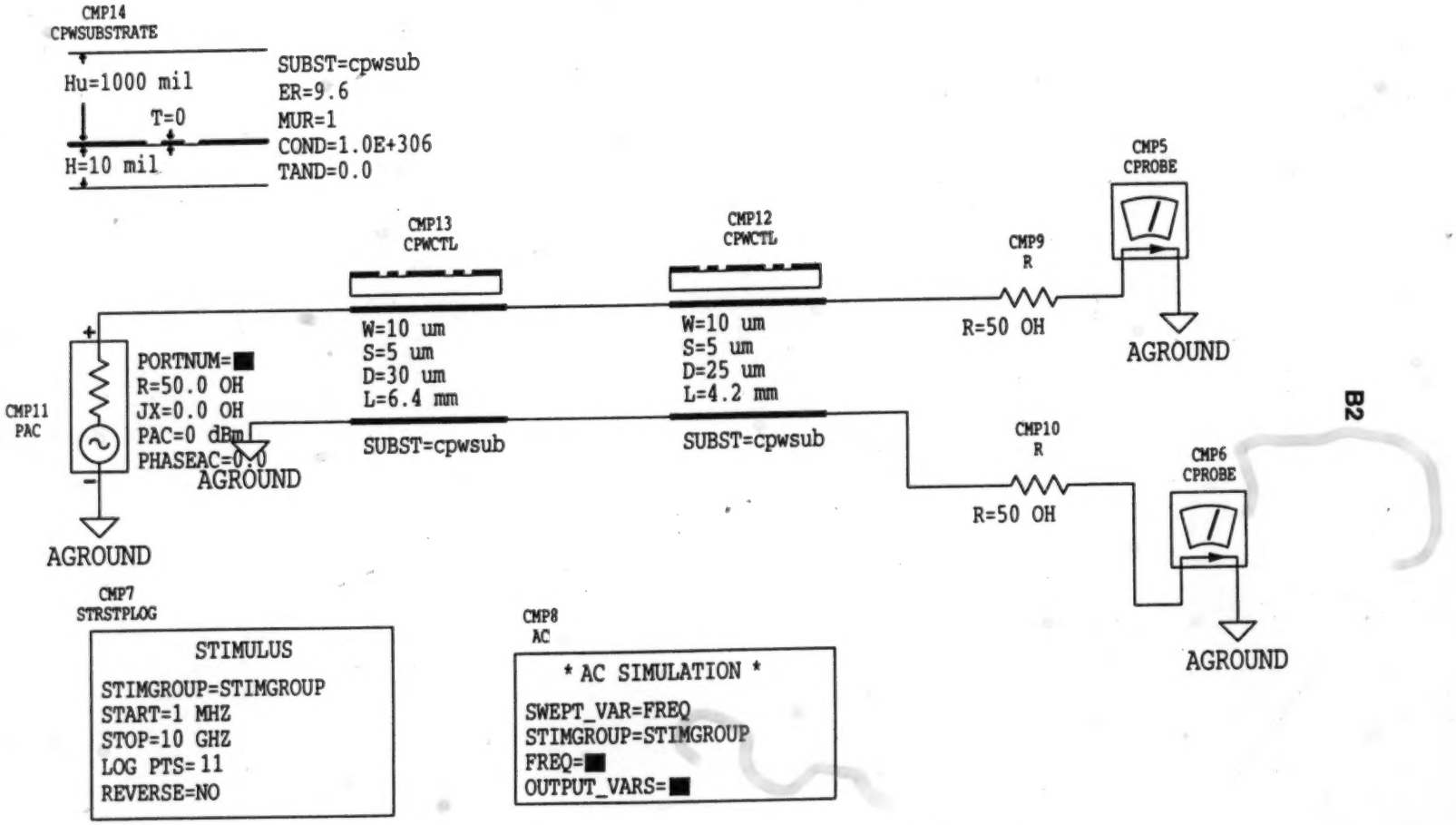
CMP14
CPWSUBSTRATE
Hu=1000 mil
T=0
H=10 mil
SUBST=cpwsub
ER=9.6
MUR=1
COND=1.0E+306
TAND=0.0
CMP13
CPWCTL
CMP12
CPWCTL
CMP9
R
CMP5
CPROBE
W=10 um
S=5 um
D=30 um
L=6.4 mm
W=10 um
S=5 um
D=25 um
L=4.2 mm
R=50 OH
AGROUND
CMP11
PAC
PORTNUM=
R=50.0 OH
JX=0.0 OH
PAC=0 dBm
PHASEAC=0.0
AGROUND
SUBST=cpwsub
SUBST=cpwsub
CMP10
R
CMP6
CPROBE
R=50 OH
AGROUND
AGROUND
CMP7
STRSTPLOG
STIMULUS
STIMGROUP=STIMGROUP
START=1 MHZ
STOP=10 GHZ
LOG PTS=11
REVERSE=NO
CMP8
AC
* AC SIMULATION *
SWEPT_VAR=FREQ
STIMGROUP=STIMGROUP
FREQ=
OUTPUT_VARS=

B3

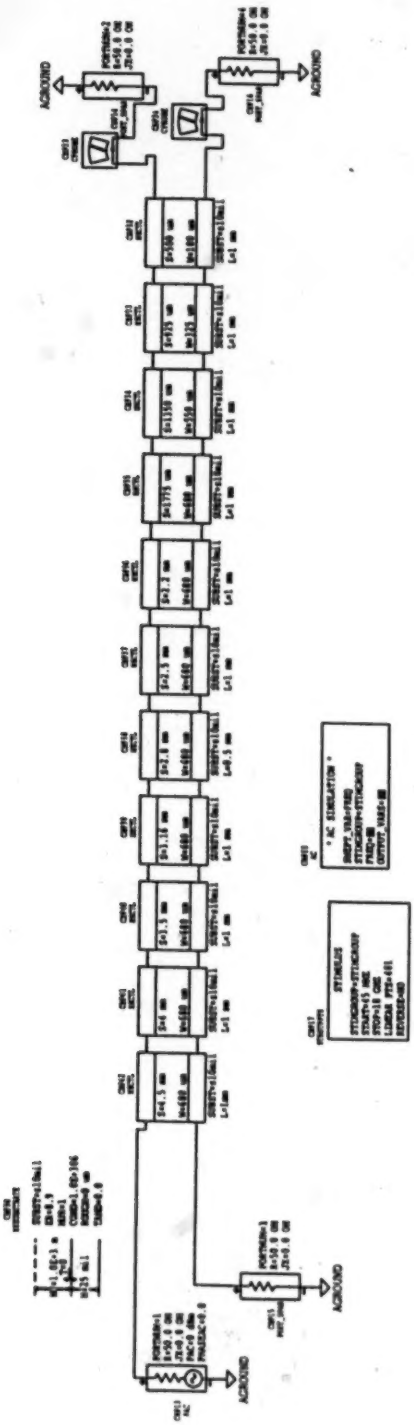

B4

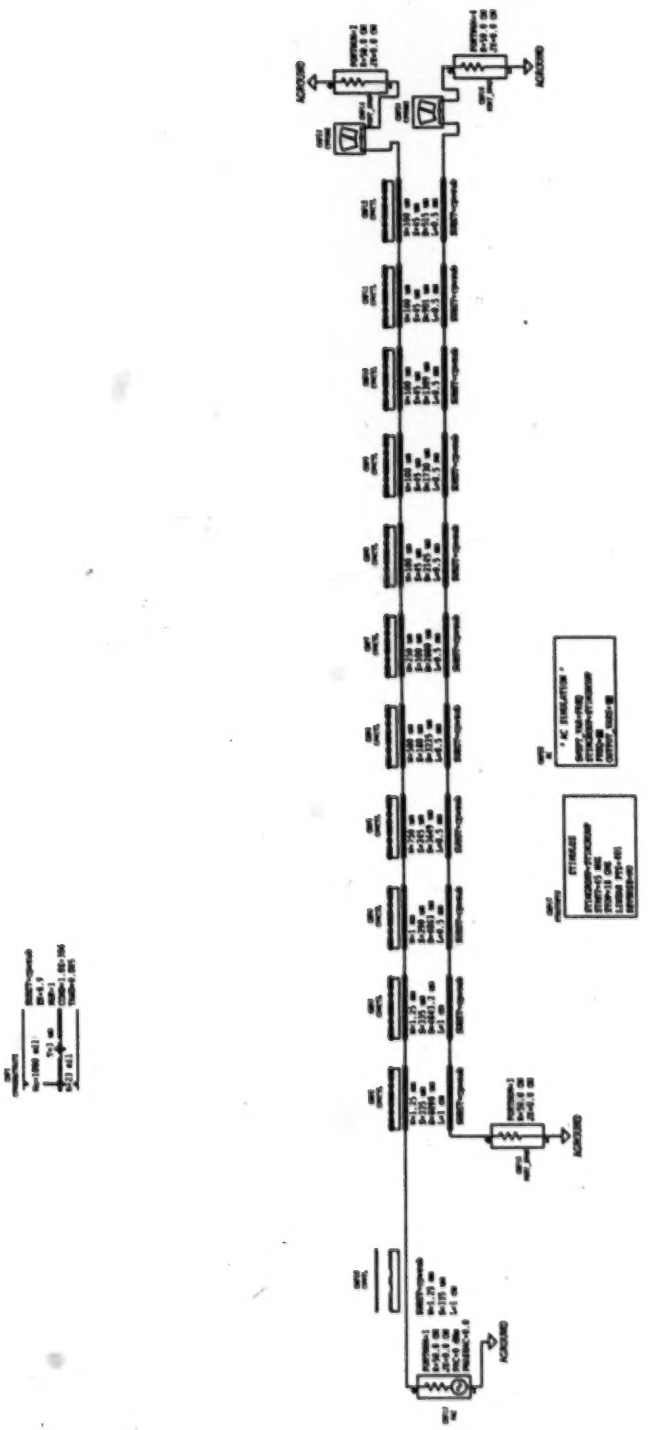

B5

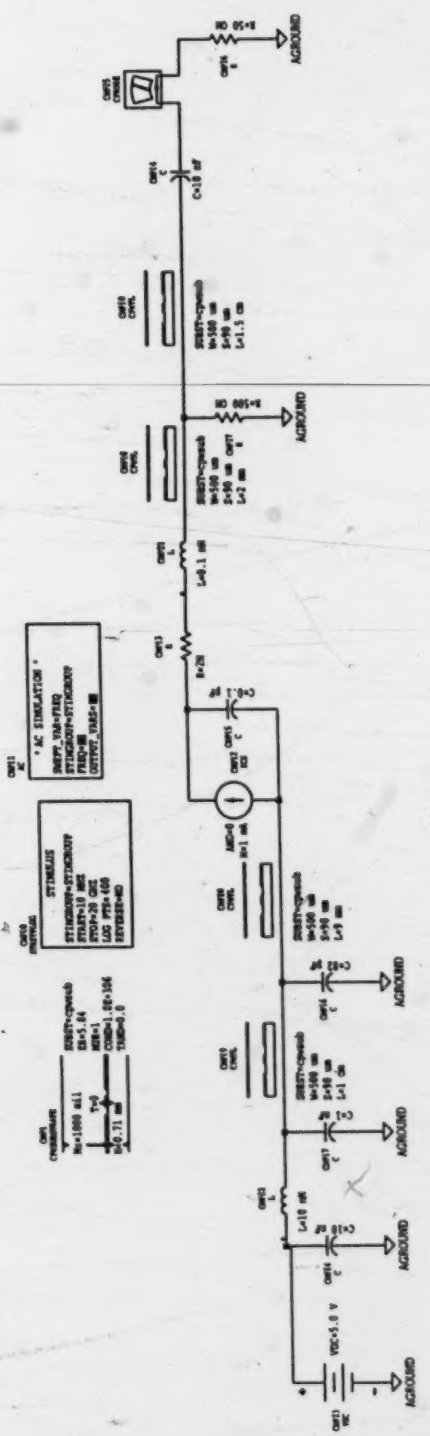

B6

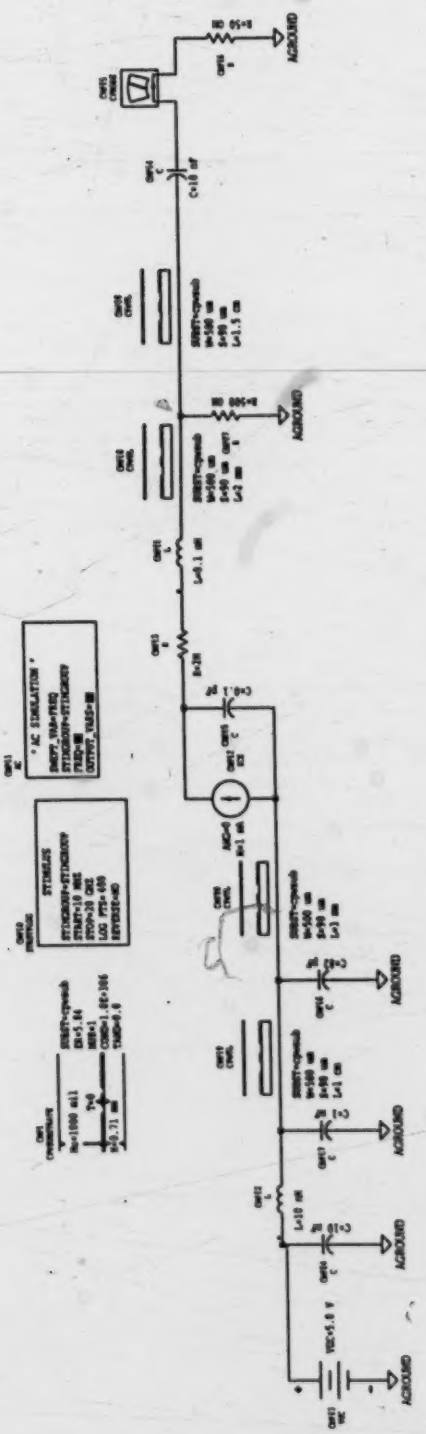

Appendix C
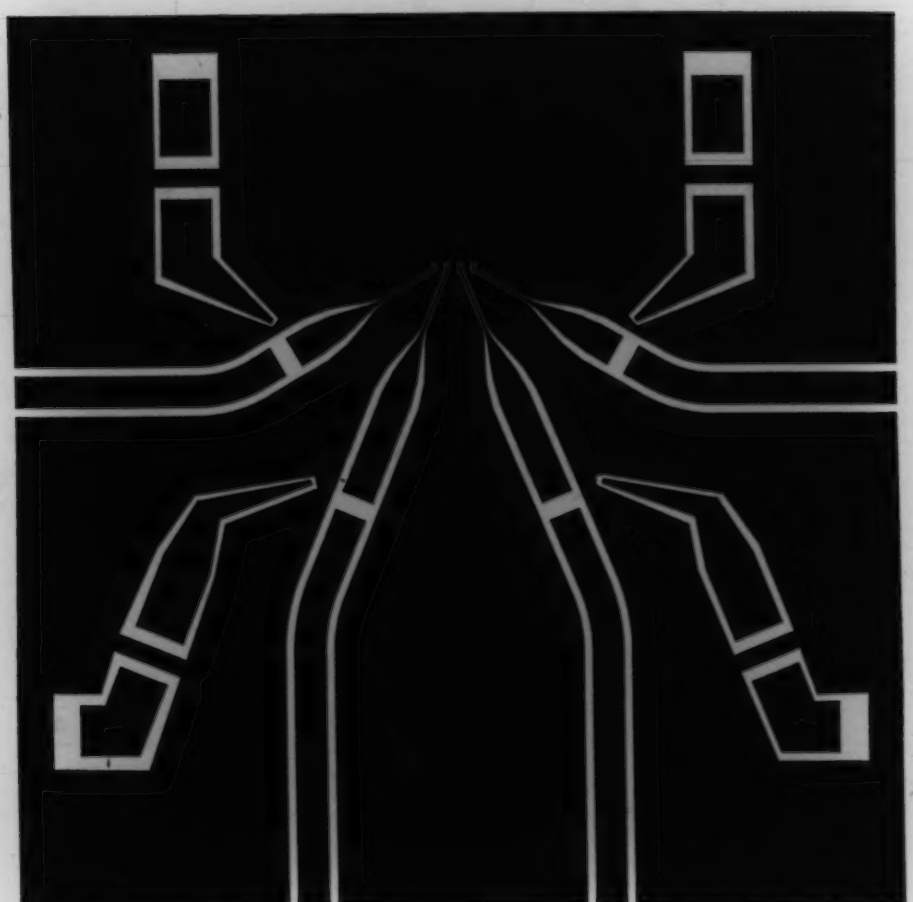
Metal layout of the 4-channel VCSEL dirver